TECHNISCHE UNIVERSITÄT MÜNCHEN
Max-Planck-Institut für Plasmaphysik

Tungsten Material Erosion under Deuterium and Carbon Co-bombardment

Heun Tae Lee

Vollständiger Abdruck der von der Fakultät für Maschinenwesen der Technischen Universität München zur Erlangung des akademischen Grades eines

Doktor-Ingenieurs

genehmigten Dissertation.

Vorsitzender:	Univ.-Prof. Dr.-Ing. H. Baier
Prüfer der Dissertation:	1. Hon.-Prof. Dr.-Ing., Dr.-Eng. (Univ. Nagoya/Japan) H. H. Bolt
	2. Univ.-Prof. Dr. mont. habil. E. Werner

Die Dissertation wurde am 23.06.2009 bei der Technischen Universität München eingereicht und durch die Fakultät für Maschinenwesen am 19.10.2009 angenommen.

Für meine Familie

Kurzfassung

Seit 2007 wird in Cadarache in Südfrankreich der Internationale Thermonukleare Experimentalreaktor ITER gebaut, mit dem erstmals ein selbständig brennendes Fusionsplasma mit magnetischem Plasmaeinschluss demonstriert werden soll. Als plasmaexponierte Materialien sind Beryllium (Be), Wolfram(W) und Kohlenstoff (C) je nach Einsatzbedingungen vorgesehen. Der Divertorbereich, der als Schnittstelle zwischen Plasma und Wand die Teilchenabfuhr aus dem Plasma kontrolliert, ist den höchsten Teilchenflüssen und thermischen Belastungen ausgesetzt. Für diesen Bereich werden deshalb C- und W-basierte Komponenten verwendet werden. Durch den Plasmakontakt kommt es zu Erosionsprozessen und in der Folge durch Plasmatransport und Redeponierung an anderen Stellen zur Ausbildung von C-W Mischmaterialien, deren Eigenschaften und Wechselwirkung mit dem Plasma sich stark von denen der reinen Stoffe unterscheiden. Aus diesem Grund ist es notwendig, die Bedingungen zu untersuchen, unter denen sich C-W Mischmaterialien bilden und die grundlegegenden Prozesse und deren Parameter-abhängigkeiten zu identifizieren. Zusätzlich ist es notwendig, die Erosionsprozesse von C-W Mischungen und deren Wasserstoffrückhaltevermögen zu charakterisieren, da diese eine große Bedeutung im Hinblick auf die Lebensdauer der Wand und die Bildung gebundener Tritiuminventare hat.

Um den geringen Wissensstand zu den Eigenschaften und Plasmawechselwirkungen von C-W Mischmaterialien zu erweitern, wurden im Rahmen der vorliegenden Dissertation die Bedingungen untersucht, unter denen sich bei gleichzeitigem Einfall von Deuterium (D) und C auf W-Oberflächen C-W Mischsysteme bilden. Damit verbunden waren Untersuchungen zu den dabei stattfindenden grundlegenden Prozessen, wie W-Erosion, C-Implantation und C-Reerosion sowie D-Implantation. Diese wurden in-situ mittels Ionenstrahlanalyse quantitativ charakterisiert. Durch Verwendung zweier unabhängiger Ionenquellen für D und C war es erstmals möglich, als wichtigsten Parameter den Anteil von C im einfallenden Ionenfluß frei zu variieren. Darüberhinaus wurde auch die D-Einfallsenergie im Bereich $0.5 - 3\,keV$ und die Temperatur der W-Oberfläche im Bereich $RT - 870\,K$ variiert. Die physikalischen Prozesse bei Ioneneinfall auf Festkörper können über einen weiten Bereich durch die Kinetik von binären Stoßprozessen (BCA) beschrieben werden. Hiezu wurde das Programm TRIDYN verwendet, daß gleichzeitig auch Veränderungen der Oberflächenzusammensetzung modelliert. Chemische Prozesse wurden in das Modell über einen phänomenologischen Ansatz eingeführt, der im Rahmen dieser Arbeit neu entwickelt wurde.

Aus dem Beschuss von W mit C-Ionen allein konnte abgeleitet werden, daß sich W-Zerstäubung und C-Implantation durch einen einzigen Parameter, nämlich die Gesamtmenge implantierten Kohlenstoffs n_c, beschreiben lassen. Mit zunehmender Temperatur ($RT \rightarrow 870\,K$) wurde eine entsprechende Zunahme der Kohlenstoffselbstzerstäubungs-ausbeute ($Y_c^c = 0.29 \rightarrow Y_c^c = 0.64$) nachgewiesen. Diese konnte im Rahmen des BCA-Modells auf eine mit der Temperatur abnehmende Oberflächenbindungsenergie ($7.4 \rightarrow 3.1\,eV$) zurückgeführt werden. Mit diesem zusätzlichen Parameter konnte das Modell auf höhere Temperaturen erweitert werden. Bei den höchsten erreichbaren Temperaturen wurden Diskrepanzen zwischen Modell und Experiment beobachtet, die auf zusätzlich einsetzende Prozesse außerhalb des Modells, wie C-Diffusion und C-Segregation und damit einhergehende Zunahme der Oberflächenrauhigkeit zurückzuführen sind.

Unter gleichzeitigem Beschuß von W mit C und D können abhangig von den Beschußparametern zwei stationare Zustände auftreten: entweder fortlaufende W-Erosion oder Bildung und fortlaufendes Aufwachsen einer geschlossenen C-Schicht. Daraus wurden folgende grundlegende Schlussfolgerungen gezogen: 1) Zusätzlich zur physikalischen Zerstäubung wird Kohlenstoff in der C-W Mischungszone durch chemische Zerstäubung erodiert. Dies geschieht durch Anlagerung von D an offene C Bindungen, die durch C und D Implantation erzeugt werden. Zu niedrigereren D Einfallsenergien wächst die chemische Zerstäubungsausbeute an, analog zu dem für reinen Kohlenstoff bekannten Verhalten. 2) Bei Erhöhung der Targettemperatur verschwindet der Beitrag chemischer C-Erosion. Die Dynamik von C-Implantation und W-Erosion wird durch TRIDYN vollständig beschrieben, wobei die Temperaturabhängigkeit durch die C-Selbstzerstäubung bedingt ist. Bei niedrigem Anteil von C im einfallenden Ionenmix, f_c, wird im Gleichgewicht kontinuierlich W erodiert. Bei $f_c = 0.10 \pm 0.01$ geht das System in den alternativen Gleichgewichtszustand mit kontinuierlichem Aufwachsen einer C Schicht über. Durch die mit der Temperatur zunehmende C-Sebstzerstäubung verschiebt sich die Grenzkonzentration zu entsprechend höheren Werten (z.B. $f_c = 0.13 \pm 0.02$ bei $770\,K$). 3) Die W-Zerstäubungsausbeute ist durch die lineare Überlagerung der partiellen Ausbeuten für D und C Ioneneinfall gewichtet mit dem jeweiligen Anteil im einfallenden Ionenstrahl und mit der W-Oberflächenkonzentration gegeben. 4) In der C-W Mischungszone findet man die größte Konzentration von gebundenem D. Mit steigender Targettemperaur verringert sich die D-Konzentration, ist jedoch auch bei der maximal erreichbaren Temperatur von $870\,K$ immer noch nachweisbar, woraus man schließen kann, daß D vor allem an Fehlstellen und an offenen C Bindungen eingefangen wird. Beim Aufwachsen einer reinen Kohlenstoffschicht findet man für das D/C Verhältnis die aus der Literatur bekannten Werte (z.B. 0.4 bei RT).

Der für die Fusionsforschung wesentliche Erkenntnisgewinn dieser Dissertation liegt in der erfolgreichen Validierung des BCA Modells für kombinierten Einfall von D+C auf W. Dies erlaubt den Einsatz des BCA-Codes TRIDYN in Kombination mit Plasmatransportcodes für eine plasmabelastete Wand mit Komponenten sowohl aus C als auch W, um die zu erwartenden Wandveränderungen durch Materialmigration und -mischung mit wesentlich größerer Genauigkeit vorhersagen zu können.

Abstract

To demonstrate the feasibility of fusion power, the International Thermonuclear Experimental Reactor (ITER) is presently being built in Cadarache, France. Carbon (C) and tungsten (W) materials are planned to be used in the divertor region of ITER as target plates and for the surrounding baffle and dome, respectively. Consequently, C-W mixed materials will form by erosion, transport, and redeposition processes, whose properties and interaction with the edge plasma will be significantly different from the pure materials. Therefore, there is a need to understand the formation conditions of different C-W mixed materials, which requires elucidation of the main processes and identifying the effects of parameter variation on the C-W mixed material behavior. Also required is the characterization of the C-W mixed material erosion and hydrogen retention behavior with their corresponding impact on plasma facing component lifetime and tritium inventory issues.

To extend the scarce knowledge on physics and plasma surface interactions of C-W mixed materials, this study examined the dynamics and formation conditions of C-W mixed materials by simultaneous C-D ion beam experiments. In the experiments, the amount of C implanted, the amount of W sputtered, and the amount of D retained as a function of incident fluence were measured in-situ by ion beam analysis. The parameters considered were: (1) the C fraction in the incident flux, f_c, (2) the specimen temperature ($RT - 870\,K$), and (3) the incident energy of the D ions ($0.53 - 3\,keV$). A phenomenological model based on the binary collision approximation model (TRIDYN) calculations has been developed to describe the chemical sputtering component observed during simultaneous irradiation at RT.

Tungsten irradiation by C-only at RT showed that the W sputtering behavior can be fully parametrized by the implanted carbon amount, n_c, effectively reducing the problem of C implantation and W sputtering processes to one parameter. With increasing temperature ($RT \rightarrow 870\,K$), a corresponding increase in the C self-sputtering yield was measured ($Y_c^c = 0.29 \rightarrow Y_c^c = 0.64$). The increase in C self-sputtering yields can be described in TRIDYN by reducing the C-C surface binding energies ($SBEs$) ($7.4 \rightarrow 3.1\,eV$). These $SBEs$ were used to successfully model the experimental results of W irradiation by C ions at elevated temperatures. Discrepancies between simulations and experiments are attributed to possible changes to the C surface concentration by diffusion or segregation effects, and the observed increase in surface roughness by island like C layer growth.

Under simultaneous C-D irradiation, the system develops into two distinct steady state regimes of continuous W erosion or continuous C layer growth depending on the main parameters varied. The main conclusions are: (1) A chemical sputtering process was observed involving the trapped D passivating broken C bonds resulting from C or D ion implantation. Lowering the incident D ion energy resulted in an increase of the chemical sputtering yield from a maximum value of $Y_{chem} \approx 0.04$ at $E_D = 3\,keV$ to $Y_{chem} \approx 0.08$ for lower D energies. (2) With increasing temperature, the C implantation and W sputtering behavior is described well by the TRIDYN model with the dominant

effect being the increased C self-sputtering yield. No chemical sputtering processes were observed. The transition point separating the two regimes was determined to be $f_c = 0.10 \pm 0.01$ at RT and increases with temperature (e.g. $f_c = 0.13 \pm 0.02$ at $770\,K$). (3) The W sputtering yield was determined to be a linear superposition of the partial sputter yields weighted to their fraction in the incident flux, which is proportional to the W surface concentration. (4) The mixed material region contained the highest relative concentration of D trapped. This amount decreased with increasing temperature, but D trapping was still observed at $870\,K$, indicating high trap energies normally associated with D trapping at C or vacancy sites. The D/C ratio in the co-deposited layer was 0.4 at RT and 0.02-0.05 at elevated temperatures.

The main achievement in the framework of fusion research is that the TRIDYN model has been bench-marked for a C-W mixed material system at $T \leq 870\,K$. The developed understanding can be applied to provide experimentally bench-marked input parameters used in present day impurity transport codes to better model the erosion and redeposition processes in tokamak devices and extrapolation to ITER and future fusion reactor (DEMO) conditions.

Contents

Kurzfassung i

Abstract iii

List of Figures xii

List of Tables xiii

1 Introduction 1
- 1.1 Fusion energy and plasma facing materials . . . 1
- 1.2 Carbon and Tungsten as plasma facing materials . . . 2
- 1.3 Safety aspects of Tritium operation . . . 4
- 1.4 Carbon-Tungsten mixed materials . . . 6
- 1.5 Thesis purpose and direction . . . 8

2 Background 11
- 2.1 Physical sputtering . . . 11
  - 2.1.1 TRIDYN . . . 13
  - 2.1.2 Carbon and Tungsten sputtering by Carbon . . . 15
  - 2.1.3 Tungsten and Carbon sputtering by Deuterium . . . 17
- 2.2 Chemical erosion and sputtering of Carbon . . . 17
- 2.3 Simultaneous irradiation of Tungsten by Hydrogen and Carbon . . . 20
  - 2.3.1 Tungsten sputtering and Carbon surface behavior . . . 20
  - 2.3.2 Sputtering of C-W mixed materials by Deuterium . . . 21
  - 2.3.3 Hydrogen retention in Carbon and Tungsten materials . . . 21

3 Experimental facilities 25
- 3.1 Dual beam ion accelerator . . . 25
- 3.2 Dual beam target chamber . . . 27
- 3.3 Experimental technique . . . 28
  - 3.3.1 Specimen preparation by magnetron sputtering . . . 29
  - 3.3.2 Specimen characterization . . . 30
  - 3.3.3 Rutherford backscattering spectrometry . . . 36
  - 3.3.4 Nuclear reaction analysis . . . 37
  - 3.3.5 Beam viewing system and fluence measurements . . . 39
  - 3.3.6 Calibration of BVS measurements . . . 40
  - 3.3.7 Temperature measurements . . . 43

4 Carbon-only irradiation 45
- 4.1 Specimen characterization . . . 45
  - 4.1.1 Surface roughness . . . 46
  - 4.1.2 XPS depth profiling . . . 49
- 4.2 Carbon-only irradiation of Tungsten . . . 50
  - 4.2.1 Parametric representation . . . 52
  - 4.2.2 Carbon self-sputtering and comparison to TRIDYN . . . 55

4.2.3 Summary 60

5 Simultaneous irradiation by Deuterium and Carbon ions 61
5.1 Carbon deposition regime 62
5.1.1 Deuterium retention 63
5.1.2 Elevated temperature 69
5.1.3 Summary 73
5.2 Tungsten erosion regime 73
5.2.1 Tungsten sputtering 74
5.2.2 Chemical sputtering of C-W mixed material 78
5.2.3 Summary 87
5.3 Discussion and conclusion 87

6 Modeling 91
6.1 Kinematic component 91
6.2 Chemical sputtering 96
6.3 Depth profiles 98
6.4 Summary 98

7 Implications for next step fusion reactor 101
7.1 Tungsten erosion and impact on component lifetime 101
7.2 Issue of fuel inventory and co-deposition 105
7.3 Limitation of TRIDYN use in modeling plasma wall interactions 106

8 Conclusions 109
8.1 Carbon-only irradiation 109
8.2 Simultaneous irradiation by Deuterium and Carbon ions 111

9 List of publications and posters 115
9.1 Publications 115
9.2 Poster presentations 115

References 117

Acknowledgments 135

List of Figures

1.1 (a) Schematic of the tokamak configuration (b) Schematic of ITER cross section illustrating the divertor configuration as well as showing the locations and choice of plasma facing materials Be, C, and W. 2

1.2 Schematic overview of some plasma wall interactions relevant to C-W mixed material or C layer formation: (1) reflection, (2) implantation, (3) D trapping/detrapping or co-deposition (solid circle), (4) carbide formation (open circle), (5) diffusion, (6) sputtering, and (7) redeposition. . 6

1.3 This thesis combines experimental and simulation work to achieve three main objectives. Investigations of: (a) the dynamics of C-W mixed material formation and its dependence on parameter variation (C fraction in the incident flux, temperature, and incident D energy), (b) erosion behavior of C-W mixed materials and implication to component lifetime issue, and (c) D retention behavior with implication to tritium safety issue. 9

2.1 Temperature dependent erosion processes for carbon (from Ref. [75]). 12

2.2 Definition of impact parameter b, scattering angle θ, and the azimuthal scattering angle, φ in the laboratory framework. 14

2.3 Chemical erosion cycle (from Ref. [110]). 18

3.1 Schematic of Dual Beam Experiment (DBE). 26

3.2 Schematic of the target chamber flange of the Dual Beam Experiment. 26

3.3 Schematic of target holder assembly showing: (1) beam viewing system (BVS), (2) calibration targets, (3) target holder, and (4) target heaters. 28

3.4 Schematic of the (a) magnetron sputter device, and (b) the cross section of a planar magnetron, where the electrons are trapped in cyclic motion near the target surface, leading to a higher plasma density and corresponding increase in cathode sputtering. 30

3.5 Atomic force microscope (AFM) images of deposited W-film specimens using an (a) old tip and (b) virgin tip. The numbers indicate the root mean square (RMS) roughness value, R_q in nm. 31

3.6 Comparison of the as-deposited W film surface from (a,c) SEM and (b,d) AFM measurements for two different scanned areas. 32

3.7 X-ray diffractograms obtained using the gracing incidence geometry of a virgin as-deposited W specimen (black) and a specimen annealed at $870\,K$ for $4\,h$ (red). Also shown for comparison is the spectrum from ITER grade bulk W (orange). Each spectrum is normalized to its respective maximum intensity observed at the W(110) peak. The positions of the W peaks are taken from JCPDS database PDF 04-0806 [152] with the relative intensities corresponding to body-centered-cubic (bcc) α-W phase indicated by the blue points; the unlabeled peaks in the W-film spectra correspond to the Ni substrate. 33

3.8 Comparison of AFM images of as-deposited W specimens with annealed specimens at $770\,K$ and $870\,K$ for $4\,h$. 35

3.9 Comparison of sample AFM surface elevation of as-deposited W specimen with specimen annealed at $770\,K$ for $4\,h$ in the region where the different orientation of the platelets meet in Fig. 3.8. 35

3.10 Typical RBS spectrum collected between each irradiation step showing the decrease in the width of the tungsten peak as a result of sputtering. 36

3.11 RBS spectrum showing: (a) the effect of W-Ni interface mixing resulting in decrease of W peak at the trailing edge, and (b) the effect of surface roughness on the trailing edge of the W peak. 37

3.12 NRA spectrum of a hard a-C:D calibration target showing the four proton peaks from the D(^{3}He, p)^{4}He and ^{12}C(^{3}He, p)^{14}N nuclear reactions. The C-related peaks of p_0, p_1, and p_2 correspond to protons from reactions with ^{14}N in ground state, $2.313\,MeV$ excited state, and $3.948\,MeV$ excited state [159], respectively. 38

3.13 Normalized current measurements of: (1) steady C and D beams resulting in near constant total current during one irradiation step, and (2) unsteady C beam resulting in fluctuations in the total current measurement. Curve (1) has been offset from zero to better distinguish the two curves. 39

3.14 Images of the D and C beams, as well as the analysis ^{3}He$^+$ beam measured using the BVS. The first row corresponds to the raw images captured by the CCD camera, while the second row shows a color mapping of the intensity variation mapped in the computer language IDL environment. 41

3.15 Schematic diagram of: (a) the major components of the Beam viewing system, and (b) exploded view of the housing showing the stacking sequence of the microchannel plate (MCP) and phosphor screen. Also shown are the (c) technical drawings showing the major dimensions of the BVS and the mounting assembly. 41

3.16 Calibration curve showing the linear dependency of the fluctuation of the local C current determined by the BVS against the total C current measured by the picoammeter. 42

3.17 The pyrometer temperature readings calibrated against thermocouple measurements. 43

4.1 AFM measurements of C-only irradiation specimens presented in Fig. 4.4 for both on- and off- beam spots at RT, $670\,K$, $770\,K$, and $870\,K$. The numbers indicate the RMS surface roughness values, R_q in nm. The column outlined in black corresponds to the location on each specimen where the fluence dependent C and W areal density changes was measured by ion beam analysis and presented in Fig. 4.4. Therefore, these images correspond to the surface topographies and R_q values following the final irradiation step. 47

4.2 SEM images showing the surface morphology at different magnification: (a,b) before full C coverage, and (c,d) after full C coverage. 48

4.3 Comparison of XPS and TRIDYN depth profiles for C-only irradiation at RT. The black line indicates the sputter depth measured by profilometry following XPS. 49

4.4 C-only irradiation of W at $RT - 870\,K$. Plotted is the: (a) implanted C areal density, and (b) sputtered W areal density as function of incident C fluence. 50
4.5 Comparison of: (a) Experimental W sputter yield as a function of implanted C areal density, n_c at various temperatures with TRIDYN calculation using the $SBEs$ corresponding to RT, and (b) the effect of incident angle, α_T, in the W sputter yield calculated by TRIDYN at low implanted C areal density corresponding to low C surface coverage. . . 51
4.6 (a) Surface C and W concentrations calculated by TRIDYN plotted against the total implanted C areal density for varying averaged depths. (b) Fig. 4.5(a) re-plotted as a function of the C surface concentration. 53
4.7 Parametric representation of C-only irradiation of W at various temperatures. 54
4.8 The increase of implanted C amount with increasing incident C fluence for temperature range $RT - 870\,K$ for C films irradiated by $6\,keV$ C ions. The implanted C amount is the difference between the initial C areal density measured by NRA and the subsequent increase measured with each irradiation step. The numbers indicate the slope of the linear fit. 54
4.9 Comparison of C self-sputtering yield against Schmid et al. [60]. 56
4.10 Parameter scan in TRIDYN to determine the dependence of Y_c^c on SBE_c. 57
4.11 Comparison of TRIDYN calculations using SBV_{ij} from Table 4.2 with experimental data presented in Fig. 4.4. The numbers indicate the angle of incidence, α_T, used in TRIDYN simulations. 58
4.12 Calculated TRIDYN values of the C reflection and sputter yields as a function of implanted C for temperatures RT, $670\,K$, $770\,K$, and $870\,K$. 59
5.1 Implantation sputter curves for simultaneous irradiation at RT for various f_c compared against TRIDYN calculation using an incident angle of $\alpha_T = 15°$. Sample error bars for the C deposition and W sputtering regimes are shown. A discussion of the experimental results for $f_c \geq 0.11$ is found in section 5.1. The discrepancy between experimental results and TRIDYN for $f_c \leq 0.11$ will be discussed in section 5.2. 62
5.2 Comparison of: (a,c) C implantation, and (b,d) W sputtering behavior as a function of incident C fluence for varying values of f_c resulting in the C deposition regime. Also shown are results of TRIDYN simulations. 63
5.3 AFM images of the C surface layer grown during simultaneous irradiation at RT for $f_c = 0.20$ for scan area of: (a) $4\,\mu m \times 4\,\mu m$, and (b) $2\,\mu m \times 2\,\mu m$. The numbers indicate the roughness values, R_q in nm. . 64
5.4 Raman spectroscopy results comparing the C layer growth by C-only irradiation (red circle) against simultaneous irradiation (black square). Also shown are the D and G peak locations at $1360\,cm^{-1}$ and $1550\,cm^{-1}$, respectively (from Ref. [174]). 64
5.5 Changes in the cross section of $2.5\,MeV$ D(^{3}He, p)^{4}He reaction as a function of depth for C, W, and Ni using the energy loss calculated by the TRIM.SP code [84] and using the cross section data of Ref. [176]. 65

5.6 NRA α-spectrum at a scattering angle of 105° using the cross section of $0.69\,MeV$ D(^{3}He, ^{4}He)p reaction for $f_{\rm c} = 0.20$ for an annealed and unannealed specimen. Shown are: (a) the raw data fitted with SIMNRA [158], and (b,c) converted to a depth scale assuming the densities of pure C and W. The numbers indicate the ratios of D/C, D/(C+W), and D/W at the indicated depth, while the C-W mixed material region is approximately highlighted by the hatched magenta box. 66

5.7 Total deuterium retention as function of incident D fluence for varying $f_{\rm c}$'s in the C deposition regime. Also plotted for the $f_{\rm c} = 0.20$ case is the integrated D amount obtained from the α-spectrum of both annealed and unannealed specimens. For comparison, D retention results from ITER grade polycrystalline W (PCW) specimens (section 5.2) are plotted (orange squares) together with literature values for single crystal tungsten: $6\,keV$ - Alimov et al. [145] (blue line) and $5\,keV$ - Nagata et al. [180] (green line); and PCW: $1\,keV$ - Haasz et al. [181] (dashed black line) and $0.2\,keV$ - Ogorodnikova et al. [139] (dashed purple line). . . 67

5.8 Comparison of experimental results for $f_{\rm c} = 0.20$ at increasing temperatures against: (a) TRIDYN calculations using $SBEs$ derived in section 4.2.2, and (b) phenomenological model discussed in section 6. The dashed TRIDYN calculations correspond to $\alpha_T = 20°$. 70

5.9 NRA α-spectrum measured at a scattering angle of 105° using the cross section of $0.69\,MeV$ D(^{3}He, ^{4}He)p reaction for $f_{\rm c} = 0.20$ for: (a) $670\,K$, and $770\,K$. Also, shown are the relative concentrations of D, C, and W as a function of depth for: (b) $770\,K$, and (c) $870\,K$ data. The numbers indicate the ratios of D/(C+W) and D/W at the indicated depth, while the C-W mixed material region is approximately highlighted by the hatched magenta box. 71

5.10 C layer thickness estimated by the maximum D peak depth in the α-spectrum for various $f_{\rm c}$'s indicated by the colored numbers at $670\,K$ and $770\,K$. Eqn. 5.1 is plotted for varying δ's. 72

5.11 Comparison of experimental results for varying f_c in the W sputtering regime with TRIDYN calculations. The steady state C areal density is constant at $n^c_{ss} \approx 0.065 \times 10^{22}\,m^{-2}$. 74

5.12 The amount of W sputtered as a function of total incident fluence for $f_c \leq 0.07$. The numbers indicate the slope of the linear fit, which is the total W sputter yield, Y_w. 76

5.13 Ex-situ XPS analysis following irradiation of the specimens with two different $f_{\rm c}$'s to determine: (a) the surface C and W elemental compositions, and (b,c) corresponding chemical binding information . The relative peak areas in (a) do not directly reflect the relative amounts due to the difference in photoionisation cross section. 77

5.14 Comparison of C implantation and W sputtering behavior for $f_{\rm c} = 0.07$ at different temperatures compared against TRIDYN calculations using the $SBEs$ derived in section 4.2.2. Also included is the range of the C areal density observed for ITER grade PCW specimens irradiated at RT outlined in orange. 79

5.15 Comparison of the W sputtering as a function of incident total fluence. The number indicates the slope and yields the total W sputter yield. . 80

5.16 Total D retention as function of incident D fluence for $f_c = 0.07$ for W-film specimens at various specimen temperatures. Also plotted are D retention results from ITER grade polycrystalline tungsten specimen (orange squares) irradiated at RT. The published literature values for tungsten single crystal: $6\,keV$ at $650\,K$ - Alimov et al. [145] (dashed blue line) and PCW: $1\,keV$ at RT - Haasz et al. [181] (dashed black line) with unpublished values at $3.33\,keV$ at $500\,K$ - O. Ogorodnikova (blue cross) are also plotted for comparison. 80

5.17 Comparison of C implantation and W sputtering behavior for: (a,b) $E_D = 3\,keV$, and (c,d) $E_D = 1\,keV$ at $f_c = 0.11$ plotted with the model and the fitted Y_{chem} component. 82

5.18 Comparison of the normalized D ranges calculated with TRIM [188] for $E_D = 3\,keV$ and $E_D = 1\,keV$ in pure W. The C depth profile is taken from TRIDYN simulations at $n_c = 0.06 \times 10^{22}\,m^{-2}$ and corresponds to an absolute scale. The dotted black lines indicate the mean ion ranges. 84

5.19 Comparison of: (a) C implantation, and (b) W sputtering behavior as a function of incident C fluence for varying incident D energies: (c,d) $E_D = 3\,keV$, (e,f) $E_D = 1\,keV$, and (g,h) $E_D = 0.53\,keV$ at $f_c = 0.23$ plotted with model predictions including and excluding the Y_{chem} component respectively. Also shown is the fitted Y_{chem} component in red. 85

5.20 Comparison of C implantation and W sputtering behavior for $f_c = 0.23$ at $670\,K$ for varying incident D energies. Shown also are the results calculated by the model without any Y_{chem} component. 86

5.21 Total D retention as function of incident D fluence for $f_c = 0.23$ at RT and $670\,K$ for various incident D energies. 86

5.22 Comparison of C implantation and W sputtering behavior for $f_c = 0.14$ at different temperatures with $3\,keV$ D. 88

5.23 The effect of changing f_c on: (a) C implantation, and (b) W erosion. Similarly, the effect of surface roughening on the dynamics of: (c) C implantation, and (d) W erosion, is shown. 89

6.1 Analytical fits for $Y_c^c(n_c)$ and $R_c(n_c)$ for varying temperature using the parameters listed in Table 6.1. 93

6.2 Comparison of TRIDYN calculations of n_c, against the model using the analytical forms of $Y_c^c(n_c)$ and $R_c(n_c)$ for varying temperature using the parameters listed in Table 6.1. 95

6.3 Comparison of TRIDYN calculations of n_w, against the model using Eqn. 6.4, where $Y_w(S_w(n_c))$ for varying temperatures. 95

6.4 Comparison of TRIDYN calculated depth profiles for increasing implanted carbon areal density, n_c. The numbers indicate the surface concentration of carbon. 97

6.5 Comparison of XPS sputter depth profiles at RT and $870\,K$ for simultaneous irradiation with $f_c = 0.28$. 98

7.1 Schematic of ITER divertor cassette showing the locations of the W plasma facing components on: (a) the inner vertical target and baffle, (b) the outer vertical target and baffle, and (c) the dome. The carbon plasma facing components at: (d) the vertical strike plates. 103

List of Tables

2.1 Calculated sputter yields using the revised Bohdansky formula at RT and $\alpha = 15°$. Also included are the experimentally measured sputter yields using the dual beam experiment in this study for $E_D = 3\,keV$ (in brackets). 17

3.1 Sample operating settings for Q1 source. 25

3.2 Sample operating settings for Q2 source. 27

3.3 The relative peak intensities observed for detector angle 2θ, for as-deposited specimen compared to annealed specimens at $770\,K$ and $870\,K$. Reference data from [152] is also listed. 33

4.1 Experimentally measured carbon self-sputtering yields. 55

4.2 Experimentally measured carbon self-sputtering yields and the SBV_{ij} used in all TRIDYN calculations to simulate the increased C self-sputtering with temperature. 57

5.1 AFM measurements of irradiated specimens for $f_c \leq 0.11$ presented in Fig. 5.11 for both on- and off- the irradiated areas. The numbers indicate the root mean square surface roughness values, R_q in nm. . . 74

5.2 Summary of the experimentally derived W sputter yield, Y_w, and the resulting proportionality factor, K_{f_c} along with the W surface concentration, S_w, measured by ex-situ XPS analysis following irradiation. S_w was determined by first normalizing the tungsten XPS peak in Fig.5.13(a) by its known sensitivity factor, then by taking the quotient of the normalized area against the total sum of the W, C, and O peaks. 76

6.1 Parameters for the fitting function described in Eqn. 6.2 for varying temperatures and angles of incidence. 93

6.2 Parameters for the function $Y_c^D(n_c)$ based on Eqn. 6.2, fitted against the partial D sputter yields from TRIDYN calculations for varying temperatures and angles of incidence. 94

6.3 Parameters for the function $Y_c^D(n_c)$ based on Eqn. 6.2, fitted against the partial D sputter yields from TRIDYN calculations for varying D energies at RT and $670\,K$. 96

7.1 Estimated gross erosion rates for the tungsten plasma facing components (plasma exposed side) at various divertor locations. 104

1 Introduction

1.1 Fusion energy and plasma facing materials

Fusion is the nuclear reaction between two light elements resulting in energy release as seen in our sun and other stars. Along with other alternative energy sources like solar, wind, or geothermal energy, fusion power is a promising long-term candidate to supply the long term energy needs of mankind [1]. On earth, the goal of harnessing fusion power has focused on the most readily achievable nuclear fusion reaction with deuterium-tritium as the fuel species:

$$\mathrm{D} + \mathrm{T} \rightarrow {}^{4}\mathrm{He}\ (3.5\,MeV) + \mathrm{n}\ (14.1\,MeV)$$

This reaction does not occur at ambient temperature because of the strong coulomb repulsion between the two positively charged nuclei. Only at very high temperatures a sufficiently high fraction of atoms in the high energy tail of the Maxwellian energy distribution are able to overcome this barrier by the tunnel effect. For such temperatures, the fuel is in the state of a fully ionized plasma, which must be confined at sufficient density and thermal insulation to release more energy than was required to heat the fuel. The quantitative formulation of this requirement is commonly known as Lawson's criterion [2]. At present, the most successful method for meeting the Lawson criterion has been the implementation of magnetic plasma confinement in the tokamak configuration (Fig. 1.1(a)). In 1997, the Joint European Torus (JET) achieved $16\,MW$ of peak fusion power with 65% ratio of fusion power to total input power (Q value) [3]. As $\approx$ 80% of the fusion power escapes the plasma with the neutrons, a self sustained fusion plasma requires a Q value of at least 5. An economically and technically viable fusion reactor requires much higher Q values in steady state operation, and as a first step in realizing this goal, the International Thermonuclear Experimental Reactor (ITER) under construction in France, aims to reach Q values of 5-10 with quasi steady state operation, (i.e. plasma discharges with a duration of $400\,sec$) [4].

One of the outstanding issues facing the development of fusion power and construction of ITER is the interaction of the edge plasma with the surrounding vessel wall. Such plasma wall interactions (PWIs) have an important role in determining the performance, as well as setting limits on the operational and safety aspects of a commercially viable fusion reactor. Consequently, the proper selection of materials to cover the vessel wall is a critical engineering decision that requires a clear understanding of how such plasma facing materials (PFMs) will behave under simultaneous: (i) heat loading, (ii) irradiation by energetic and thermal fuel species, and (iii) irradiation by helium and neutrons. Ideally, a plasma facing material will have high erosion resilience, high thermal conductivity, high thermal stress resistance, low tritium retention, and low embrittlement and nuclear activation. The tokamak vessel is composed of main chamber walls and the divertor structure used for fuel and impurity exhaust (See Fig. 1.1(b)). The two regions are subject to vastly different plasma exposure conditions

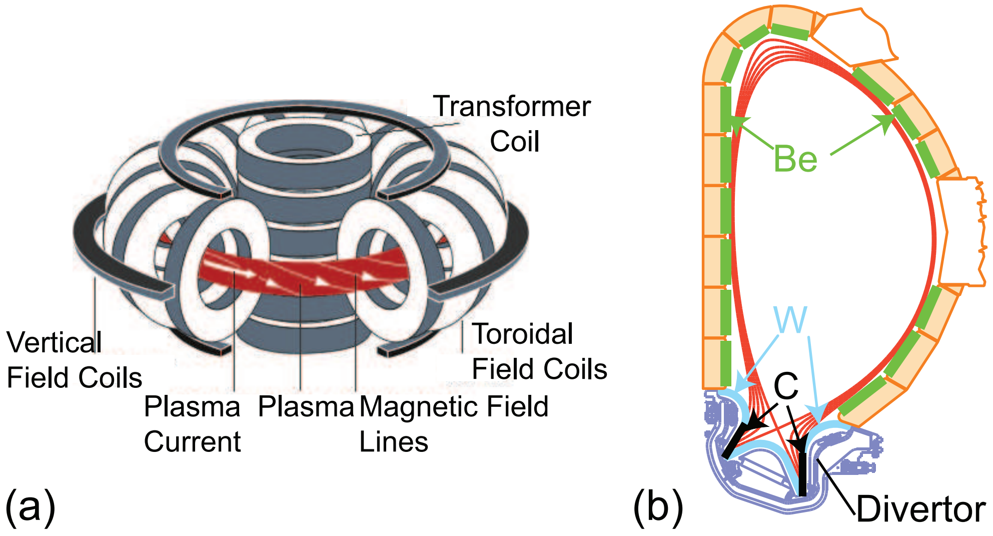

Figure 1.1: (a) Schematic of the tokamak configuration (b) Schematic of ITER cross section illustrating the divertor configuration as well as showing the locations and choice of plasma facing materials Be, C, and W.

[5] and no one material has been found yet to satisfy all criteria in all regions. This has led to the decision to select different materials for different regions based on the most critical criteria for a given part of the vessel. Although still under review [6], the ITER project plans to use beryllium (Be) for the main wall, while carbon fiber reinforced carbon (CFC) and tungsten (W) will be used in the divertor as target plates and for the surrounding baffle and dome regions, respectively. In this work, carbon and tungsten materials will be the main focus, because these materials are the most critical components due to the very intense particle flux ($> 10^{24}\,m^{-2}s^{-1}$) and power loads ($\leq 20\,MW/m^2$) experienced in the divertor.

1.2 Carbon and Tungsten as plasma facing materials

In contrast to present-day tokamaks, ITER will be operated with higher number of plasma discharges with longer pulse durations. The consequences of such operational conditions are: (i) the need for active cooling of the plasma facing materials to limit overheating and thermal stress, (ii) the increase in material erosion leading to component lifetime issues, and (iii) the increase in tritium retention leading to safety issues. The following discussion presents the material properties which have led to the decision to select carbon and tungsten as plasma facing materials in the divertor region and corresponding impact on component lifetime and tritium safety issues. Following ITER, the development of an electricity producing fusion reactor DEMO [7], in which tungsten is a leading candidate as plasma facing material, will require additional and partly different selection criteria for PFMs compared to ITER [8] and is not discussed here.

ITER will need to explore and extend the accessible parameter space of plasma operation, and therefore disruptions and off-normal recoverable plasma displacements cannot be avoided altogether [5]. The advantage of carbon and its selection as a plasma facing material for the divertor strike zones is mainly due to its resilience against such thermal shocks and tolerance of transient heat loads [9]. High heat flux testing of a prototype vertical target using a carbon fiber reinforced carbon (CFC) mono-block design has demonstrated its capability to sustain $20\,MW/m^2$ for 2000 cycles in line with ITER requirements [10]. However, the disadvantage of carbon is that it is eroded efficiently by both physical and chemical sputtering processes which could lead to component lifetime issues in ITER. Physical sputtering by self-sputtering (i.e. C sputtering C) and chemical sputtering by hydrogen (i.e. formation of volatile molecules) are temperature dependent processes and will be covered in detail in section 2. Chemical sputtering can be reduced by doping carbon materials by B, Si, or transition metals [11] but at the expense of mechanical property degradation like thermal conductivity [12]. A further disadvantage is that the eroded C is co-deposited with hydrogen, forming continuously growing layers at less exposed or remote surfaces that can lead to unacceptable tritium inventory ($> 700\,g$ [13]) in ITER [14]. Delamination and disintegration of such C layers may lead to formation of significant amounts of dust [15] with no efficient method of recovery. Therefore, the use of carbon-based materials is limited by its significant impact on tritium safety issue and likely prevent the use of C under future reactor conditions. A detailed discussion of the safety aspects of tritium retention follows in the next section 1.3.

The main advantage of selecting tungsten (W) as a plasma facing material is due to its favorable plasma wall interaction properties of low erosion yield by light elements [16] and low hydrogen retention [17]. This property makes W particularly well suited for the divertor region in ITER, where high fluxes of fuel and He particles are expected with typical energies below the W sputtering threshold energy [18]. In the divertor configuration, the contribution to W erosion by fuel isotopes and He ash is therefore limited, but will be dominated by impact of multiply charged low-Z impurities accelerated in the sheath potential [19]. Even in the absence of carbon impurities (e.g. D-T phase in ITER with full W divertor or DEMO), plasma seeding by Argon or Neon will be required for radiative cooling [20], and therefore strict control of the divertor plasma temperature will be necessary to mitigate W erosion and corresponding impact on component lifetime. The disadvantage of tungsten is the high radiative cooling coefficient of tungsten in the plasma core [21], which, in order to meet the Lawson criterion, sets a maximum allowable core W concentration of $\approx 10^{-5}$ [22]. Such low core concentration dictates that the W concentration in the plasma boundary, which is closely related to the W erosion flux, is kept similarly low. However, a high fraction of the sputtered W neutrals were found to promptly re-deposit within one gyro radius [23], limiting the eroded W particle flux into the core plasma. A further disadvantage is the high ductile to brittle transition temperature ($\approx 670\,K$) of tungsten which makes component machining difficult as well as potentially leading to formation of macroscopic cracks due to thermal heat gradients [24]. Further embrittlement by neutron irradiation as well as significant nuclear activation is an issue important for DEMO and therefore subject of ongoing and future research.

In ITER, the worst case erosion mechanism of tungsten is predicted to be from thermal shock induced processes like melt layer ejection or dust formation under high power loads during disruptions (thermal quench) or Type-I ELMs [5] that will significantly affect W component lifetime. The time scale of the thermal energy deposition is typically in the order of milliseconds, and is much shorter than the time required for heat transfer through the material. Therefore, cooling technologies developed [25] will not be able to prevent melting, and techniques for mitigating disruptions and ELMs have to be developed in order to meet ITER requirements of permitting at least 300 disruptions without critical failure [15]. Although tungsten plasma facing materials cannot fully withstand such unmitigated transient thermal loads, the technical solution of meeting ITER requirements for quasi-stationary thermal loads has been successful [10]. The design geometry of W mono-blocks and W macro-brush joined to CuCrZr heat sinks were able to withstand $16 - 20\,MW/m^2$ in heat load tests for 1000 cycles without failure, thus meeting and exceeding ITER specification [10]. This is because from a thermo-physical point of view, tungsten benefits from an extremely high melting point ($3683\,K$), good thermal conductivity of $\approx 140\,Wm^{-1}K^{-1}$ at room temperature, and only a marginal reduction in thermal conductivity with neutron irradiation [24].

1.3 Safety aspects of Tritium operation

Tritium (T) is radioactive and its in-vessel retention is an important issue determining the safety and economy of operation of a future fusion reactor. The safety hazard would be in the form of potential tritium release to the atmosphere in the case of a loss of vacuum. Tritium exposure limits for the population around the reactor site impose a corresponding maximum in-vessel amount (e.g. $< 700\,g$ in ITER [13]). The impact on the economy of operation would be the requirement of interrupting reactor operations once the safety limit was reached in order to recover the T vessel inventory. The frequency of these maintenance interruptions directly impacts the economic feasibility of fusion power generation. Therefore, a viable fusion reactor requires strict control of the T inventory such that the operation cycle can be maintained in cycles of years rather than weeks or months. This requires knowledge on T retention processes as well as of efficient T recovery methods, which are discussed below with emphasis on ITER as the next step fusion device. Experimental data on T retention is limited due to its radioactivity, and most studies have examined the retention behavior using hydrogen and deuterium isotopes. Therefore, the general term hydrogen used in the following discussion, includes retention behavior of all three isotopes.

The importance of T accumulation was realized following the D-T campaigns in the JET [26] and TFTR [27] tokamaks, where 35% and 51% of T was retained in the vessel at the end of each campaign, respectively. By various detritiation procedures, the total amount could be reduced to 10% and 16%, respectively [13]. In both cases, T retention was mainly in the form of T co-deposition with C layers and their resulting decomposition into hydrocarbon flakes formed during material erosion, migration and re-deposition processes. In divertor machines, hydrogen co-deposition was found to occur mainly on the inner divertor surfaces and shadowed areas of the divertor and limiters and a similar pattern is also expected in ITER.

The first step in the co-deposition process is the erosion of the plasma facing material by physical and chemical sputtering processes which will be discussed in sections 2.1 and 2.2, respectively. Following a cycle of deposition and re-erosion, a co-deposition layer can form both on plasma facing sides and remote areas (i.e. not in direct line of sight by the plasma) of the plasma facing material depending on the local deposition conditions. Such remote areas also include the gaps between components, such as the areas between the castellated structure of the W and C plasma facing components planned for use in ITER. Significant amounts of hydrogen can trap in these gap areas and investigations of the trapped amount and modeling of the co-deposition processes is a topic of ongoing research (see Refs. [28, 29, 30, 31]). In case of co-deposition with C, the energy of the incident tritium will be a critical parameter, since energetic hydrogen ions tend to form hard amorphous carbon layers with a H/C concentration of 0.4 (plasma facing areas), while low energy thermal hydrogen leads to the formation of soft layers with H/C concentrations exceeding 1 (plasma shadowed areas). For a typical ITER scenario ($Q = 10$, $400\,sec$ discharge with 50:50% D:T), extrapolation from present day devices operating with full carbon walls have shown that the in-vessel T limit will be reached within a few hundred discharges [13]. This has led to the decision by the ITER-team [32] to replace the CFC divertor strike point tiles to a full W divertor before the onset of D-T campaigns.

For high Z materials, like tungsten, tritium implantation and subsequent diffusion and bulk trapping is the dominant retention process in contrast to co-deposition processes for Be and C. An exception are CFC materials, which due to their porous structure result in significant inwards D diffusion and trapping in cracks between fibers and the CFC matrix [33]. In tungsten, the hydrogen retention behavior typically follows a square root dependence from the incident fluence which results in smaller retention rates compared to co-deposition processes. As a result of this different behavior, it turned out that a Be main wall and a full W divertor will permit 1500 to 5000 discharges before the T in-vessel limit is reached [13]. However, neutron irradiation damage and other defect creating mechanisms (e.g. ion induced damage or He bubbles) can lead to an increase in the square root fluence dependence.

To decrease the T accumulation rate in the vessel during the operational phase of a reactor, various methods of controlled plasma operations are proposed [34], which include isotope tailoring, nitrogen seeding, and pure D plasma operation following D-T operation. The efficiency of T recovery using these methods is limited however, and more efficient methods are required for cleanup. The simplest method of thermal desorption of T by heating the plasma facing components in vacuum would require too high first wall temperature ($\approx 1100\,K$) in the case of C co-deposited layers, but at the reduced temperature ($< 620\,K$) required in the case of Be co-deposited layers or pure W, the method appears feasible [13]. However, reaching the required temperature even for this relaxed condition requires modification to the present ITER divertor bake-out system. Presently, baking in oxygen at atmospheric pressure is the only proven method in removing T co-deposited layers with C. The introduction of O into the vessel will, however, result in corrosion of non plasma facing components. In summary, no single method has been found that can effectively recover all retained T, and therefore a combination of all methods will be needed for efficient in-vessel T management. For the maintenance phase of a reactor, additional recovery methods using local heating by lasers and flashlamps are being studied.

Predicting T retention under ITER conditions remains challenging due to large uncertainties in determining the local deposition conditions. Parameters such as the power and particle fluxes (including impurity fluxes), 3-D geometry effects, and local surface temperature are difficult to measure in existing devices, leading to large

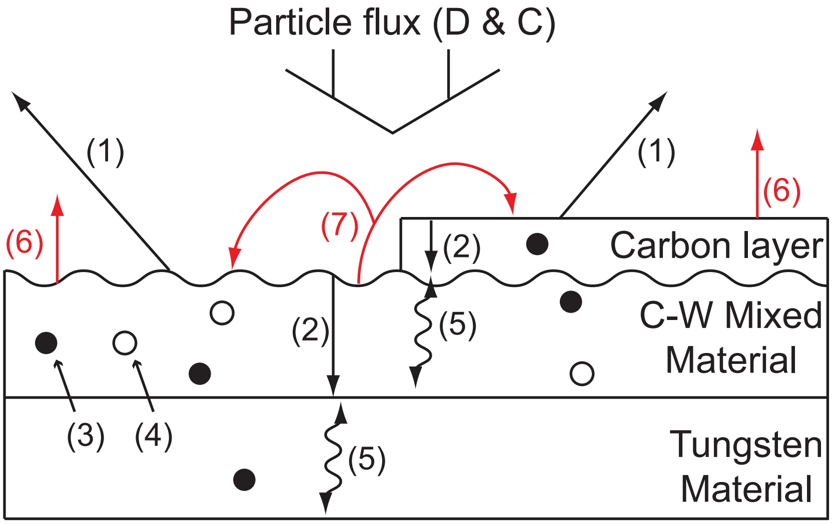

Figure 1.2: Schematic overview of some plasma wall interactions relevant to C-W mixed material or C layer formation: (1) reflection, (2) implantation, (3) D trapping/detrapping or co-deposition (solid circle), (4) carbide formation (open circle), (5) diffusion, (6) sputtering, and (7) redeposition.

uncertainties in extrapolation models. A further complication arises from the use of several different materials in ITER, which results in the formation of mixed materials that strongly affect the local surface composition and behavior of the plasma facing material.

1.4 Carbon-Tungsten mixed materials

A natural consequence of using both carbon and tungsten as plasma facing materials will be the formation of C-W mixed materials by erosion, transport, and redeposition processes. Figure 1.2 gives a schematic overview of these main processes. The question of how such C-W mixed materials affect component lifetime and tritium retention issues requires detailed characterization of the C-W mixed material behavior. Furthermore, there is a need to understand where and how these mixed materials are formed, requiring knowledge of the formation conditions and parameters governing the process. Formation of carbides will also affect both plasma wall interaction processes and thermo-mechanical properties.

The problem of mixed materials can in principle be divided into two main parts: (a) production, and (b) transport of the eroded impurity particles. Here impurity particles are defined as any particle (atoms or molecules both charged or neutral) resulting from plasma wall interaction. Knowledge of transport behavior is necessary to predict both the spatial and temporal distribution of the impurities' key impact parameters. To model the impurity transport in the plasma edge, simulation codes like DIVIMP [35] or ERO [36, 37] are used to follow the eroded particles in a background plasma provided by either a fluid plasma code like B2-EIRENE [38, 39] or a 1D plasma solver based on particle, energy, and momentum conservation [40]. Experimental work in ASDEX-Upgrade [19, 41, 42, 43, 44], using a near full tungsten wall has investigated the W and

C erosion and deposition processes as well as the transport of W inwards and inside the bulk plasma. Additional tokamak relevant transport studies are planned with the ITER-like wall project at JET [45, 46]. The confidence in simulation results and quality of predictions to future experiments not only depend on accurate knowledge of the plasma parameters but also in accurately modeling the plasma wall interactions, particularly with respect to the production of impurity particles.

To model plasma wall interactions, the codes use approximations based on semi-empirical formulas (described in more detail in section 2) derived from numerous laboratory experiments and/or kinetic transport codes for ions in matter like TRIM.SP [47] or TRIDYN [48]. However to date, the implementation of the plasma wall interactions in the transport codes is restricted to processes with pure materials. The treatment of mixed materials in simulations have relied on the most simple model of linearly scaling the pure materials' behavior by their respective concentrations in the mixed material. However, this approximation completely neglects the sophisticated and often complex synergistic mixing processes by assuming that the mixed material behavior is linearly dependent of its constituent species. An analytic model of material erosion for multiple impurity species clearly shows that this is not the case exhibiting complex non-linear behavior [49]. To address such concerns, there has been recently a concentrated effort in the fusion community to understand the basic development and behavior of mixed materials under well controlled laboratory conditions. For a recent review of the experiments, see Ref. [50].

In fusion devices using carbon and tungsten as plasma facing materials, C impurities impinge on the W surface with a certain energy and angular distribution along with hydrogen, resulting in the formation of C-W mixed materials. Such mixed C-W layers and C layers have been observed at ASDEX-Upgrade divertor tiles [51] and in TEXTOR limiter experiments [52, 53] distinguished by a clear division between areas of continuous W erosion and C deposition [52, 54]. In ASDEX-Upgrade, the whole outer divertor area was found to be a net erosion area for C and W, in contrast to net deposition areas in the inner divertor [43, 55]. W and Si markers used in the divertor plates in ASDEX-Upgrade showed that the carbon impurity concentration in the incident flux (f_c) is an important parameter in determining erosion behavior [23]. Modeling of the erosion and deposition behavior of TEXTOR test limiters indicates a strong dependence on plasma temperature [56, 57]. A recent experiment highlights the importance of surface roughness in determining C deposition behavior [58]. In addition, formation of various carbides are also observed from post-mortem analysis of TEXTOR limiter tiles [59]. To understand the main parameters and mechanisms governing such behavior, laboratory experiments have been performed at IPP [60, 61, 62, 63, 64, 65, 66]. Analytical model [65] and TRIDYN studies [60, 62] based on CH_3^+ experiments have shown a fluence dependency of the transition between erosion and deposition. The competition of erosion and deposition processes from simultaneous bombardment of W surfaces with both hydrogen and carbon ions was significantly different from H- or C-only bombardment [60, 62, 65, 67]. However in CH_3^+ experiments, the C fraction in the incident flux is fixed and access to this key parameter requires an experimental setup where f_c can be varied. Recently, a dual beam experiment with two independent ion sources has been commissioned [68] that allows for variation of f_c.

1.5 Thesis purpose and direction

The first step in the chain of processes determining the component lifetime and tritium retention by co-deposition is *erosion* of the plasma facing material. The second step is the transport and *redeposition* of the eroded materials resulting in mixed material formation. Local deposition conditions will dictate whether the deposited material will be re-eroded or remain deposited. In areas that are continuously eroded, the component lifetime issues will increase in importance, whereas in areas of continuous deposition, the tritium retention issue will become dominant. The combined effects integrated over the entire vessel will determine which issue will become the limiting factor in the operation of a fusion reactor. To reliably predict these effects will require a clear understanding of the local processes that govern the plasma facing material behavior under simultaneous impact of fuel and impurity species. Specifically in the framework of ITER, knowledge on the behavior of C and W materials is required to achieve this goal.

Therefore this thesis is intended to better understand the *local* formation dynamics of C-W mixed materials and characterize its behavior under simultaneous C-D ion irradiation. The experimental approach chosen is to follow the evolution from a pure W surface under simultaneous irradiation by D and C to a steady state condition, while characterizing the W erosion, C implantation, and D retention behavior. The major goals are: (a) to elucidate the main mechanisms affecting the dynamics and to identify synergistic effects, (b) characterize the evolution and behavior of the C-W mixed material, and (c) parametrize the C-W mixed material system to provide accurate data for benchmarking of simulation codes. The latter includes also the validation of the model assumptions in the code simulations and the identification of processes, which are not covered by the model, leading to discrepancies between simulation and experiment. The ultimate goal of this is to improve the accuracy and confidence level for erosion and deposition processes and its impact on predictions of carbon and tungsten components lifetime behavior and tritium retention under exposure to a plasma containing impurity elements.

The start of this project came shortly after the completion of room temperature (*RT*) experiments investigating the simultaneous irradiation of W by deuterium and carbon ions using the IPP dual beam experiment [69, 70, 71]. Significant deviation of the prediction of the transition point between erosion and deposition regimes from comparing *RT* experimental results with simulations was found. In particular, the contribution of surface roughness from chemical sputtering processes could not be separated while the previously observed synergistic effect of W erosion yield being greater than the sum of the C and H sputter yields [65] still remained unclear. Furthermore, experimental data at elevated temperatures during simultaneous irradiation were very limited.

The main parameters varied in the experiments are the C fraction in the incident flux, target material temperature, and the incident D energy. A systematic attempt has been made to obtain a complete set of experimental results at *RT* with respect to the C fraction in the incident flux to identify the transition point from erosion to deposition regimes. The experiment is then taken to divertor relevant temperatures at $670\,K \rightarrow 870\,K$ [72] to elucidate the effects of C self-sputtering and chemical sputtering processes that are temperature dependent. Results from C self-sputtering experiments are used to benchmark surface binding energies ($SBEs$) used in TRIDYN [48], which critically determine the C sputter yields in simulations. Lastly, the incident D energy is lowered to observe the energy dependence of chemical sputtering [73] and its impact on the dynamics so far studied; an emphasis is placed on determining whether chemical sputtering occurs in C-W mixed materials. A simple model based on TRIDYN is developed to isolate the chemical contribution and quantify its amount. The structure of this work is summarized in Fig. 1.3 and an attempt has been made to increase our understanding of the following main points:

- Dynamics of C-W mixed material formation
- Erosion behavior of C-W mixed material
- Hydrogen retention in C-W mixed material

during simultaneous irradiation of tungsten by deuterium and carbon ions.

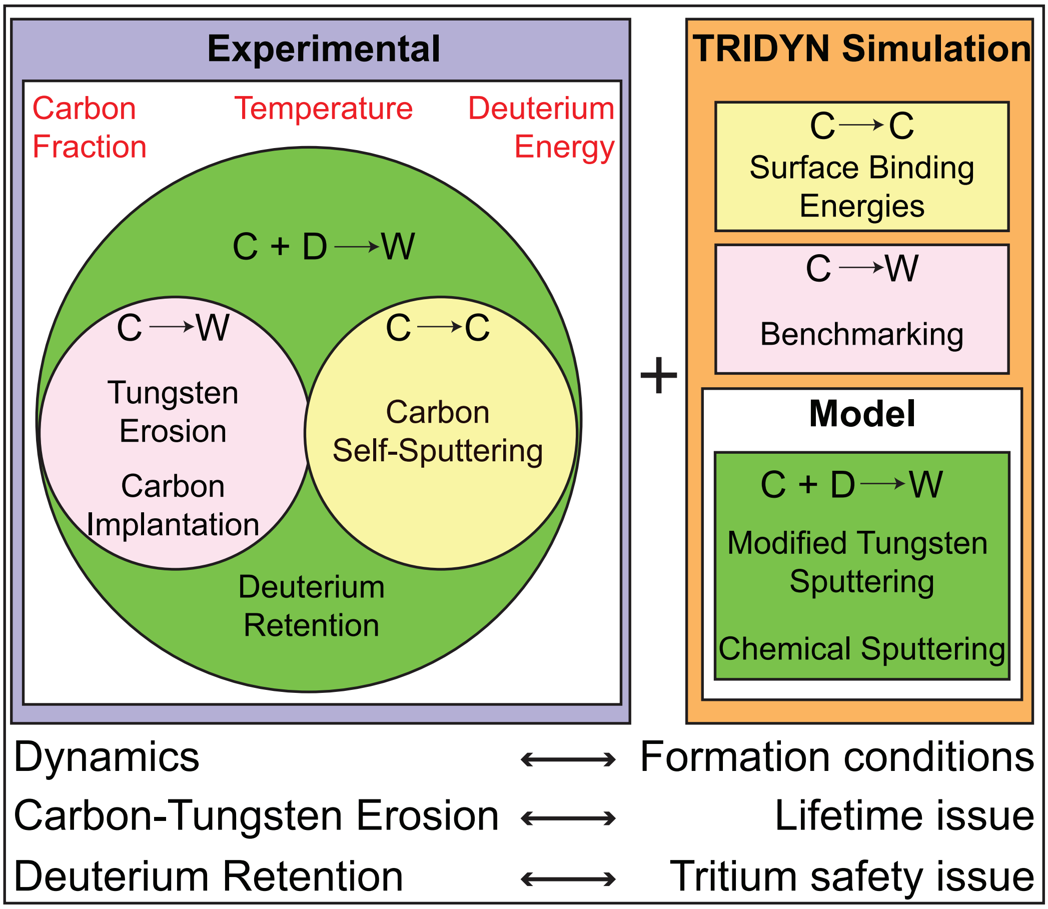
Experimental
Carbon Fraction
Temperature
Deuterium Energy
C + D ⟶ W
C ⟶ W
Tungsten Erosion
Carbon Implantation
C ⟶ C
Carbon Self-Sputtering
Deuterium Retention
+
TRIDYN Simulation
C ⟶ C
Surface Binding Energies
C ⟶ W
Benchmarking
Model
C + D ⟶ W
Modified Tungsten Sputtering
Chemical Sputtering
Dynamics ⟷ Formation conditions
Carbon-Tungsten Erosion ⟷ Lifetime issue
Deuterium Retention ⟷ Tritium safety issue

Figure 1.3: This thesis combines experimental and simulation work to achieve three main objectives. Investigations of: (a) the dynamics of C-W mixed material formation and its dependence on parameter variation (C fraction in the incident flux, temperature, and incident D energy), (b) erosion behavior of C-W mixed materials and implication to component lifetime issue, and (c) D retention behavior with implication to tritium safety issue.

2 Background

The processes studied in this thesis involve complicated dynamic kinematic and chemical interactions between the incident deuterium (D) and carbon (C) species with the tungsten (W) target. At this point, it is appropriate to introduce the following definitions of physical and chemical sputtering: *Physical sputtering* is the ejection of target atoms resulting from momentum transfer between the incident energetic particles and the target atoms. Because the scattering processes between incident projectile and target atoms are at energies much higher than thermal energies (keV vs. $0.01 - 0.1\,eV$), this process is independent of temperature. *Chemical sputtering* is the production of volatile species by chemical reactions *induced* by incident energetic particles that occur either at the surface or deeper in the material [74]. *Chemical erosion* is defined as the release of volatile species due to chemical reactions of a neutral or thermal incident species directly with the target atoms. Both chemical sputtering and erosion processes have a strong temperature dependence. In carbon materials, an additional effect at high temperature occurs during irradiation known as Radiation-Enhanced Sublimation (RES) [75]. The suggested mechanism involves the formation of C interstitials from ion irradiation, that diffuse to the surface and are sputtered easily due to weak surface binding energies [76]. Fig. 2.1 illustrates the temperature dependent erosion processes in carbon from hydrogen irradiation.

Due to the use of incident species above the threshold energy of both C and W in this study, physical sputtering is the dominant process observed in most experiments. A description of the analytic and computational methods developed to describe the physical sputtering process is presented in section 2.1. Next, background on chemical sputtering and erosion processes are summarized in section 2.2. Considerable data exist in the literature for physical and chemical sputtering processes in C and W. Therefore, references to the most recently compiled reviews are provided at the beginning of each section, and here, only the most pertaining aspects are discussed. Finally, recent understandings in C-W mixed materials involving simultaneous irradiation experiments and hydrogen retention will be summarized in section 2.3.

2.1 Physical sputtering

A complete treatment of both theoretical and experimental aspects of physical sputtering is found in Refs. [77, 78, 79]. Physical sputtering requires the transfer of kinetic energy from the incident particles to the target atoms. The elastic energy transferred between two colliding particles is described by a kinematic factor $4M_1M_2/(M_1+M_2)^2$, dependent on the masses of the colliding atoms. The elementary process for this energy transfer is a cascade of elastic collisions between the incident particle and target atoms. These recoil atoms undergo further collisions until they finally come at rest by energy transfer to the crystal lattice. Only atoms that have acquired enough kinetic energy to overcome the target's surface binding energy are sputtered. Therefore, physical sputtering is characterized by a threshold energy, E_{th}, at which point no more sputtering takes place.

Analytical physical sputtering theory has been developed primarily in the approach of predicting the sputtered amount as a function of target element, projectile element,

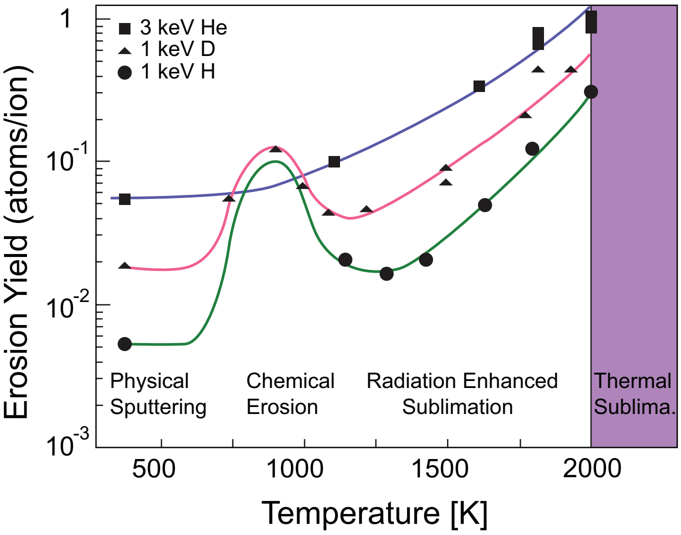

Figure 2.1: Temperature dependent erosion processes for carbon (from Ref. [75]).

projectile energy and angle of incidence, without explicit reference to the details of the recoil cascade. The principal quantity is the sputter yield Y_a^b, defined as the mean number of target a atoms removed from the surface of a solid per incident projectile b:

$$Y_a^b = \frac{atoms\ removed}{incident\ particle}$$

The processes related to sputtering only occur in a layer of thickness Δx_o, which is a function of the mean projectile range and typical dimension of the resulting collision cascade [79]. The rate of recoil atoms generated in this layer is proportional to the energy deposited per unit depth of the incident particle. This is quantitatively described by the nuclear stopping cross section which is defined as the mean energy lost from elastic collisions per unit path length. Therefore, the sputter yield can be described as a function of the stopping power and incident particle energy. For normal incidence ($\alpha = 0°$), Bohdansky derived a formula [80] based on Sigmund's analytic theory [78]:

$$Y_{phys}(E_o, \alpha = 0°) = Q s_n^{TF}(\varepsilon)\left(1 - \left(\frac{E_{th}}{E_o}\right)^{\frac{2}{3}}\right)\left(1 - \frac{E_{th}}{E_o}\right)^2 \qquad (2.1)$$

where E_o is the incident particle energy, E_{th} is the threshold energy, α the angle of incidence, $s_n^{TF}$the Thomas-Fermi nuclear stopping cross section, Q a fitting parameter that determines the maximum of the yield curve, and ε the reduced energy:

$$\varepsilon = \frac{E_o}{E_{TF}} \qquad with \qquad E_{TF}(eV) = 30.74\frac{M_1 + M_2}{M_2} Z_1 Z_2 (Z_1^{2/3} + Z_2^{2/3})^{1/2}$$

Recently, the formula has been revised to replace s_n^{TF} by one based on the Kr-C potential [81] known as the revised Bohdansky formula [82]. The angular dependence of the sputtering yield is described by the analytic formula proposed by Yamamura [83]:

$$Y_{phys}(E_o, \alpha) = \frac{e^{(f[1-1/cos\alpha]cos\alpha_{opt})}}{cos^f\alpha} Y_{phys}(E_o, \alpha = 0°) \tag{2.2}$$

here $Y_{phys}(E_o, \alpha)$ is the yield at an ion energy, E_o, and nominal angle of incidence α while f and α_{opt} are fitting parameters to experimental data and can be taken from published tables [16] or from the formula in Ref. [83]. For detailed discussions of these analytical models and comparison to experimental results see Refs. [16, 82].

For an improved treatment of sputtering by considering the details of the recoil cascade, one has to rely on computer simulations. Two main methods are used, the molecular dynamics (MD) approach where the movement of target atoms is studied as a function of time taking the interaction of all neighboring atoms into account, and the binary collision approximation (BCA) where the movement of projectile and target atom collision partners is treated as as series of successive binary collisions. MD simulations are best suited for low energies but require long computational times, and in most cases is used to study principal processes, where also the target lattice structure and chemical processes are of importance. BCA simulations are much faster, and are widely used to calculate sputtering yields where mainly kinematic scattering processes are involved. The strength of such simulations is that they provide access to additional information, like partial sputter yields coupled with surface concentration and depth profiles, that are normally not all accessible simultaneously in experiments. For a comprehensive description of computational methods and their applications to ion solid interactions see Ref. [77]. For this study, only the Monte-Carlo program TRIDYN [48] based on the BCA was used and a short description of the program follows.

2.1.1 TRIDYN

TRIDYN is an extension of the static program (no changes to target composition under irradiation) TRIM.SP [47] based on the binary collision approximation (BCA) for an amorphous target with dynamic update of the changing surface and target composition within the incident projectile range. The name "Monte-Carlo" arises from the assumption that the material is amorphous, and therefore the next collision partner can be determined by a random selection process. Three variables are required that are chosen randomly: 1) λ, the distance between successive collisions, 2) b, the impact

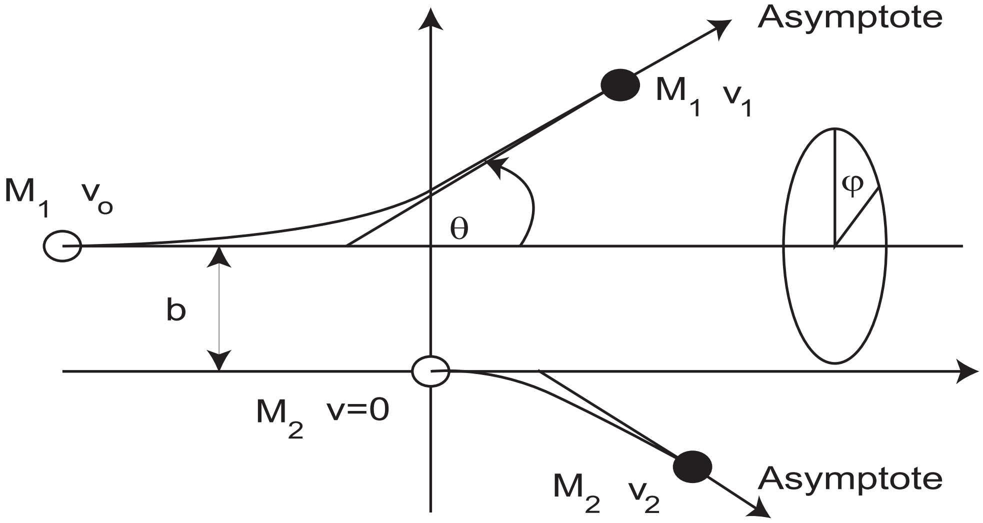

Figure 2.2: Definition of impact parameter b, scattering angle θ, and the azimuthal scattering angle, φ in the laboratory framework.

parameter, and 3) φ, the azimuthal scattering angle (see Fig. 2.2). For λ, the liquid model is used [77]:

$$\lambda = N^{-\frac{1}{3}}$$

where N is the target number density in units of $\left[\frac{atoms}{cm^3}\right]$. For b, the following relationship is used:

$$b = b_{max}\sqrt{R}$$

where b_{max} is the maximum impact parameter corresponding to a minimum scattering angle, and R is a random number between 0 and 1. To determine, b_{max}, a cylindrical volume, V, in which a collision event can occur is defined:

$$VN = 1 = \pi b_{max}^2 \lambda N$$

resulting in:

$$b_{max} = (\pi\lambda N)^{-\frac{1}{2}}$$

Finally, φ can be determined using the following relationship from symmetry argument:

$$\varphi = 2\pi R$$

where R is again a so-called random number between 0 and 1. The scattering angle θ, is approximated using the "magic formula" [84] and the change in particle direction from the collision is taken from the asymptote of the real trajectory (see Fig. 2.2). The Kr-C potential [81] is used as the interaction potential between colliding particles, which is valid down to ion energies of $\approx 50\,eV$. Therefore, TRIDYN calculations can be used to simulate ion-solid interactions relevant to particle energies expected in the ITER divertor. The inelastic electronic energy loss as the particles move through the target is calculated using an equipartition of the Lindhard-Scharff [85] and the Oen-Robinson [86] interactions.

The process begins with a projectile whose collision partner (PKA: primary knock-on atom) is determined by the randomized b and φ. The "magic formula" then delivers the scattering angle in the center of mass frame, from which the scattering angle of the projectile and the PKA is determined in the laboratory frame. The energy changes are assigned and the program follows the PKA (labeled i), as it starts its own cascade resulting in secondary knock-on atoms (SKA). The resulting SKA created are also labeled i and the information stored, while the PKA is incremented to $i + 1$. Subsequent collisions will further increment the PKA as well as the SKA. When, after several collisions the PKA is sputtered, transmitted, or stopped, the program returns to the last SKA labeled i and follows this SKA like the PKA. Finally, after treatment of all SKA's (i.e. i, $i + 1$, etc.) created by the first PKA, the program returns to the initial projectile and follows it to its next collision and the cycle repeats.

To account for changes in target composition, the program divides the target into layers of initially constant thickness. After following a certain number of projectiles, the local excess or loss in the layer composition is allowed to relax by adjustment of the layer thickness. The layers are kept within a certain thickness range, such that thin layers will merge and thick layers will split. Following this relaxation cycle, the projectile loop begins once more. In TRIDYN, information on the surface recession or growth, sputtering and reflection yields, depth distributions, and surface and target composition as a function of incident particle fluence can be obtained. The surface binding of target surface atoms is described by a planar potential and in general, the heat of sublimation values are taken as surface binding energies ($SBEs$). All simulations results presented in this thesis were calculated using Version 40.1 [48] unless otherwise stated.

2.1.2 Carbon and Tungsten sputtering by Carbon

C-C: Experimental carbon (C) self-sputtering yields were determined via weight-loss measurements [87] or by surface collector method [88]. However there is a lack of experimental data in the temperature range $RT < T \leq 870\,K$ and will be the focus of this work. For the incident angle $\alpha = 15°$ used in this thesis, the C self-sputtering yield is below unity for all impact energies [89]. Therefore, in the case of C-only irradiation, a C layer will always grow on a C surface. The reflection yield is negligibly small for energies above $100\,eV$ compared to the sputter yield [90].

C-W: Results of first laboratory controlled experiments examining the fluence dependence of tungsten (W) sputtering by $E_c = 1\,keV$ and $E_c = 6\,keV$ C ions at RT using in-situ weight-loss measurements are presented in Ref. [61]. Initially, weight-loss is observed at low fluences in accordance to Y_w^c calculated with TRIM.SP [47] (not taking into account the implanted C concentration), but this trend reverses to weight gain at higher fluences. Steady state conditions are reached when the negative yield given by the slope of the weight change becomes constant with increasing fluence. The initial weight-loss due to W sputtering is gradually reduced by the gradual increase of the implanted C fraction, ultimately forming a protective C layer which suppresses further sputtering of W. During this process, the weight of the growing C layer eventually becomes larger than the weight of the sputtered W, resulting in the observed continuous increase. This weight-loss/gain behavior was found to depend strongly on the angle of incidence. From $\alpha = 70°$, the behavior switches to continuous weight-loss by W sputtering due to increased C self-sputtering and reflection yields that prevents the formation of a closed C layer. A parameter scan of α in TRIDYN showed that the partial sputter yield of W increases monotonically with α, while the partial sputter yield of C reaches a maximum around $\alpha = 40°$. Therefore, the C coverage of the surface was identified as an important parameter in determining W sputtering behavior. For the situation where a carbon layer greater than the depth range of incident C ion develops, the system behavior was observed to shift from a C-W to C-C interaction. Consequently, the partial sputter yield of carbon was observed to approach the experimentally determined C self-sputtering yields [90] in TRIDYN simulations.

A subsequent study examined the effect of elevated temperature using $E_c = 2.4\,keV$ C ions at normal incidence [63]. A trend of increased weight-loss was observed with increasing temperature. The results were interpreted as increased W sputtering due to C loss from the surface by diffusion into the W bulk material. TRIDYN calculations iteratively coupled with the diffusion program PIDAT [91] indicated that diffusion is negligible at (or below) $673\,K$ and only becomes significant for $T > 850\,K$. However, to obtain a good fit to the experimental data, higher values of the diffusion coefficient than the literature data [92] were required for $773\,K$ and lower values than in the literature for $973\,K$. The resulting temperature dependency of D exhibited a smaller slope with temperature compared to literature values, which was attributed to effects of C trapping and tungsten carbide formation. To improve upon these findings, the concentration dependent diffusion coefficient $D(C)$ was determined in a separate experiment [66, 93] by Boltzmann Matano analysis of measured C depth profiles and found to be of the order of $10^{-19}\,m^2s^{-1}$ to $10^{-21}\,m^2s^{-1}$. Based on these results, a new program, DIFFUSEDC, was developed and successfully tested [93]. $D(C)$ was found to decrease at higher C concentrations due to a shift of C diffusion in tungsten to C diffusion in W_2C, WC, and even graphite where the diffusion coefficient was negligible in the considered temperature range below $1100\,K$ [94]. A follow up experiment examining both effects of increased C self-sputtering (RES) and diffusion with temperature found that the C fluence dependence of the measured weight-loss was well reproduced by simulation results [60], confirming the temperature dependence model of diffusion and

	$E_D = 0.5\,keV$	$E_D = 0.7\,keV$	$E_D = 1\,keV$	$E_D = 3\,keV$	$E_c = 6\,keV$
Tungsten	0.0014	0.0028	0.0044	0.0085 (0.0098)	0.4
Carbon	0.029	0.028	0.026	0.017 (0.010)	0.264 (0.29)

Table 2.1: Calculated sputter yields using the revised Bohdansky formula at RT and $\alpha = 15°$. Also included are the experimentally measured sputter yields using the dual beam experiment in this study for $E_D = 3\,keV$ (in brackets).

RES used at $T > 1000\,K$. It should be noted that in the present work the temperature range studied is below the temperature in which carbon diffusion in tungsten is observed and therefore diffusive behavior is not treated.

2.1.3 Tungsten and Carbon sputtering by Deuterium

Physical sputtering of carbon (C) and tungsten (W) by deuterium (D) is in general well described by TRIDYN or by using the revised Bohdansky formula. The deviation between calculated and experimental results from weight-loss experiments is normally a factor of two (see Ref. [16]). The calculated W sputter yield by $E_D = 3\,keV$ D ions is 0.0085, which is in good agreement with the improved experimental yield of 0.0098 measured using the present dual beam experiment [95]. The calculated C sputter yield is 0.017 while the experimental total yield measured in this study (physical *and* chemical sputtering yields) at RT is 0.010. A summary of the carbon and tungsten sputter yields calculated by using the revised Bohdansky formula is shown in Table 2.1.

In the case of tungsten carbides, preferential sputtering of the C is observed due to the large difference in mass ratio between carbon and tungsten atoms [96], which is in good agreement with TRIDYN simulations. Also, field ion microscope measurements show similar threshold energies of $150\,eV$ for tungsten sputtering from a mixed C-W layer [97] as predicted from TRIDYN simulations.

2.2 Chemical erosion and sputtering of Carbon

Carbon (C) has the additional property of being eroded by incident hydrogen or oxygen species well below the threshold energy of physical sputtering. The chemical sputtering and erosion of C in context of plasma facing materials in fusion research is covered in reviews by Roth [98] and Vietzke and Haasz [99]. Like physical sputtering, the chemical erosion or sputtering yield is defined by the ratio of removed carbon atoms per incident species. In most experiments, the carbon loss is measured via weight-loss measurements or mass spectrometry. The advantage of weight-loss measurements is the ability to quantify the total erosion, while mass spectrometry offers insight into the elementary steps of the reaction process but has limited accuracy for quantification of the total erosion yield. The isotopic effect expressed by the ratio of the respective yields has a nominal value of $Y_c^D/Y_c^H = 1.5$ [100], indicating chemical sputtering and erosion processes by tritium species will not be significantly different from deuterium species.

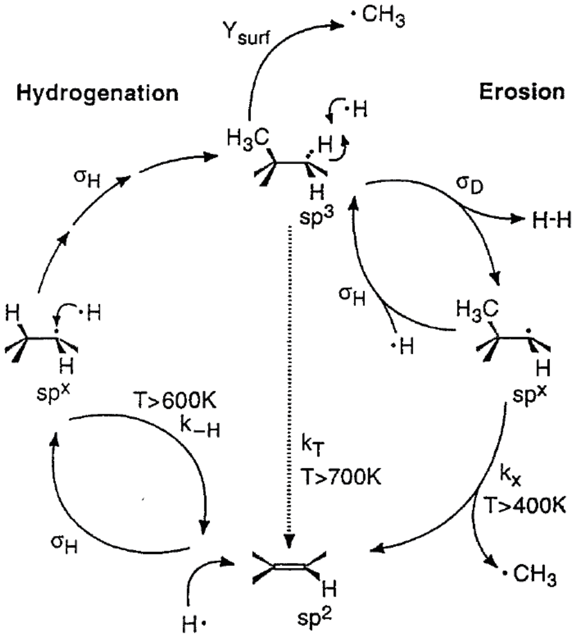

Figure 2.3: Chemical erosion cycle (from Ref. [110]).

The governing mechanisms behind *chemical erosion* is the balance between hydrogenation [101] of unsaturated carbon atoms at the surface and hydrogen abstraction [102]. Two main erosion steps were determined from the interaction of atomic hydrogen with a thin amorphous hydrogenated carbon layer (a-C:H). First, kinetic or thermal [103] ejection of surface hydrocarbon groups can occur due to the breaking of C-C_iH_j bonds. This is illustrated by the Y_{surf} arrow (kinetic) and Y_{therm} center arrow (thermal) in Fig. 2.3, respectively. The second, more complex process is the thermally activated de-excitation of a radical sp^x carbon site resulting in a split-off of a neighboring methyl group [104]; as seen from the erosion cycle in Fig. 2.3. Although CH_3 and CH_4 are the main species ejected from the surface, a wide distribution of heavier hydrocarbons is also observed [105]. Amorphous carbon materials were found to have higher erosion yields in comparison to ordered materials from the increased availability of hydrogenation sites [106].

The entire cycle is initiated from the hydrogenation of sp^2 to sp^3 carbon sites via an intermediate radical stage sp^x, which is not temperature dependent but proportional to an empirical cross section σ_H. Further hydrogen irradiation with temperature increase above $400\,K$ results in chemical erosion where stable hydrocarbon complexes desorb with a rate constant k_x via an intermediate radical stage sp^x. However at temperatures above $600\,K$, hydrogen recombines with a rate $k_{\_H}$ which interrupts the hydrogenation process, resulting in a decrease in sp^3 concentration and correspondingly the chemical erosion yield. This is the reason why in experiments, a maximum erosion yield between $700 - 900\,K$ is observed [107]. It is found that this maximum temperature shifts to higher temperatures with increasing hydrogen flux [108] and energy [73, 109]. A detailed review of the hydrogen surface chemistry is discussed in Ref. [106].

The chemical reaction of energetic hydrogen ions with carbon atoms was found to occur after the ions have slowed down (to thermalised ions) at the limit of their implantation range [110, 111, 112]. Therefore, the above chemical erosion model of thermal hydrogen atoms can also be applied for the case of energetic incident ions. The main difference lies in the additional damage created by the incident energetic ions which can enhance both Y_{surf} and Y_{therm} by energy deposition in the near surface layer. Incorporating both processes, one can derive an analytical description of the total chemical yield that reproduces the measured temperature ($T[K]$), incident energy ($E_o[eV]$), and flux ($\phi[ions/m^2s]$) dependencies of the chemical erosion yield [73]:

$$Y_{chem} = Y_{surf} + Y_{therm}(1 + D\,Y_{dam})$$

where D is a parameter depending on the hydrogen isotope and Y_{dam} is equivalent to Eqn. 2.1 with the threshold energy E_{th} replaced by a damage activation energy $E_{dam}[eV]$ derived from experiment [113]. Y_{therm} and Y_{surf} are given by the following expressions:

$$Y_{therm} = c^{sp^3}\frac{0.033exp\left(\frac{-E_{therm}}{kT}\right)}{2\times10^{-32}\phi + exp\left(\frac{-E_{therm}}{kT}\right)}$$

$$Y_{surf}(E_o,T) = c^{sp^3}\frac{Y_{des}(E_o)}{\left[1 + exp\left(\frac{E_o - 65eV}{40eV}\right)\right]}$$

where $E_{therm}[eV]$ is the thermal activation energy, Y_{des} is equivalent to Eqn. 2.1 with the threshold energy, E_{th}, replaced by an empirical desorption activation energy [114], $E_{des}[eV]$, and $c^{sp^3}$is the hydrogenated carbon concentration given by:

$$c^{sp^3} = \frac{C\left[2\times10^{-32}\phi + exp\left(\frac{-E_{therm}}{kT}\right)\right]}{2\times10^{-32}\phi + \left[1 + \frac{2\times10^{29}}{\phi}exp\left(\frac{-E_{rel}}{kT}\right)\right]exp\left(\frac{-E_{therm}}{kT}\right)}$$

where $E_{rel}[eV]$ is the activation energy for hydrogen release [115, 116] and C is given by:

$$C = \frac{1}{1 + 3\times10^{7}exp\left(\frac{-1.4eV}{kT}\right)}$$

Therefore, the chemical erosion cycle of carbon irradiated by low energy ions is composed of: (1) the reaction of thermalised ions, and (2) the enhancement of the thermal reaction by radiation damage, in combination with (3) the enhanced ion induced desorption of hydrocarbon radicals on the surface. A similar modification of the atomistic model was presented by Mech et al. [113].

However at RT where thermal erosion mechanism can be excluded, the chemical erosion yield could not be correctly explained by the sputtering of weakly bound hydrocarbons from the surface only (Y_{surf}) [117]. Instead, a chemical sputtering mechanism was proposed, where energetic ions break C-C bonds within their penetration range and the resulting dangling bonds are passivated by hydrogen atoms. Consecutive bond breaking and passivation results in the formation and release of hydrocarbons at and below the surface. The main difference of the chemical sputtering model is the fact that the process is not surface limited and requires breaking of C-C bonds by energetic particles. The energy dependence of the chemical sputter yield could be well reproduced by this model for simultaneous irradiation of atomic hydrogen and low energy ions [117, 118, 119, 120]. In support of the chemical sputtering mechanism, molecular dynamic studies [121, 122] showed that a hydrogenic ion can attack the region between two C atoms, resulting in core-core repulsion between the ion and the C atoms. At short inter-atomic distances the repulsive interaction was found to push the two C atoms apart breaking the covalent C-C bonds.

2.3 Simultaneous irradiation of Tungsten by Hydrogen and Carbon

To study C-W mixed materials, it is important to investigate the simultaneous bombardment of both hydrogen and carbon together. The primary reason is that during simultaneous bombardment, the surface composition is subject to the balance of implantation and erosion processes of both species. On the one hand, the implantation of carbon can be balanced by C removal due to sputtering and/or diffusion, resulting in continuous tungsten erosion. On the other hand, C implantation may prevail over the sputtering process, resulting in C layer formation on top of the C-W mixed material. The dominating behavior will depend on both the kinematic and chemical processes outlined in sections 2.1 and 2.2, as well as target properties like surface morphology (e.g. roughness) and temperature which have a significant effect on carbon diffusion and tungsten carbide formation. Single species irradiation of prepared C-W mixed materials cannot correctly describe such a system since only one species can be represented at one time.

2.3.1 Tungsten sputtering and Carbon surface behavior

To simulate simultaneous irradiation of carbon and hydrogen in previous experiments, polished tungsten targets were bombarded with $E_{CH_3^+} = 3\,keV$ CH_3^+ ions and the sputtering behavior studied by in-situ weight-loss measurements [62]. Large deviations from TRIDYN calculations resulted in the formulation of an analytical model based on balancing the erosion-deposition processes in Ref. [65]. The resulting erosion yields required to fit the experimental data by the model could not be explained by the superposition of carbon self-sputtering and the additional erosion due to hydrogen impact. However both experiments suffered from surface roughness and effects of non-uniform bombardment over the irradiated area. Recently, improvements to the experimental technique by replacing the in-situ weight-loss measurements with in-situ ion beam analysis has allowed to achieve good quantitative agreement between experimental results and TRIDYN simulations in case of smooth surfaces [70]. Chemical sputtering effects were considered negligible with surface roughness being the dominant parameter governing the erosion and deposition process [123]. A separate high temperature experiment using $E_{CH_3^+} = 3\,keV$ CH_3^+ ions at $T = 1000\,K$ was performed by Schmid and Roth [60], and a model combining the effects of RES and diffusion was able to reproduce the experimental weight-loss/gain results.

The carbon surface concentration was investigated as a function of temperature and carbon fraction in the incident particle flux, f_c, using a mixed beam of $E_{H_3^+} = 1\,keV$ H_3^+ ions and $1\,keV$ CH_x^+ and $C_2H_x^+$ ions (>80% and $<$ 20%, respectively) in Refs. [67, 124]. An increase in C surface concentration was observed by increasing the f_c from 0.1% to 0.8%, while a slight expansion of the C depth profile was observed by increasing the temperature from $653\,K$ to $913\,K$. In the corresponding C depth profiles, a local peak at $\approx 20\,nm$ was observed (greater than the ion range of $\approx 5\,nm$), which was explained as an effect of recoil implantation of the carbon deeper into the implantation range [125].

2.3.2 Sputtering of C-W mixed materials by Deuterium

A very weak temperature dependence was observed for methane release in tungsten carbide irradiated with $E_D = 1.5\,keV$ D^+ ions that is significantly different from the $800 - 900\,K$ peak observed in graphite [126]. Interestingly, methane release was also observed at RT following an initial D buildup phase. The total sputtering yield was observed to decrease with increasing W concentration in the C-W mixed material [127]. The D energy used ($E_D = 66\,eV$) was below the threshold of W sputtering, and therefore, the weight-loss of the specimens was attributed to the preferential loss of carbon by physical and chemical sputtering processes. Such preferential loss of carbon was also observed for $E_D = 1\,keV$ D^+ion irradiation of tungsten carbide specimens [96], with good agreement between experimental results and TRIDYN simulations. The preferential carbon erosion behavior was interpreted to be due to threshold effects caused by the large mass ratio between carbon and tungsten atoms.

2.3.3 Hydrogen retention in Carbon and Tungsten materials

A recent review of hydrogen retention in plasma facing materials planned for ITER has been compiled in Refs. [128, 129]. Significant deuterium (D) retention is observed in co-deposited layers on tungsten (W) divertor tiles in ASDEX-Upgrade [130]. A detailed review of hydrogen retention in bulk W materials can be found in Refs. [17, 131], and for carbon (C) materials in Ref. [132]. In general, hydrogen trapping in C is much larger than in W. The following discussion summarizes the relevant results of hydrogen retention in C-W mixed materials.

The methods used to study hydrogen retention in C-W mixed materials has been

D irradiation of tungsten carbide materials [126, 133, 134, 135, 136], C-W mixtures prepared before the D irradiation step [137, 138], or by C pre-implantation followed by D irradiation [139, 140, 141]. In all cases, the hydrogen retention behavior was found to strongly depend on the C concentration in the material. It is postulated that the amount of active C with free bonds is the critical parameter determining the hydrogen retention behavior, but such measurements have not been performed experimentally. A decrease in hydrogen retention from absorption experiments is observed with increasing carbonization of tungsten [142], illustrating the fact that when stable C bonds are formed, hydrogen retention decreases. However, D irradiation of tungsten carbide at RT results in D retention similar to levels observed in graphite, and decreasing to levels of pure W with increasing temperatures [126]. Thus, irradiation of stable tungsten carbides may result in C bond breaking that activate C sites which trap hydrogen more effectively than W trap sites. Thermal desorption spectra indicate two regions of D release between $300-700\,K$ and $900-1100\,K$, respectively [126, 135, 136, 143, 137]. With increasing W concentration, an increase in D release between $300-700\,K$ is observed [137]. Therefore, the lower temperature region is generally associated with D de-trapping from tungsten traps, while the higher temperature region is associated with D de-trapping from carbon traps. Deuterium depth profiles reveal that the near-surface layers in tungsten carbides retain twice as much D than poly-crystal tungsten [128] with no saturation effects [134]. This is in direct contrast to hydrogen retention in C, where saturation occurs due to the low diffusivity of D in carbon. The increased trapping in the near-surface region results in a decrease of the long D diffusion tail characteristic of pure W, but is still in the order of several μm. The fact that hydrogen retention in tungsten carbides follow the temperature behavior of pure W is due to the lower activation energy for recombination and faster diffusion of D than C [144]. There is also evidence that D is trapped solely as D atoms in tungsten carbides in contrast to both D atoms and D_2 molecules in pure W [128, 133, 145]. It is postulated that this occurs due to the reduction of the recombination coefficient of the C-W mixed material surface [139].

In the case of C pre-implantation, significant C and D fluence dependencies are observed in the hydrogen retention behavior [139, 140, 141]. The reason is that the C fluence determines whether the subsequent D will interact with a C-W mixed layer or a pure C layer, while the D fluence determines to what extent the C is eroded such that D no longer interacts with a C-W layer but rather pure tungsten. It should be noted that there is also a C and D energy dependence to the trapping behavior, since this determines the ranges as well as the creation of active C sites. For cases where the incident D interacts with a C layer, higher D retention is observed at low D fluences and approaches retention fractions in pure W with increasing D fluence [140]. For cases where incident D interacts with a C-W mixed layer, a decrease in D retention has been observed by Poon et al. [140], while an increase was observed by Ogorodnikova et al. [139]. The discrepancy remains as yet unresolved, but the results of Ogorodnikova et al. [139] are consistent with the hydrogen retention behavior in tungsten carbides. TDS spectra indicate that most of the D is released at $T \leq 800\,K$ [139, 141].

In summary, hydrogen retention in C-W mixed material is more similar to the retention behavior in pure W than C (i.e. significant diffusion into the bulk material). However, due to the presence of additional C traps an increase in retention in the implantation range is always observed. The observed effect is most pronounced at *RT* but decreases with increasing temperature, and the total retention amount approaches the retention behavior of pure W.

3 Experimental facilities

All experiments described in this study have been performed using the dual beam experiment (DBE) in the Tandem-Accelerator Laboratory in the Plasma Wand Wechselwirkung Group at the Max Planck Institut für Plasmaphysik in Garching, Germany. In the following sections the major components of the experimental apparatus used will be described together with an outline of the experimental techniques used. A detailed description of the apparatus is also given in Ref. [68], therefore only a concise overview is presented below. For details which are specific to an individual study, more information is provided in each respective chapters.

3.1 Dual beam ion accelerator

Irradiation was performed using the two independent ion sources of the dual beam experiment (DBE). A schematic of the DBE is shown in Fig. 3.1. It consists of two mass-selected ion beam lines focused on a single spot in the target chamber separated by an angle of 30°, resulting in an incident angle $\alpha = 15°$ during dual beam irradiation. The two independent sources allow a much wider study of the parameter range (the C fraction in the combined beams) than accessible in previous experiments [60, 62, 65]. In this thesis, different C fractions (f_c) in the total incident beam were obtained by keeping the C flux nearly constant (factor of 2) while the D flux was varied. The incident ion energies used for most experiments were $12\,keV$ C_2^- and $9\,keV$ D_3^+ ions. At these energies the incident ion species dissociate on impact resulting in energy/ion of $6\,keV$ for C and of $3\,keV$ for D. The DBE is also connected to a MeV tandem accelerator allowing *in-situ* ion beam analysis described in sections 3.3.3 and 3.3.4.

The "Quelle 1" (Q1) side is equipped with a standard Peabody Scientific Model PS-100 duoplasmatron source used to generate positive D ions. The source plasma is created within a cylindrical cavity by introducing high purity D gas from a Linde Minican controlled by a pressure regulator and controllable leak valve. A hot platinum filament is used as cathode and an axial magnetic field constricts the plasma, which is extracted through a $0.3\,mm$ diameter pinhole aperture by the applied extraction voltage (i.e. the implantation energy). The D ions are then focused using an einzel lens and X-Y steering plates before entering the 60° bending magnet for mass selection.

Ion energy:	$3000\,eV$
Filament current:	$14\,A$
Plasma arc current:	$1.2\,A$
Plasma arc voltage:	$90\,V$
Duoplasmatron magnet current:	$1.1\,A$
Extraction voltage:	$9\,kV$
Einzel lens voltage:	$8.2\,V$
Bending magnet current:	$12.08\,A$
Pressure:	$1.2 \times 10^{-6}\,mbar$

Table 3.1: Sample operating settings for Q1 source.

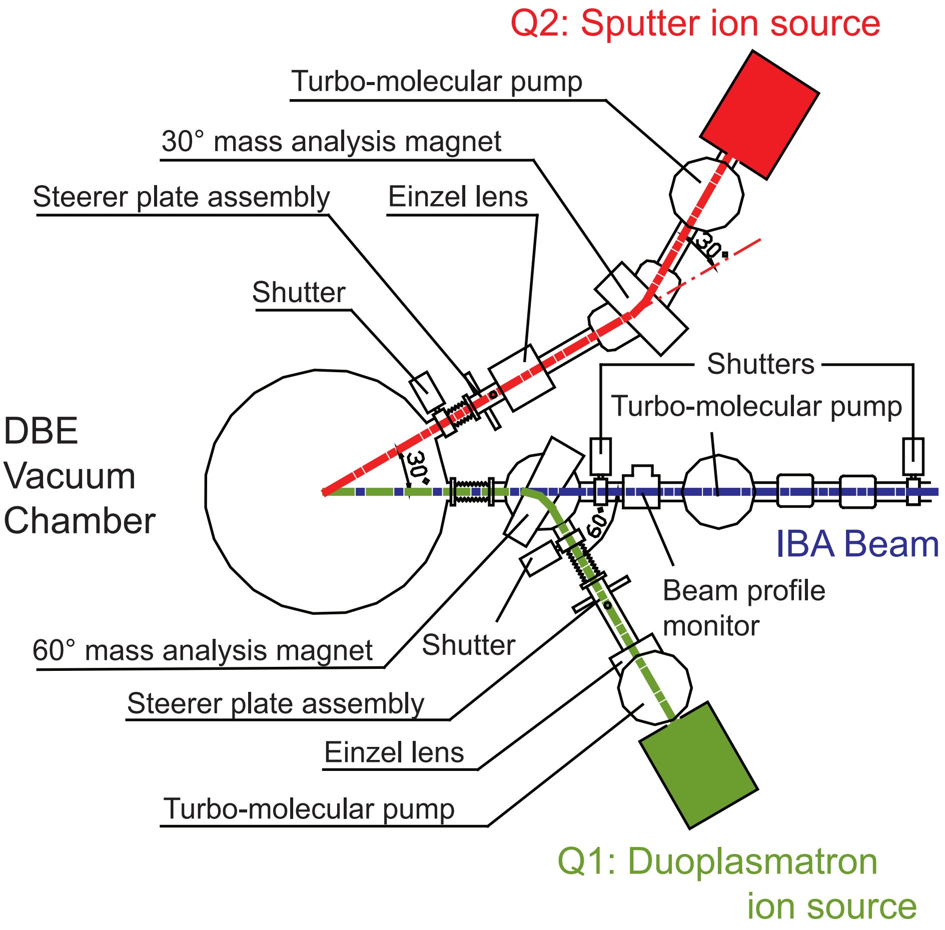
Q2: Sputter ion source
Turbo-molecular pump
30° mass analysis magnet
Steerer plate assembly
Einzel lens
Shutter
30°
Shutters
Turbo-molecular pump
DBE Vacuum Chamber
30°
60°
IBA Beam
Beam profile monitor
60° mass analysis magnet
Shutter
Steerer plate assembly
Einzel lens
Turbo-molecular pump
Q1: Duoplasmatron ion source

Figure 3.1: Schematic of Dual Beam Experiment (DBE).

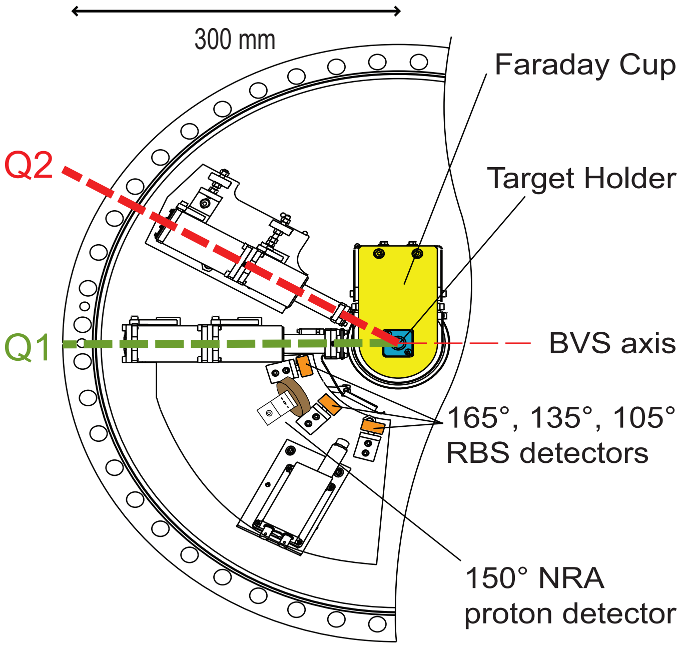
300 mm
Faraday Cup
Q2
Target Holder
Q1
BVS axis
165°, 135°, 105° RBS detectors
150° NRA proton detector

Figure 3.2: Schematic of the target chamber flange of the Dual Beam Experiment.

Ion energy:	$6000\,eV$
Tube heater current:	$53\,A$
Tube heater voltage:	$0.55\,V$
Cs reservoir current:	$0.6\,A$
Ionizer current:	$21\,A$
Extraction voltage:	$12\,kV$
Einzel lens voltage:	$-6.53\,V$
Bending magnet current:	$27.8\,A$
Pressure:	$1 \times 10^{-6}\,mbar$

Table 3.2: Sample operating settings for Q2 source.

The ions enter the DBE target chamber through a beam tube consisting of three apertures with a final beam aperture of $3\,mm$ diameter. The target is placed in a Faraday cup assembly at a distance of $15\,mm$ from the final beam aperture so that the beam divergence is considered negligible in between; see Fig. 3.2. A sample listing of the Q1 control settings used is found in Table 3.1.

The "Quelle 2" (Q2) side is equipped with a Peabody Scientific Model 120 negative ion sputter source used to generate negative carbon ions. A Cesium (Cs) reservoir is heated to produce Cs vapor that is positively ionized by an ohmically heated helical ionizer. The Cs^+ ions are accelerated onto the target cathode holding a cylindrical copper target with a graphite inset, sputtering the C atoms. The C atoms charge exchange in the neutral Cesium surface layer resulting in negative C ions which are repelled from the cathode and accelerated to ground potential. Therefore, the Cs^+ acceleration voltage is also the extraction voltage, limiting the achievable carbon current using this setup. The negative C ions are mass selected by a 30° bending magnet and focused using an einzel lens and X-Y steering plates before entering the target chamber through a separate beam tube. The final aperture is also $3\,mm$ in diameter with the distance to the target equal to Q1 at $15\,mm$. A sample listing of the Q2 control settings used is found in Table 3.2.

3.2 Dual beam target chamber

The target chamber is $700\,mm$ in diameter with a removable flange mounted on which the target holder assembly, beam guiding systems, and the detector assembly are mounted (see Fig. 3.2). Upgrades to the target chamber during this study include the installation of a Helix On-Board In-Situ Waterpump capable of water pumping speed of 35 000 ι/s, a Hiden HAL 201-RC single quadrupole residual gas analyzer, and a beam viewing system described in more detail in section 3.3.5.

The target holder assembly can be rotated and moved vertically by a two-axis motorized manipulator housed in a Faraday cup. It consists of a base plate consisting of: (1) the beam viewing system, (2) a calibration target holder for ion beam analysis, (3) two target holders, and (4) two boron-nitride ceramic heaters (see Fig. 3.3). The details of each component will be described in further detail in section 3.3.

The detector system consists of four planar silicon (PIPS) detectors mounted on

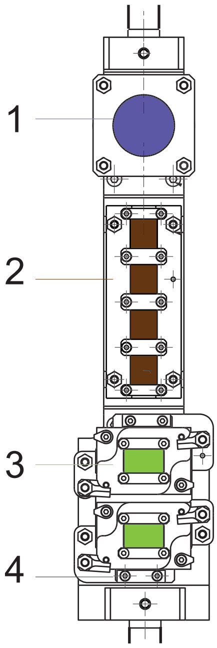

Figure 3.3: Schematic of target holder assembly showing: (1) beam viewing system (BVS), (2) calibration targets, (3) target holder, and (4) target heaters.

a common base plate at scattering angles of 165°, 135°, and 105° for the detection of backscattered ^{3}He$^+$ ions and at 150° for the detection of protons from nuclear reactions. A $5\,\mu m$ thick Ni foil is placed in front of the the large solid angle ($61.64\,msr$) 150° detector to allow only the transmission of the high energy protons. In addition, an X-ray detector is available for proton-induced X-ray analysis (PIXE), but was not used in this work. The entire assembly is shielded by a shutter that is remotely controlled to protect the detectors from the reflected ions during the irradiation stage of the experiments.

3.3 Experimental technique

The general procedure of the experiments is a series of irradiation steps of thin film specimens prepared by magnetron sputtering at a fixed C fraction in the incident flux and specimen temperature. The specimen preparation and characterization is discussed in sections 3.3.1 and 3.3.2, respectively. Following each irradiation step, in-situ ion beam analysis using ^{3}He$^+$ ions is performed with the heaters off. This method allows to study the dynamics of C and W sputtering, C implantation, and D retention as function of incident fluence species. Rutherford backscattering spectrometry (RBS) is used to quantify W sputtering behavior and will be discussed in section 3.3.3, while Nuclear reaction analysis (NRA) is used to determine the C and D areal densities and will be discussed in section 3.3.4. The C fraction in the incident flux and incident fluence of each species are determined by the beam viewing system calibrated against measurements of the total implanted current and will be discussed in section 3.3.5. The temperature measurement is performed using a pyrometer calibrated against thermocouple measurements and will be discussed in section 3.3.7. The main advantage of using in-situ ion beam analysis over previous weight-loss measurements is the capability of independent and accurate quantification of W sputtering and C implantation/re-sputtering, which provides in turn the ability to detect accurately the transition point between W sputtering and C deposition dominated regimes.

3.3.1 Specimen preparation by magnetron sputtering

Tungsten or carbon thin film specimens were prepared by sputtering of a carbon or tungsten cathode in a magnetron sputter device under vacuum using Ar as the working gas (see Fig. 3.4(a)). The device consists of three sputter cathodes (two shown) that can be shielded from the Ar plasma by movable shutters, and a rotating base plate on which the substrates are placed. A direct current (DC) or radio frequency (RF) plasma discharge sputters the cathode target material, mainly as neutral atoms, which are subsequently deposited on the substrates below. The magnetic field lines from the permanent magnets (see Fig. 3.4(b)) trap the secondary electrons in helical paths, resulting in increased ionization of the Ar gas and a corresponding increase in the target sputtering rate. The sputtered atoms, as mentioned earlier are neutrally charged, and so are unaffected by the magnetic trap. The properties of the deposited W films depend mainly on the Ar pressure, deposition temperature, and substrate bias voltage [146, 147]. At the low Ar pressure used, the arriving Ar neutrals reflected from the W cathode have sufficient kinetic energy to cause local lattice damage, promoting a dense microstructure. This effect of "peening" decreases with Ar pressure due to the enhanced collisional scattering of the neutrals with the plasma. Sputter-deposited refractory-metal films like tungsten tend to have high residual stress, which changes from compressive to tensile on increasing the working gas pressure [148]. Although, film stress plays an important role in determining the electrical and mechanical properties of the film, there is no known effect on surface binding energies which critically determine the sputtering yields.

The procedure for thin film preparation used in this study closely follow the procedures developed for the C-Wu-Si specimens used in a previous study [95]. However, W layers deposited on Si substrates were found to delaminate at high temperatures making them unsuitable as substrate material in this work. In addition, the Cu interface used previously acted as a D diffusion barrier during RT measurements, causing the D trapped at the interface to create blisters [95]. Therefore polished Ni substrates were chosen for W layer depositions with the thickness range of $400 - 500\,nm$. A DC discharge at $560\,V$ with Ar flow rate of 20 cubic centimeters per minute (ccm) was used for all specimens. Base pressures of $\approx 10^{-7}\,mbar$ were reached by using a liquid nitrogen cooling trap, and the introduction of Ar led to deposition pressures of $\approx 3.5\times10^{-3}\,mbar$. During deposition, the base plate temperature measured was $\approx 450\,K$, which was taken to be the Ni substrate temperature since the system reached thermal equilibrium. For C self-sputtering measurements (section 4.2.2) $\approx 250\,nm$ thick C films were deposited on polished ITER grade W substrates using an RF discharge of $500\,W$ at $20\,ccm$ Ar pressure. The temperature of the base holder stayed below $350\,K$.

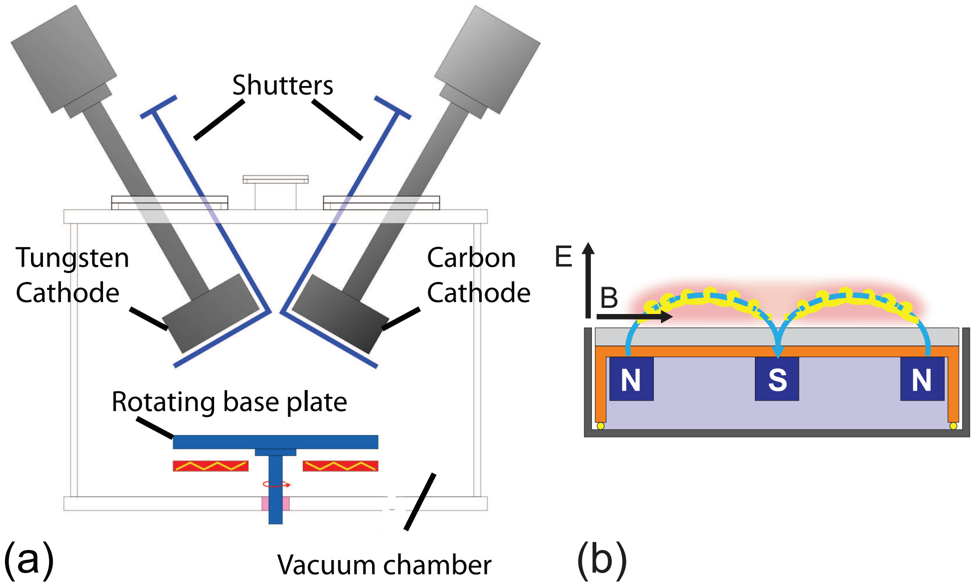

Figure 3.4: Schematic of the (a) magnetron sputter device, and (b) the cross section of a planar magnetron, where the electrons are trapped in cyclic motion near the target surface, leading to a higher plasma density and corresponding increase in cathode sputtering.

3.3.2 Specimen characterization

The impurity content of the tungsten (W) specimens were characterized by X-ray photoelectron spectroscopy (XPS), yielding oxygen (O) and carbon (C) concentrations < 2 %. No XPS characterization was performed for the C film specimens. RBS was used to determine the W film thickness by measuring the W areal density and will be discussed in section 3.3.3, while NRA was used to determine the C areal density and will be discussed in section 3.3.4. For both carbon and tungsten film specimens, atomic force microscopy (AFM) was used to study the surface topography and roughness while scanning electron microscopy (SEM) was used to analyze the surface morphology. X-ray diffraction (XRD) measurements were performed to characterize the deposited C and W film structures.

Atomic force microscope

The atomic force microscope is a class of scanning probe microscope where a probe consisting of a sharp tip at the end of a cantilever is rastered across the specimen surface in either contact or tapping mode measuring the topographic image of the specimen surface in three dimensions (where z is normal to the specimen surface). All measurements were performed in contact mode, where a constant force is maintained on the cantilever which pushes the probe tip against the specimen as it rasters the surface. This deflection is kept constant by maintaining constant tip-specimen separation by moving the scanner in the z direction by a feedback loop. A typical scan area measuring $L_x \times L_y$ is collected with the data represented as a discrete two-dimensional data field of size $N \times M$, with nominally an equal sampling interval distance, $\triangle$.

AFM measurements were performed using a Rasterscope 4000, AFM 2194, DME in

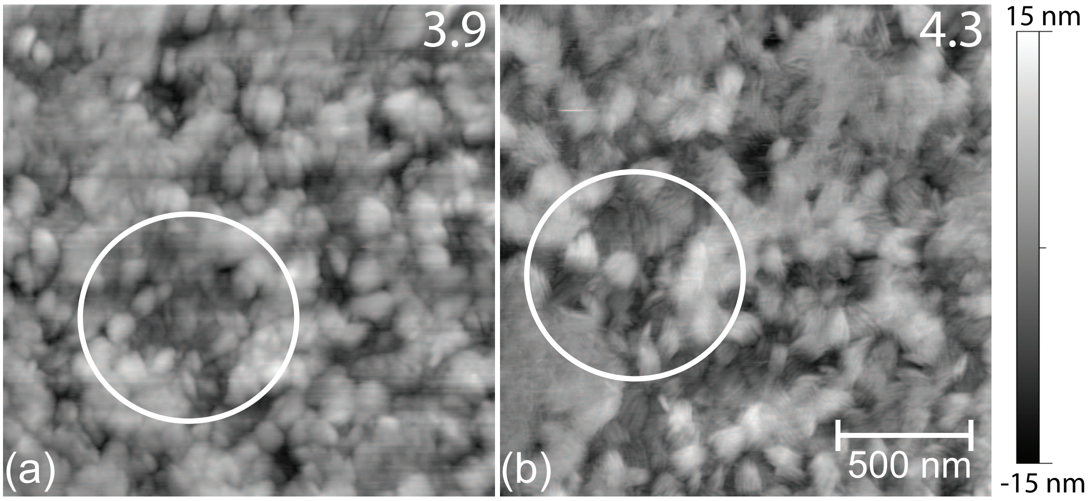

Figure 3.5: Atomic force microscope (AFM) images of deposited W-film specimens using an (a) old tip and (b) virgin tip. The numbers indicate the root mean square (RMS) roughness value, R_q in nm.

contact mode at $0.5\,nN$ using pyramidal Si tips (radius of curvature $< 10\,nm$) at a scan speed of 3 $\mu m/s$. A nominal scan area of $2\,\mu m \times 2\,\mu m$ consisting of 512×512 pixels was collected. Surface roughness was quantified by using the open-source software Gwyddion [149] to determine the root mean square roughness (R_q) of the scanned area. This parameter is an amplitude parameter and measures the standard deviation of the distribution of surface heights with the following definition [150]:

$$R_q = \sqrt{\frac{1}{n}\sum_{j=1}^{n} y_j^2}$$

where y_j is the height deviation from a mean line defined as a line from which the sum of the squares of the height deviations is equal to zero, and n is the number of sampling lengths. Tip sharpness critically determines the resolution of the collected images and corresponding R_q values, since prolonged use will tend to broaden out the tip radius [151]. Therefore, to estimate the magnitude of tip wear on measured roughness, a calibration experiment on deposited W film specimen was performed using an old and virgin tip on the same specimen location (see Fig. 3.5). As seen by comparing the circled areas in Figs. 3.5(a) and (b), the virgin tip is able to resolve small surface features ("platelets") that were previously not visible using the old tip. Also, due to the increase in resolution, the R_q value increases by $\approx 0.5\,nm$ using the virgin tip. The magnitude of this error from tip wear is comparable to the statistical variation of R_q values measured at several different specimen locations. Therefore, as an upper estimate, the error in the R_q value was taken to be $\pm 1\,nm$ throughout this work unless otherwise stated.

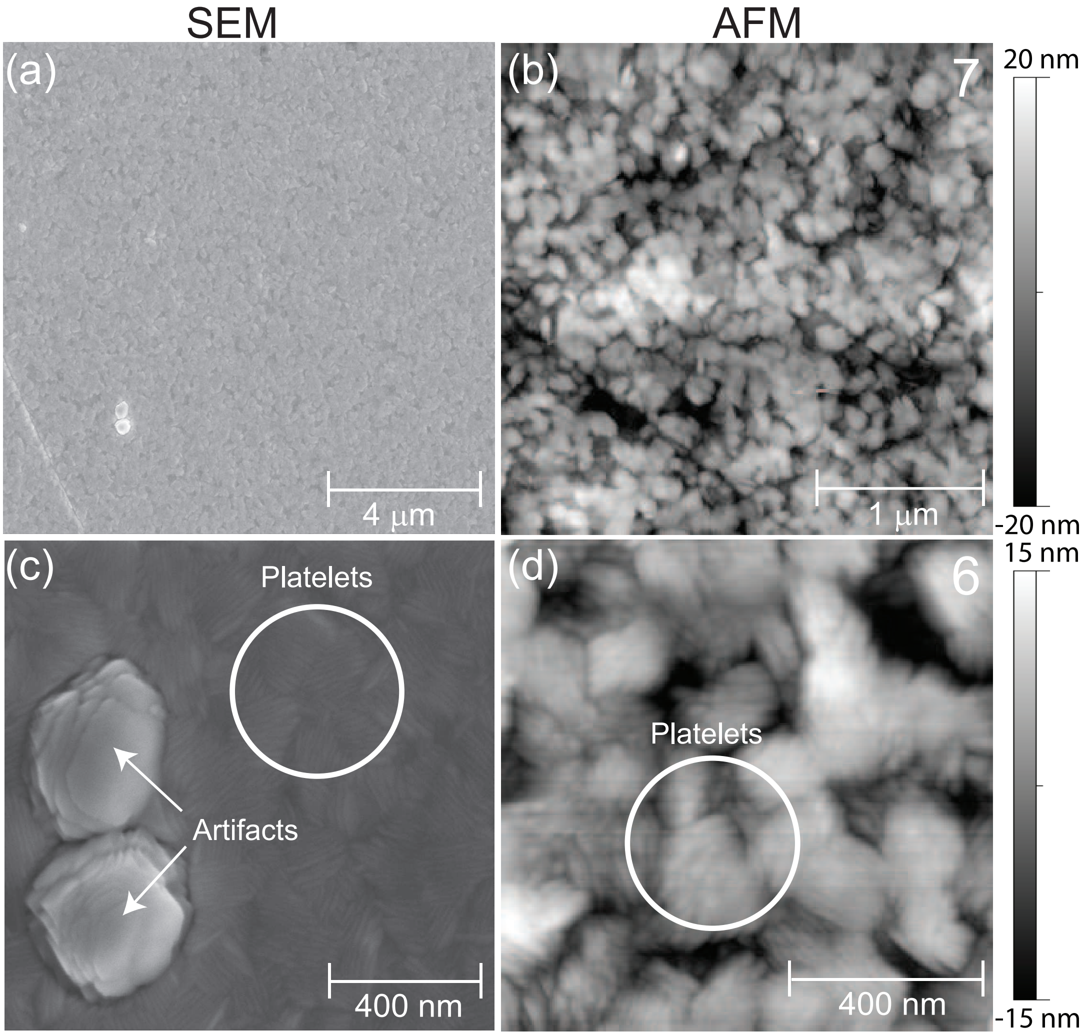

Figure 3.6: Comparison of the as-deposited W film surface from (a,c) SEM and (b,d) AFM measurements for two different scanned areas.

Scanning electron microscope

Scanning electron microscopy was used to study the surface morphology by collecting both the secondary electrons which are sensitive to surface structures, and the backscattered electrons which are sensitive to elemental composition. Two scanning electron microscopes, an XL 30 ESEM from FEI operated at $20\,kV$, and a higher resolution Helios nanolab 600 from FEI operated at $10\,kV$ was used. As seen from Fig. 3.6(a), the W-film specimen is in general laterally uniform with a few isolated surface artifacts and scratches visible. By analyzing the backscattered electrons, the round artifacts were determined to be tungsten and not surface contaminants. These artifacts are few however, and the surface generally represents a patchwork of "platelets" (circled) as seen from the higher magnification in Fig. 3.6(c) or from the corresponding AFM image in Fig. 3.6(d). In general, good agreement between the surface morphology is observed between AFM and SEM images as seen by comparing Figs. 3.6(a-b) or (c-d).

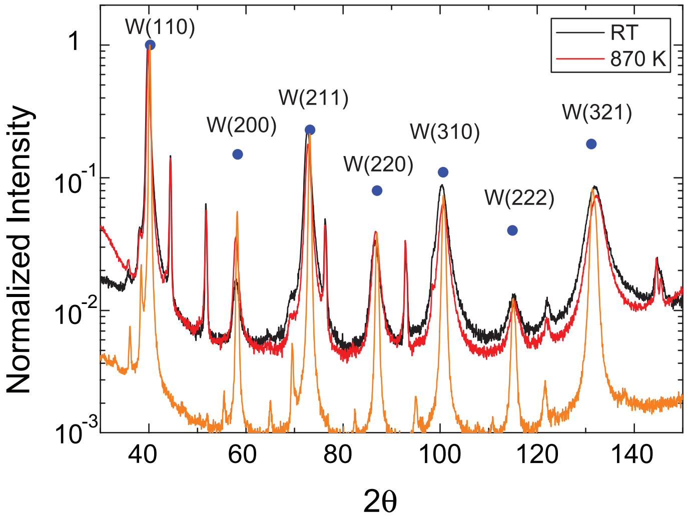

Figure 3.7: X-ray diffractograms obtained using the gracing incidence geometry of a virgin as-deposited W specimen (black) and a specimen annealed at 870 K for 4 h (red). Also shown for comparison is the spectrum from ITER grade bulk W (orange). Each spectrum is normalized to its respective maximum intensity observed at the W(110) peak. The positions of the W peaks are taken from JCPDS database PDF 04-0806 [152] with the relative intensities corresponding to body-centered-cubic (bcc) α-W phase indicated by the blue points; the unlabeled peaks in the W-film spectra correspond to the Ni substrate.

2θ	hkl	PCW [152]	RT	$770K$	$870K$
39.8	110	1	1	1	1
58.0	200	0.15	0.02	0.03	0.04
72.7	211	0.23	0.23	0.21	0.18
86.7	220	0.08	0.03	0.03	0.04
100.5	310	0.11	0.09	0.07	0.07
115.1	222	0.04	0.01	0.01	0.01
131.7	321	0.18	0.08	0.07	0.07

Table 3.3: The relative peak intensities observed for detector angle 2θ, for as-deposited specimen compared to annealed specimens at 770 K and 870 K. Reference data from [152] is also listed.

X-ray Diffraction

A diffractogram obtained by gracing incidence X-ray diffraction (XRD) analysis, where the incident beam was kept constant at $\alpha = 3°$ while the detector geometry was varied, is shown in Fig. 3.7 for a virgin as-deposited W specimen and a specimen annealed at $870\,K$ for $4\,h$. Also shown for comparison is the spectrum from an ITER grade bulk tungsten specimen. This geometry was chosen to maximize the X ray penetration along the thin film and reduce the contribution of the Ni substrate since the deposited W films are on the order of $400-500\,nm$, while the X rays probe depths in the $10-100\,\mu m$ range. The diffracto-meter was a model Seifert XRD 3003 PTS operated with CuK$_\alpha$ radiation ($0.154\,nm$). Comparison of the W peaks to XRD reference data [152] in Fig. 3.7 show good agreement, indicating that the W film is primarily a body-centered-cubic (bcc) α-W phase, similar to randomly oriented polycrystalline tungsten (PCW) foils or bulk W samples used in sputtering and retention studies. The ratio of the (211)/(110) peaks is in good agreement to that of PCW as seen in Table 3.3. However, it is quantitatively difficult to relate the intensity of each peaks to a corresponding amount in the W film and the quantitative determination of a dominant crystallographic phase can therefore not be made from Fig. 3.7. However, the tungsten films indicate a strong <110> texture or preferred orientation parallel to the surface normal.

The width of the peaks are rather broad in comparison to ITER grade PCW, which is due to several factors like small crystallite sizes, the crystallite shape and distribution, and distortions in the crystal structure from stacking faults, dislocations, and microstrain [153]. The evaluation of the peak broadening to extract quantitative information on crystallite size and lattice strain was not performed since under ion irradiation the original structures lose their importance with increasing fluence due to ion-induced damage of the material. A comparison to $150\,nm$ W films deposited under similar DC magnetron sputtering conditions at $3\,mTorr$ Ar pressure show similar XRD patterns with strong <110> texture and compressive stress [147]. Transmission electron micrographs (TEM) of the W film cross section showed a dense microstructure without any columnar structures with no evidence of voids [147]. Comparison to $500\,nm$ thick W films deposited via simultaneous W evaporation and Ar bombardment [146] also display the "platelet" surface appearances seen in Fig. 3.6 with <110> texture. Therefore, the W films prepared in this work are similar to W films deposited using other magnetron sputtering devices, but more importantly, is comparable in structure to the PCW foils and bulk W samples used commonly in sputtering and retention studies in the published literature data. No clear peaks were observed for the C film specimens (amorphous) and therefore its diffractogram was not included.

Effect of Tungsten specimen annealing

From the XRD diffractogram (see Fig. 3.7), annealing the specimen at $870\,K$ for $4\,h$ results in minor changes in the relative peak intensities with only the (211)/(110) ratio showing an observable decrease (see Table 3.3). This decrease has been observed to correspond to decreasing film stress [154] which will affect the D trapping behavior, as stress-relieved W is observed to retain reduced amounts of D retention [155]. In addition, from Fig. 3.8, it can be seen that the temperature induced structural or-

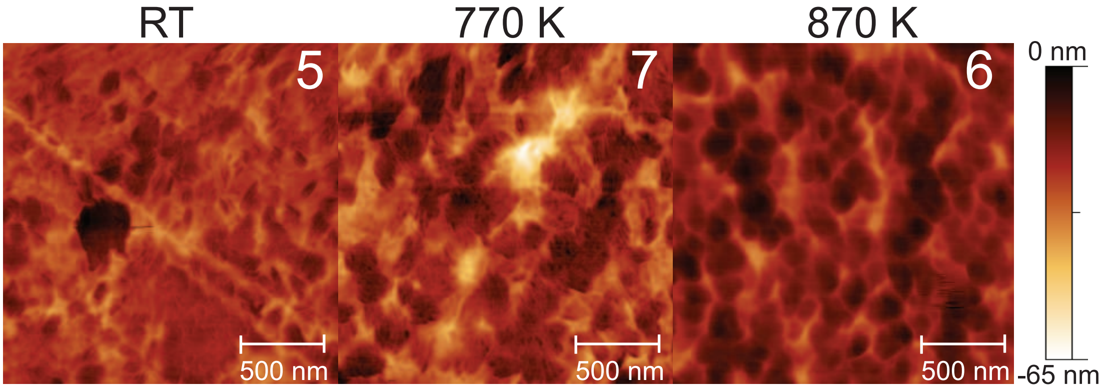

Figure 3.8: Comparison of AFM images of as-deposited W specimens with annealed specimens at 770 K and 870 K for 4 h.

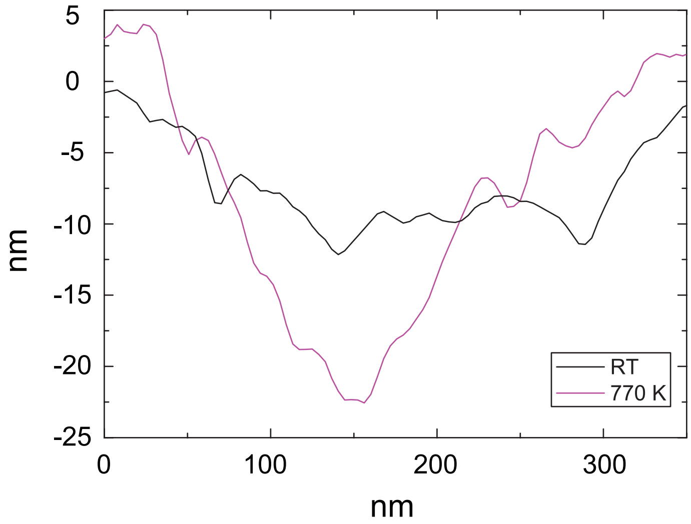

Figure 3.9: Comparison of sample AFM surface elevation of as-deposited W specimen with specimen annealed at 770 K for 4 h in the region where the different orientation of the platelets meet in Fig. 3.8.

dering results in a increase in surface roughness from RT to 770 K, but retain the overall “platelet” appearance at the surface. The increased roughness results primarily from the increased peak to peak variations as shown in Fig. 3.9 in the regions where nanocrystallite groups of different orientation meet. The “platelet” structures which can no longer be distinguished in the AFM images for specimens annealed at 870 K and corresponding decrease in R_q value is attributed to tip wear. Therefore, annealing to 870 K does not result in significant changes to the W film structure aside from reduction in film stress accompanied by an increase in surface roughness. The W film specimens can therefore be assumed to be stable during irradiation experiments at elevated temperatures.

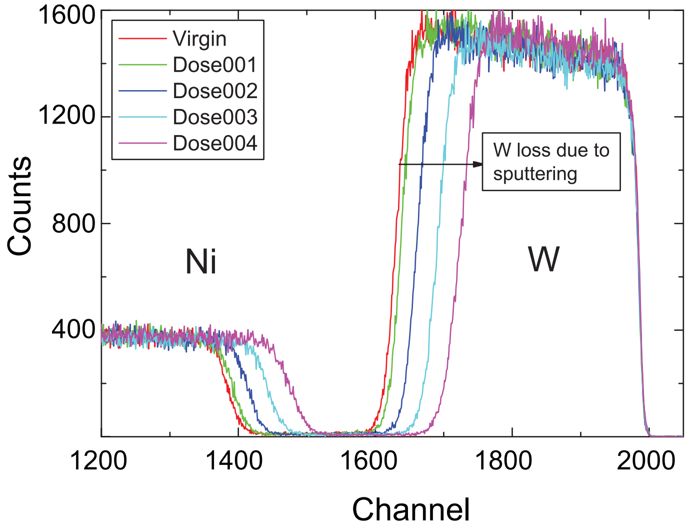

Figure 3.10: Typical RBS spectrum collected between each irradiation step showing the decrease in the width of the tungsten peak as a result of sputtering.

3.3.3 Rutherford backscattering spectrometry

Rutherford back-scattering spectrometry is the standard ion beam analysis technique used to accurately determine the stoichiometry, elemental areal density, and impurity depth distributions in thin films. A mono-energetic MeV ion beam ($2.5\,MeV$ $^3\mathrm{He}^+$ ions in this study) scatters elastically due to collisions with the target atoms with energy characteristic of the mass of the struck particle at given scattering angle. The ratio of incident to final energy ($\frac{E_1}{E_o}$) is only dependent on the masses of the incident projectile, target particle (M_1, M_2), as well as the scattering angle θ:

$$\frac{E_1}{E_o} = \left[\frac{(M_2^2 - M_1^2 sin^2\theta)^{\frac{1}{2}} + M_1 cos\theta}{M_1 + M_2}\right]^2$$

By measuring the number of backscattered ions as well as their energy using a solid state detector at a defined scattering angle θ, the unknown target mass, M_2 can be determined. For a full description of the technique see Refs. [156, 157]. Further details with a detailed discussion regarding the advantages of the RBS technique for the study of W sputtering and C layer formation can also be found in Ref. [68].

A collection of RBS spectra for a W-Ni specimen collected in between subsequent irradiation steps with a 165° detector ($3.28\,msr$) is shown in Fig. 3.10. The loss of W results in the decrease of the W peak width and a corresponding increase of the energy related to the W-Ni interface. The total amount of W sputtered can be determined by taking the difference in the measured W areal density following each irradiation step against the virgin specimen. To determine the W areal density, the spectra are fitted by the SIMNRA [158] program. Assuming PCW like W density of $19.3\,g/cm^3$ results in typical W film thicknesses of $400-500\,nm$ with thicknesses varying depending on the specimen location in the base plate during deposition.

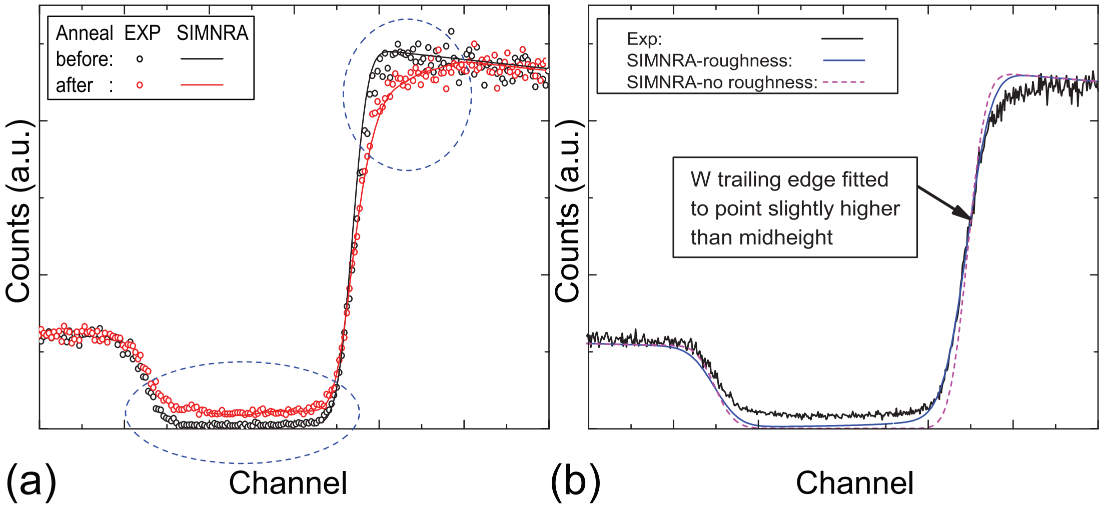

Figure 3.11: RBS spectrum showing: (a) the effect of W-Ni interface mixing resulting in decrease of W peak at the trailing edge, and (b) the effect of surface roughness on the trailing edge of the W peak.

The W-Ni interface remains stable at annealing temperatures below $870\,K$. But at $870\,K$, the heating process during irradiation results in W diffusion into the Ni substrate and corresponding mixing of the W-Ni interface. The RBS spectra before and after annealing at $870\,K$ for $4\,h$ are seen in Fig. 3.11(a), with their corresponding SIMNRA fits. The effect of the W-Ni interface mixing results in a decrease of the W peak height at the trailing edge of the spectrum and a corresponding increase in counts between the W and Ni peaks (circled blue), due to dilution of W at the interface region. The loss in W counts from the trailing edge is accounted for the gain in W counts between the W and Ni peaks, and the difference in the W areal density from the two SIMNRA fits before and after annealing is within 1%. The mixing does not result in any significant loss of W into the Ni bulk or result in Ni diffusion to the W surface. Therefore, the time consuming fitting of the mixing was neglected and the W spectra were fitted to optimally match the W trailing edge only. Furthermore in some cases, irradiation at $T < 870\,K$ leads to the increase in W surface roughness from the sputtering process or from the growth of a rough overlying C layer, leading to the observed decrease in the slope of the trailing edge as seen in Fig. 3.11(b). For these cases, the trailing edge was fitted to a point slightly higher than the mid height of the trailing edge and surface roughness effects were not included in SIMNRA simulations. This approximation resulted in an uncertainty below 10% in determining the W areal density.

3.3.4 Nuclear reaction analysis

The Rutherford cross section or scattering probability increases with the square of the atomic number [156]. Therefore, scattering events from light elements like carbon (C) in a heavy tungsten (W) matrix will be detected against a large background signal making it almost impossible to discern its contribution. Furthermore, deuterium cannot be measured using RBS, and thus, the C and D areal densities were determined using the

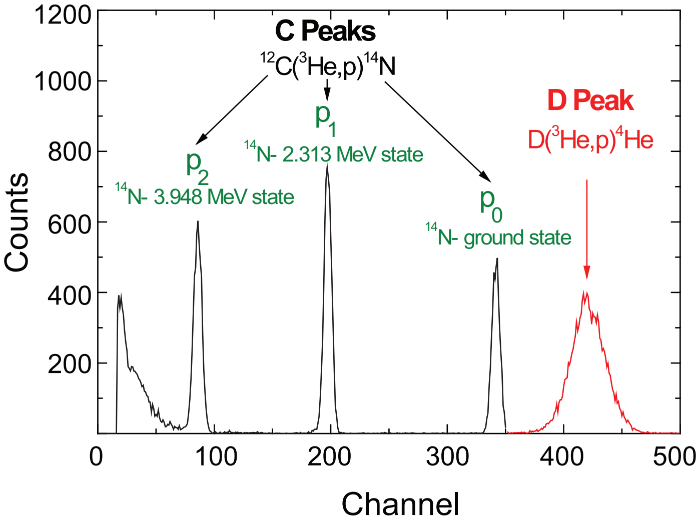

Figure 3.12: NRA spectrum of a hard a-C:D calibration target showing the four proton peaks from the D(^{3}He, p)^{4}He and ^{12}C(^{3}He, p)^{14}N nuclear reactions. The C-related peaks of p_0, p_1, and p_2 correspond to protons from reactions with ^{14}N in ground state, 2.313 MeV excited state, and 3.948 MeV excited state [159], respectively.

nuclear reactions ^{12}C(^{3}He, p)^{14}N and D(^{3}He, p)^{4}He, respectively [159]. These nuclear reactions are isotope specific with no direct relationship between the mass of the target nucleus and the energy of the detected particles. The protons were collected using a solid angle (61.64 msr) detector with a 5 μm Ni foil placed in front of the detector to filter out the backscattered ^{3}He ions. A typical spectrum of the collected protons is shown in Fig. 3.12. The ^{3}He nuclear reaction with carbon leads to three peaks in the spectrum because the ^{14}N produced in the reaction can be created in an excited state with correspondingly less energy left for the proton. The peaks p_0, p_1, and p_2 correspond to protons from reactions with ^{14}N in ground state, 2.313 MeV excited state, and 3.948 MeV excited state [159], respectively. The broadened peak centered around channel 420 is due to protons from the ^{3}He reaction with deuterium. The broadening in comparison with the carbon-related peaks results from the higher energy of the protons. Because the thickness of the active detector layer is not sufficient to stop the protons entirely, they lose only a fraction of their energy on their path through the detector layer, which leads to a broader distribution of the deposited energy by the corresponding energy loss straggling. By integration of the C- and D- related proton peaks and by multiplication with the respective calibration factors determined from a reference hard a-C:D layer on Si, the corresponding total C and D areal densities can be determined with an error $<$10%.

The accurate measurement of the integrated beam dose (nominally 5 μC) is of critical importance in obtaining good accuracy for both RBS and NRA. Unfortunately, the heating of the sample holder results in many different metals to heat up and the Seebeck effect results in random positive or negative offset currents (maximum few nAs) to be present during ion beam analysis. Therefore, a negative offset will result in a collected dose $> 5\,\mu C$, while a positive offset will result in a collected dose $< 5\,\mu C$.

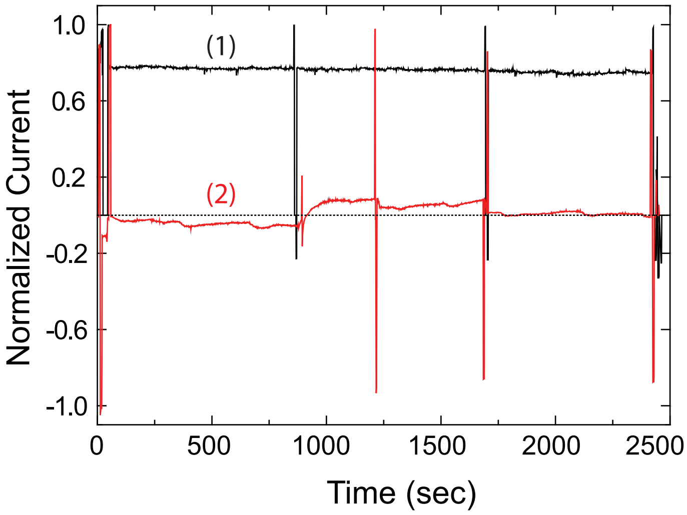

Figure 3.13: Normalized current measurements of: (1) steady C and D beams resulting in near constant total current during one irradiation step, and (2) unsteady C beam resulting in fluctuations in the total current measurement. Curve (1) has been offset from zero to better distinguish the two curves.

To overcome this problem, prior to heating, an RBS spectrum of the virgin specimen was collected up to a total dose of $5\,\mu C$. The SIMNRA fit of the spectrum will result in the true particles*sr value that corresponds to this nominal dose of $5\,\mu C$. Variation of the particles*sr value from this true value therefore yields the variation of the collected dose when the RBS spectra collected for the heated specimens are fitted. It is assumed that the detector solid angle does not change during experiments because the thickness of the specimens will vary only on a nm scale.

The channels corresponding to the energetic MeV protons from the D reactions were observed to shift to lower energies with increased heating time of the system. This is most likely due to the heating and corresponding expansion of the Ni foil in front of the solid state detector. The increased thickness will result in increased electronic energy loss of the MeV protons, resulting in the observed shift to lower energies. This heating induced shift results in the proton peaks of C and D to become mixed, which could be resolved by fitting to sum of two overlapping Gaussians. The mixing of the C and D peaks was most pronounced for experiments at $870\,K$, but for these cases, the amount of D trapped in the material was normally below the detection limit and did not result in significant errors in the determination of the C areal density.

3.3.5 Beam viewing system and fluence measurements

The implanted current of the carbon (C) and deuterium (D) beams during irradiation was measured using a Model 6487 Keithley picoammeter with typical readings shown in Fig. 3.13. The positive and negative spikes correspond to measurements of the D and C beams respectively. The normalized total current measurements are shown for two different experiments where (1) corresponds to steady C and D beams during irradiation, while (2) corresponds to an unsteady C beam resulting in fluctuations in the total current measurement. Due to the larger C fluxes required to reach steady state conditions with increasing temperature, the previous approach of defocusing the beams to achieve homogeneous distribution of the beams resulted in unacceptable low fluxes. Therefore, the C beam was focused to produce the highest flux possible which resulted in an inhomogeneous distribution over the entire beam spot (see Fig. 3.14). For such an inhomogeneous beam, the method of determining the C and D fluences by averaging the total current measurements over the entire beam area result in large errors since the local C and D fluence in the area analyzed by the $^3\mathrm{He}^+$ ions is in general much higher than the averaged values. Therefore, in order to obtain quantitative and accurate measurements of the incident beam distributions, C fraction in the total flux (f_c), as well as locating the position of the analysis spot of the $^3\mathrm{He}^+$ ions relative to the beam spots of the low energy ion sources, a so called Beam viewing system (BVS) [160] was installed as new diagnostic tool. The device consists of a Photonis imaging quality microchannel plate (MCP) manufactured by Burle industries, and a phosphor screen coupled with a CCD camera that captures the light produced by the amplified charge pulses of the incident ions (see Fig. 3.15(a)). The imaging area of the MCP is $18\,mm$ in diameter and typically operated at $700\,V$ bias resulting in a gain of 200. The nominal pore size of the MCP is $10\,\mu m$ with a nominal center-to-center spacing of $12\,\mu m$. The phosphor screen is a standard aluminized P-20 deposited on glass plate with a conversion efficiency of $\eta = 0.063\,photons/eV/electron$ operated at $3000\,V$ bias. The camera system used is a 12 bit Pixelfly QE 270 system from PCO imaging, with a resolution of 1390 × 1024 pixels, with a pixel size of $6.45\,\mu m \times 6.45\,\mu m$, capable of imaging a $9\,mm \times 6\,mm$ area. The camera can be operated with variable exposure times from $10\,\mu sec - 10\,sec$, but nominally an exposure time of $1\,sec$ was used. The camera is equipped with a telecentric CCD lens from Sill Optics (S5LPJ9032) to allow focusing of the beam image from outside the vacuum vessel without affecting the actual beam spot size. The resulting images are first collected using the software Camware, followed by analysis using programs implemented in the computer language IDL. The integral over the image intensity was calibrated against the current measurements of the picoammeter to obtain calibration factor relating the light intensity to charge. A short description of the calibration procedure follows next.

3.3.6 Calibration of BVS measurements

The collected intensity of the BVS images must be calibrated against the dose of incident ion charge to determine the lateral distribution of fluence and C fraction in the incident flux, f_c. Accurate determination of both quantities depends critically on the accurate measurement of: (i) the area of the beam, and (ii) the total dose amount. To determine (i) the area of the beam, the pixel size of the collected images must be translated to an actual geometric area. This was done by mounting a calibration plate with a $1\,mm$ diameter hole and integrating the pixel counts to obtain a calibration factor relating the pixel/area. The main source of error lies in defining the region of interest (ROI) of the beam boundary over which the intensity of the pixels are integrated and calibrated against the current measurement.

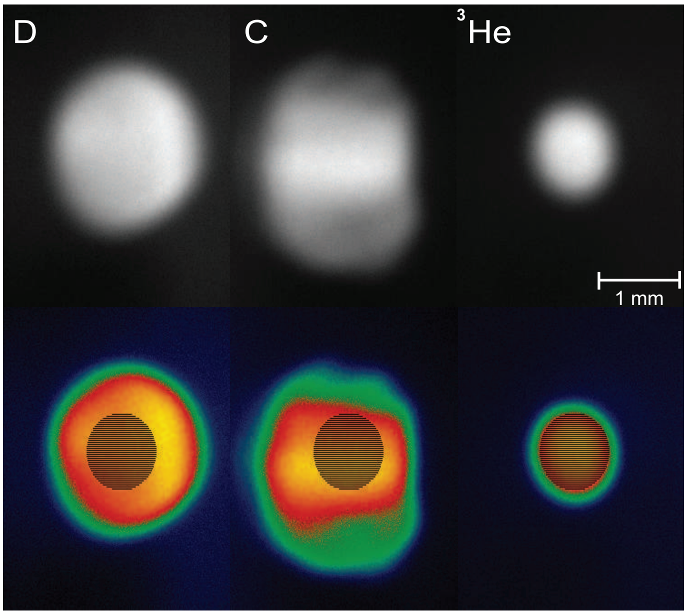

Figure 3.14: Images of the D and C beams, as well as the analysis $^3He^+$ beam measured using the BVS. The first row corresponds to the raw images captured by the CCD camera, while the second row shows a color mapping of the intensity variation mapped in the computer language IDL environment.

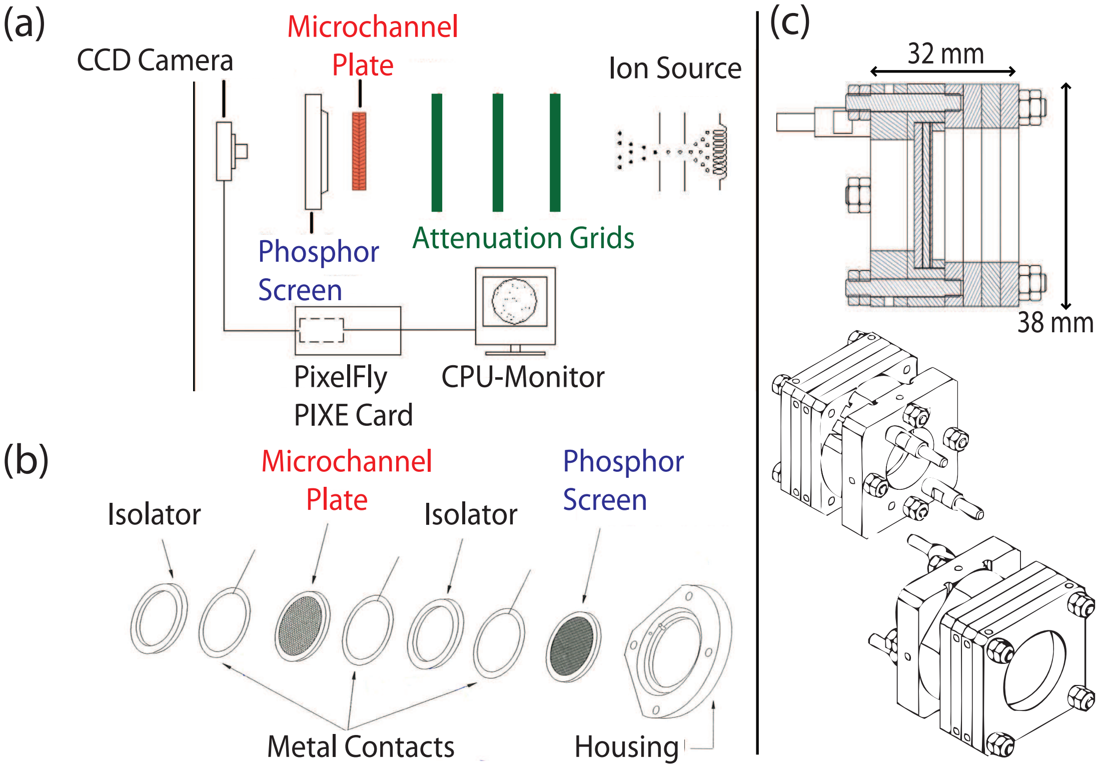
(a)
CCD Camera
Microchannel Plate
Ion Source
Phosphor Screen
Attenuation Grids
PixelFly PIXE Card
CPU-Monitor
(b)
Isolator
Microchannel Plate
Isolator
Phosphor Screen
Metal Contacts
Housing
(c)
32 mm
38 mm

Figure 3.15: Schematic diagram of: (a) the major components of the Beam viewing system, and (b) exploded view of the housing showing the stacking sequence of the microchannel plate (MCP) and phosphor screen. Also shown are the (c) technical drawings showing the major dimensions of the BVS and the mounting assembly.

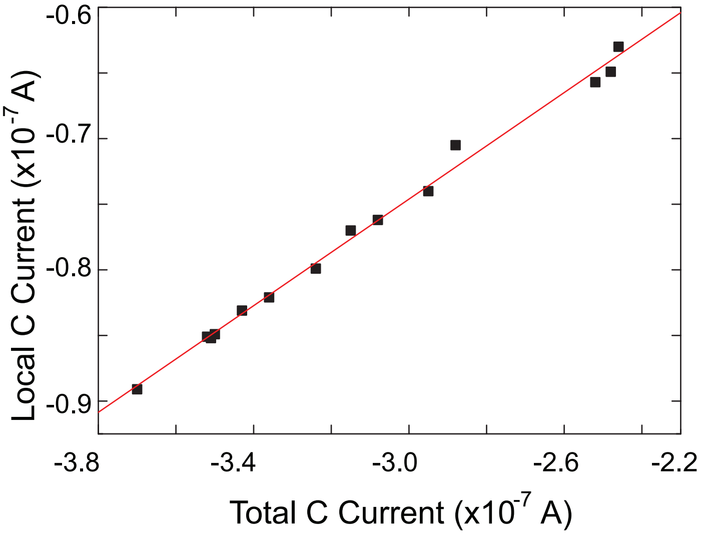

Figure 3.16: Calibration curve showing the linear dependency of the fluctuation of the local C current determined by the BVS against the total C current measured by the picoammeter.

The attenuation grids used to reduce the beam intensity introduce a scatter of the beam (<10 pixels) resulting in a beam boundary that is not sharply defined. Also, due to the principal of MCP operation, parasitic electrons may be produced which can misleadingly indicate a larger beam area. However, the errors associated from both effects is <5% and is often negligible compared to the error in determining (ii) the total dose amount. Normally, the BVS was used to collect the beam images at the start and end of each irradiation step and the total fluence was calculated by taking the average of the two measurements. Under normal ion source conditions, this method provides sufficient accuracy given the constant currents generated by the ion sources as seen from curve (1) in Fig. 3.13. However, when the C source operates unsteadily due to fluctuations of cathode erosion, the resulting current fluctuation as seen from curve (2) in Fig. 3.13 introduces large errors. It was determined however that the fluctuations in the total C current are approximately linearly dependent on the C current fluctuation in the local area of interest (see Fig. 3.16). Therefore, for experiments where the C beam fluctuations were large, the total C current component was isolated from the total current measured (D+C) by subtracting the normally constant D component. The resulting curve yields the total C current as a function of time, and using a calibration curve (see Fig. 3.16), the local C current as a function of time can be determined. In turn, by integrating this curve, the C fluence and the C/D ratio in the analysis area can then be more accurately determined. The difference in the C fluence amount can vary by up to 30% in some cases between the two methods of calculation. It should be noted that for experiments where f_c is large (i.e. the D flux is reduced), the fluctuation of the C beam introduces a correspondingly greater error in determining both the total fluence (C+D) and the C fraction in the incident flux, f_c. For these experiments, special care was taken to ensure that the sources operated with minimal disruptions.

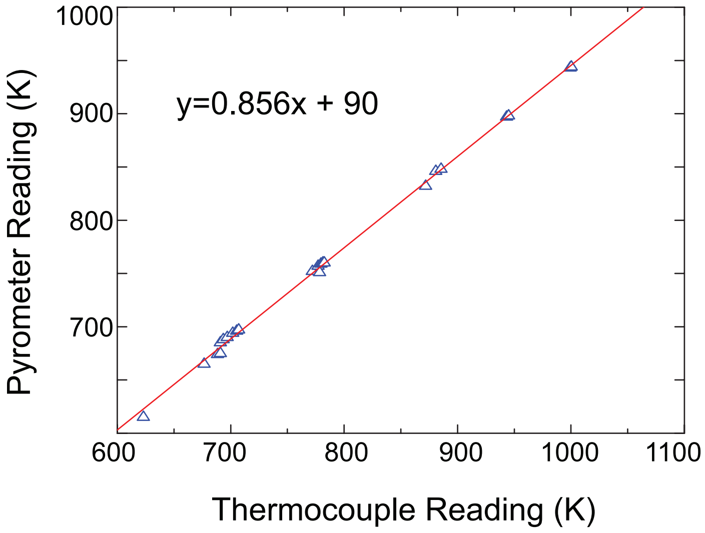

Figure 3.17: The pyrometer temperature readings calibrated against thermocouple measurements.

3.3.7 Temperature measurements

The specimens were heated using a standard Boralectric ceramic heater located behind the specimens to $670\,K$, $770\,K$, and $870\,K$ using a FUG power supply at $2.10\,A$, $2.80\,A$, and $3.75\,A$, respectively (Model NTN 700-65, $65\,V$, $10\,A$). The temperature was measured using a two wavelength pyrometer (Impac model IGAR 12-LO) which was calibrated using a chromel-alumel thermocouple attached to the front surface of the specimen. Direct temperature measurement of the irradiated W area is difficult due to the complicated emissivity dependency on the C concentration implanted during experiments. Therefore, the pyrometer spot was focused on the stainless steel target holding plate $\approx 3\,mm$ away from the center of the irradiated area, where a thermocouple was also installed. The calibration curve used for W-Ni specimens is shown in Fig. 3.17. The pyrometer readings were limited to temperatures $> 570\,K$ because of the decreasing signal-noise ratio towards lower temperatures.

4 Carbon-only irradiation

The use of carbon (C) as a plasma facing material in ITER will lead to the presence of C impurities in the plasma due to erosion of the material. At typical plasma edge temperatures ($10 - 100\,eV$) carbon ions occur mainly in higher ionization states. Multiply charged C ions incident at a wall surface will be accelerated in the sheath potential and can therefore impact with energies up to the lower keV region [49, 161]. The ASDEX-Upgrade tungsten divertor experiments have shown that W sputtering is dominated by such C impurities originating from erosion of graphite plasma facing materials in the main chamber [19]. Tungsten sputtering by C has been well characterized both by experiments and simulations primarily through comparison of weight-loss measurements performed at IPP with TRIDYN calculations [60, 61, 63, 65], resulting in the sputtering yields discussed previously in section 2.1.2. The experimental findings presented in this section are intended to characterize particularly the temperature dependence of the sputtering behavior of tungsten for $E_c = 6\,keV$ C ion irradiation in the temperature range $RT - 870\,K$ and to benchmark respective TRIDYN calculations.

The use of ion beam analysis leads to significant improvement over the previous weight-loss measurements because it allows to quantify the previously inaccessible parameter of the implanted C areal density, n_c. The W sputtering behavior will be shown to be fully parametrized by n_c, effectively reducing the problem of C implantation and W sputtering to one parameter. A fully characterized description of the W sputtering behavior by C is an important prerequisite for separating the effect of additional D bombardment during simultaneous irradiation and quantifying the correspondingly invoked synergistic effects.

Furthermore, the temperature dependence of the C self-sputtering yields was determined in the previously unexamined temperature range $670 - 870\,K$. The purpose of this set of experiments was to obtain the temperature dependence of C surface binding energies ($SBEs$) as input parameters for TRIDYN calculations. The benchmarked TRIDYN calculations will be used as fitting curves for the application of the phenomenological model described in section 6.

4.1 Specimen characterization

Tungsten was irradiated using $6\,keV$ C ions at $\alpha = 15°$ and surface temperatures of RT, $670\,K$, $770\,K$, and $870\,K$. At this angle of incidence, a C layer always forms following an initial period of W sputtering as discussed in section 2.1.2. In order to facilitate a better understanding of the experimental results presented in section 4.2, it is useful to view the development of the specimen's surface morphology as a function of irradiation fluence as the system moves from W erosion to C layer formation. AFM and SEM images will serve to illustrate the surface modification, while Raman spectroscopy will be used to characterize the structure of the developed C layer. XRD could not be applied for this purpose because the diameter of the irradiated area was much smaller than the area analyzed by the X-rays.

4.1.1 Surface roughness

The effect of surface morphology and its impact on sputtering behavior has been studied for fusion applications [71, 162, 163] as well as in plasma processing [164, 165]. In the context of ion-surface interactions, a surface is defined to be smooth if the mean ion range of the incident species, λ, is significantly greater than the surface roughness, R_q (i.e. $\lambda \gg R_q$) [69]. The principal effect of surface roughness on ion-surface interactions is the replacement of a singular angle of incidence by a local distribution of incident angles with corresponding modifications of the sputter and reflection yields. The energy range of incident particles both in fusion and plasma processing applications can be as low as $10-100\,eV$. At such energy scales, the geometric features of the surface become important as the range of the incident particle becomes comparable to surface roughness. Efforts at implementing surface roughness effects using fractal geometry considerations [162], determination of local angular distributions from STM measurements [163], or introduction of 2-D (depth and lateral scale) surface geometry [71] in simulations exists. However, the simulations are restricted by the difficulty in determining the fractal dimension in the first case, while for the latter cases, the surface roughness must be measured before or after to provide the inputs and is therefore not predictive. In the case of Bizyukov et al. [71], the results are also qualitative due to the fit of a 2-D surface topology to 3-D experimental data, and additional computational times are required from the increased complexity.

TRIDYN calculations used in this study assume perfectly smooth surfaces with the 1-D elemental change in surface composition calculated only as a function of depth. Therefore, in order to avoid incorrect interpretation from comparing experimental results with idealized TRIDYN results, AFM measurements were performed for specimens before and after irradiation to determine the evolution of surface roughness and to estimate the magnitude of corresponding effects on the measured C implantation and W sputtering behavior.

AFM images for C-only irradiation of W at different temperatures for 3 locations both on and 1 location off the beam spot are shown in Fig. 4.1. The C flux is uniform in the central part of the beam where ion beam analysis is performed following each irradiation step (black column), but can vary laterally by ±30% with the effect most pronounced at the beam edges. In general, the C flux is lowest at the left edge and highest at the right edge as seen from the BVS image in Fig. 3.14. Therefore, by scanning horizontally across the specimen from an unexposed area towards the beam maximum, the qualitative evolution of the surface topography with increasing fluence can be observed. The roughness evolution with increasing fluence shown in Fig. 4.1 does not correspond to one location, but three different locations on the same specimen irradiated to a difference in total fluence.

First, Fig. 4.1 shows that the heating process alone for $T \geq 770\,K$ (first column) results in a $\approx 50\%$ increase of R_q value compared to $T < 770\,K$ as previously seen in section 3.3.2. The mean ion range of $6\,keV$ C ions in tungsten is $\lambda = 10-15\,nm$, and therefore surface roughness effects cannot be neglected for irradiation at $T \geq 770\,K$. Second, for all specimens, the R_q value increases with the growth of a C layer. At RT, this is mainly due to the presence of pores in the C layer but at elevated temperatures, the inhomogeneous growth of the C layer in the form of island structures

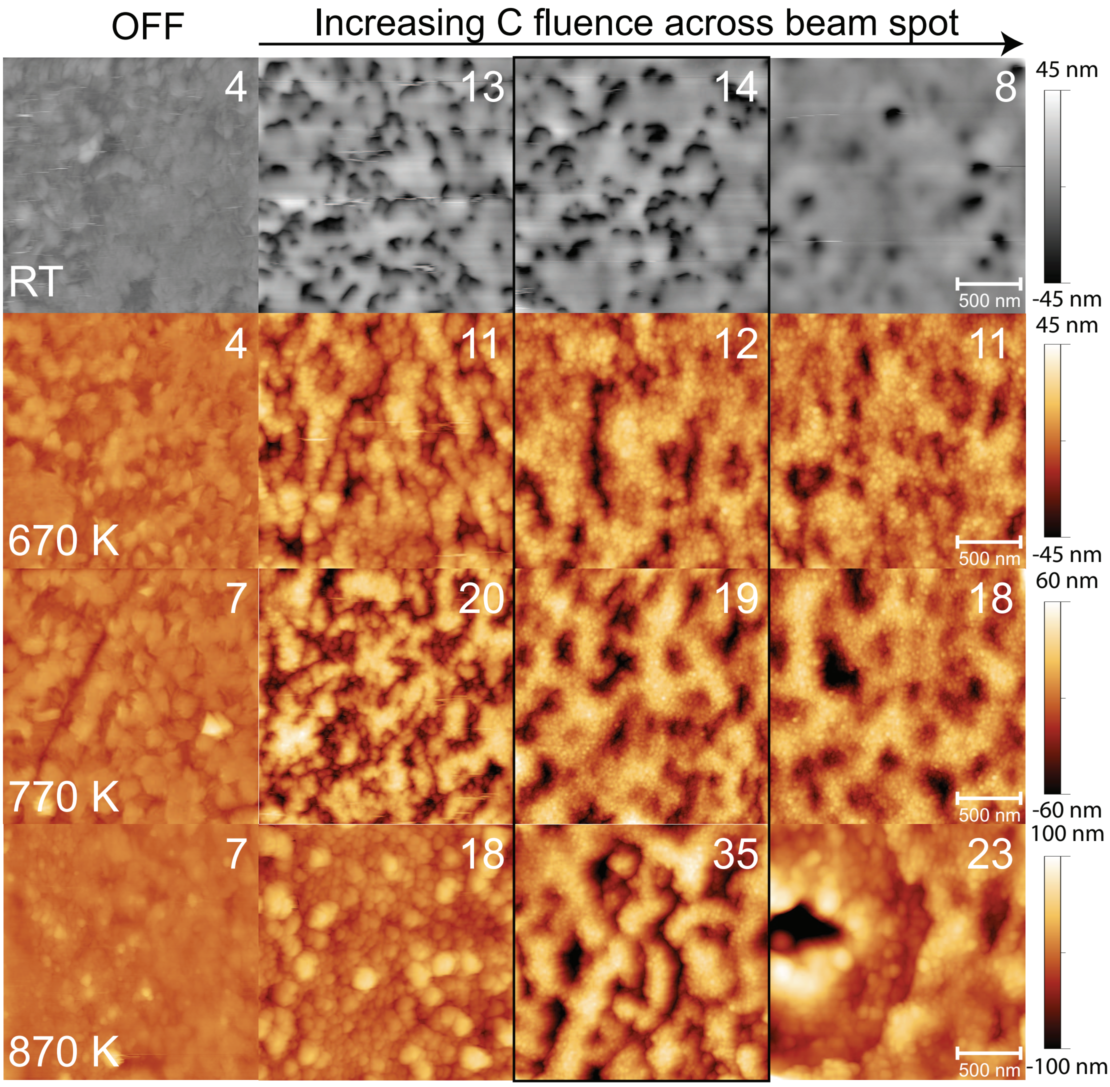
OFF
Increasing C fluence across beam spot
4
13
14
8
RT
500 nm
45 nm
-45 nm
4
11
12
11
670 K
500 nm
45 nm
-45 nm
7
20
19
18
770 K
500 nm
60 nm
-60 nm
7
18
35
23
870 K
500 nm
100 nm
-100 nm

Figure 4.1: AFM measurements of C-only irradiation specimens presented in Fig. 4.4 for both on- and off- beam spots at *RT*, 670 *K*, 770 *K*, and 870 *K*. The numbers indicate the RMS surface roughness values, R_q in *nm*. The column outlined in black corresponds to the location on each specimen where the fluence dependent C and W areal density changes was measured by ion beam analysis and presented in Fig. 4.4. Therefore, these images correspond to the surface topographies and R_q values following the final irradiation step.

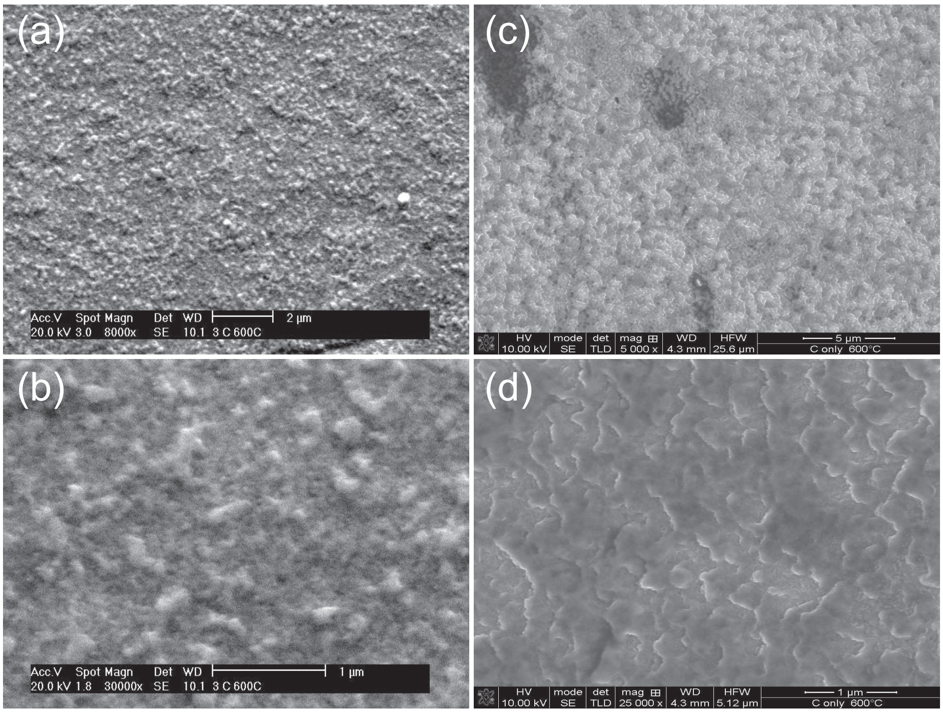
(a)
Acc.V Spot Magn Det WD 2 µm
20.0 kV 3.0 8000x SE 10.1 3 C 600C
(c)
HV mode det mag WD HFW 5 µm
10.00 kV SE TLD 5 000 x 4.3 mm 25.6 µm C only 600°C
(b)
Acc.V Spot Magn Det WD 1 µm
20.0 kV 1.8 30000x SE 10.1 3 C 600C
(d)
HV mode det mag WD HFW 1 µm
10.00 kV SE TLD 25 000 x 4.3 mm 5.12 µm C only 600°C

Figure 4.2: SEM images showing the surface morphology at different magnification: (a,b) before full C coverage, and (c,d) after full C coverage.

mainly contribute to the increase in surface roughness. Third, at elevated temperatures, the C layer is observed to grow in cluster sizes of $\approx 10\,nm$ which in turn are networked to form larger island like structures. Such surface topography is typical of surface growth processes [166] where the surface C atoms are mobile and can coalesce to form 3-D structures. This is in contrast to the very smooth surfaces observed at RT, which is in accordance to the sub-plantation model [167] where C layer growth occurs by implantation into the material.

The morphology of the initially sputtered W surface from SEM images is shown in Fig. 4.2(a,b). Clearly visible are W island structures, which are formed by inhomogeneous sputtering of the surface. This may be due to yield variations for different lattice orientation of grains at the surface. The corresponding surface roughness is $R_q \approx 10\,nm$. This initial surface topography of peaks and valleys provides in the following irradiation, the basis for C layer growth. According to Fig. 4.1, the C layer evolves by first following the initial surface morphology, but then roughness increases with growth of a C layer on top of the surface. Above a certain threshold, further increase in C fluence results in merging of the growing C structures, resulting in the valleys to become filled and corresponding decrease of R_q values. SEM images following full coverage of the W surface by a C layer after irradiation is shown in Fig. 4.2(c,d). The growth pattern clearly shows the effect of the 15° inclination of C ion's angle of incidence and the preferred growth orientation of the C layer.

The Raman spectroscopy [168] spectrum shows that the C layer is similar in structure to highly disordered carbon with broad D and G peaks. The results are presented together with C layer formed under simultaneous irradiation in Fig. 5.4 in section 5.

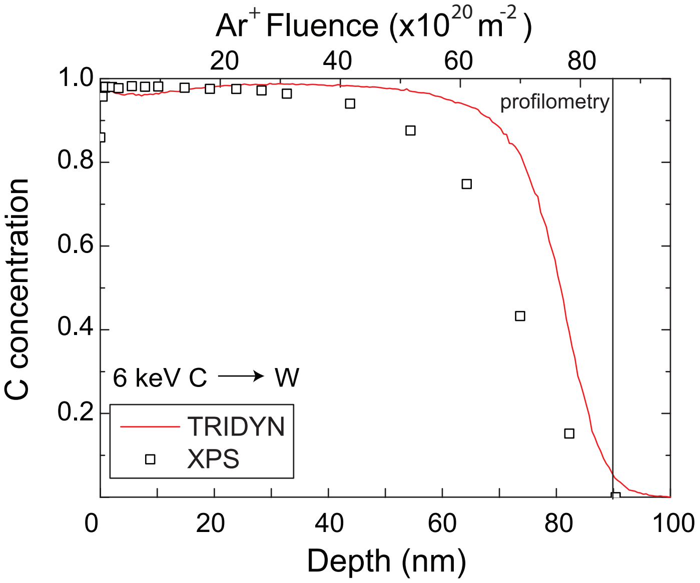

Figure 4.3: Comparison of XPS and TRIDYN depth profiles for C-only irradiation at RT. The black line indicates the sputter depth measured by profilometry following XPS.

From the wavelength of the laser used ($514.5\,nm$), only the sp^2 content in the grown C layer can be determined. However, carbon films with different sp^3- to sp^2- ratios tend to graphitize when annealed to temperatures higher than $670\,K$ [169]. Also, radiation damage by ions via atomic displacements graphitize even real diamond surfaces [170], and therefore in present experiments low sp^3 amount in the growing C layer is expected. This requires experimental verification using UV-excitation mode ($325\,nm$), which at the time of measurement in Karlsruhe was not available. Since the threshold for atom displacement in graphite by H impact is $124\,eV$ [171], the initial crystalline structures of carbon facing the boundary plasma in a fusion device will likely be transformed into the amorphous disordered C structure similar to those observed in this study.

4.1.2 XPS depth profiling

To determine the thickness of the C deposition layer and to measure the change in C concentration with depth in the C-W mixed material layer, XPS depth profiling was performed for a C-only irradiation specimen at RT. Fig. 4.3 shows the result of the calculated TRIDYN depth profile following an implanted C amount of $n_c = 0.85 \times 10^{22}\,m^{-2}$. This areal density corresponds to the experimental amount implanted following irradiation up to a C fluence of $F_c = 2 \times 10^{22}\,m^{-2}$ measured by ion beam analysis as seen in Fig. 4.4.

The XPS results are plotted against the Ar fluence such that the end point matches the depth of the sputter crater measured by profilometry. Since the Ar fluence does not scale linearly with depth, it is difficult to quantitatively compare the two depth profiles. However, XPS measurements and TRIDYN calculations are in good agreement at the depth where the C implantation zone ends at $90 - 100\,nm$. From this comparison, it is inferred that TRIDYN can approximate the implanted C depth profile during C-only

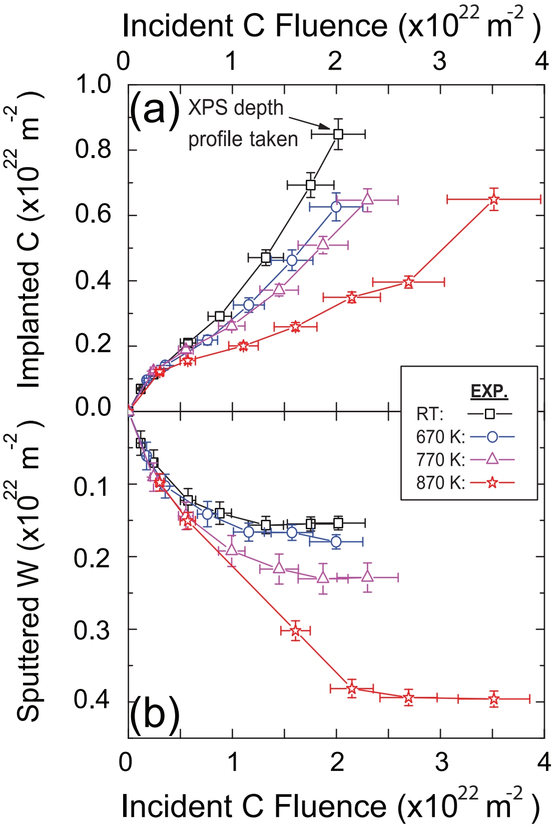

Figure 4.4: C-only irradiation of W at $RT - 870\,K$. Plotted is the: (a) implanted C areal density, and (b) sputtered W areal density as function of incident C fluence.

irradiation.

4.2 Carbon-only irradiation of Tungsten

The C-implantation and W-sputtering behavior at C-only irradiation is plotted in Fig. 4.4 for varying temperatures as a function of the incident C fluence. Fig. 4.4(a) shows a strong temperature dependence of the growth rate of implanted C areal density, n_c. Correspondingly, one observes that the decrease of the C growth rate with increasing temperature results in increased amount of W sputtered. This inverse relationship of sputtered W and C growth rate becomes clearer by plotting the W sputter yield against n_c as shown in Fig. 4.5(a). The W partial sputter yields were obtained by fitting the curves in Fig. 4.4(b) with a first order exponential decay function and taking the slope at each point. TRIDYN calculation is also plotted for incident angle of $\alpha_T = 15°$.

First, at $T < 770\,K$, Fig. 4.5(a) clearly shows that there is no temperature dependence to the W sputter yield. This means that the experimental results can be well described by purely kinematic effects of a smooth 1-D planar model used in TRIDYN, and temperature dependent processes like C segregation and diffusion can be neglected. TRIDYN calculations slightly overestimates the W sputter yield for $T < 770\,K$. Meaning, the total amount of W sputtered calculated by TRIDYN for a given incident C fluence will be larger compared to the experimental results at $T < 770\,K$.

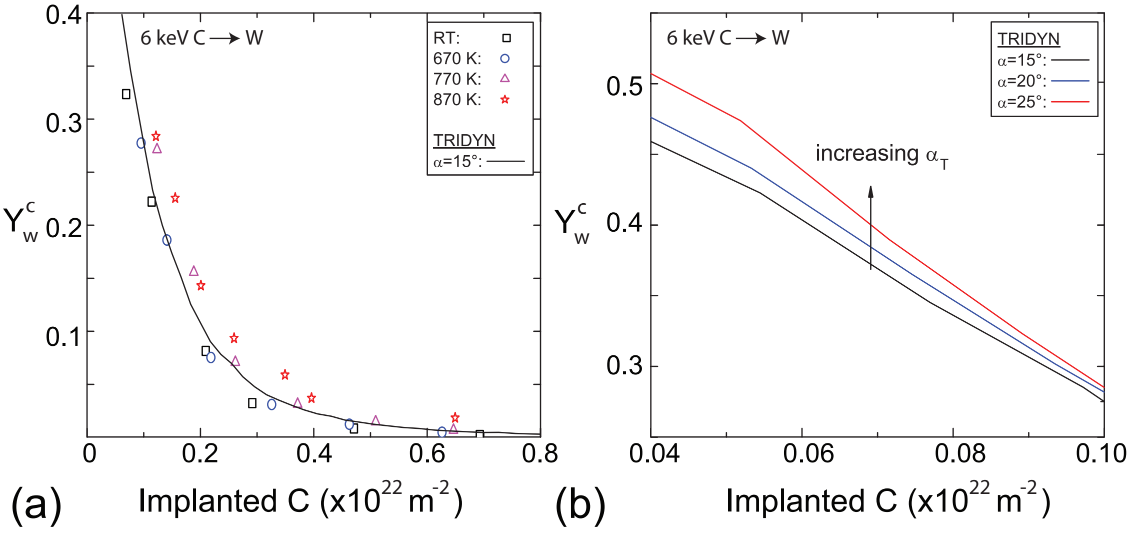

Figure 4.5: Comparison of: (a) Experimental W sputter yield as a function of implanted C areal density, n_c at various temperatures with TRIDYN calculation using the $SBEs$ corresponding to RT, and (b) the effect of incident angle, α_T, in the W sputter yield calculated by TRIDYN at low implanted C areal density corresponding to low C surface coverage.

Second, at $T \geq 770\,K$, deviation between experimental results and TRIDYN calculations is seen from Fig. 4.5(a). The underestimate of the W sputter yield by TRIDYN at $T \geq 770\,K$ could be interpreted by C diffusion to the surface, resulting in enhanced C sputtering with corresponding increase in W sputtering by increased W surface concentration. However, C diffusion in W is negligible at $T = 770\,K$ [93], and therefore changes to the C surface concentration by diffusion effects can be neglected. The onset of C diffusion in W has been observed at $T \approx 870\,K$ [63] and is highest at low C concentrations [93]; meaning diffusion effects will be most pronounced at low amounts of implanted C. Yet, comparison of the W sputter yields below $n_c < 0.2 \times 10^{22}\,m^{-2}$ between $T = 770\,K$ and $T = 870\,K$ experimental results show little deviation. Therefore, C diffusion in W at $T = 870\,K$ and its corresponding effect on the C-implantation and W sputtering behavior can be assumed to be small for present experiments.

The deviation at $T \geq 770\,K$ between TRIDYN calculations and experimental results is explained by the departure of the experimental W specimen topography from the smooth surface model used in TRIDYN. Surface roughness effects increase the local distribution of incident angles as well as increasing the W surface area. The effect of increase in incident angle and its effect on W sputtering can be seen in TRIDYN calculations in Fig. 4.5(b). The effect is pronounced at low implanted C amount, corresponding to low C surface coverage. This is because the mean ion range of $6\,keV$ C ions in W ($\lambda = 10 - 15\,nm$) is comparable to the surface roughness resulting from heating at $T \geq 770\,K$ ($R_q = 7\,nm$) as well as the evolving surface topography of W island structures formed by the inhomogeneous sputtering process itself (see Fig. 4.2(b)). The peaks of such island structures in past studies [69, 71] were observed to be not fully covered by C and thus remained longer exposed to the incident C ions resulting in higher W sputter yields. However, the observation that the C layer grows in island structures indicate that W sputtering originates not from the peaks but from the valleys between the growing islands. Therefore, a rough surface contributes to increased W sputtering by: (a) increasing the W area and (b) by broadening the distribution of local incident angles for a given n_c at $T \geq 770\,K$.

It is important to note that n_c corresponds to the integrated amount of C in the initial mixed material and subsequent pure C layer ($\approx 50 - 200\,nm$) and not a measure of the actual C surface concentration (few monolayers). As discussed in section 2.1, surface concentration is a key parameter in describing sputter yields since most of the sputtered atoms originate from the first few monolayers. As seen from the correlation between the tungsten sputter yield and implanted carbon in Fig. 4.5(a), n_c can also parametrize the W sputter yield, indicating that a specific n_c corresponds to a certain C surface concentration. Unfortunately, the C surface concentration during experiments cannot be measured using the present experimental setup (requires in-situ XPS or Auger spectroscopy).

However, at $T < 770\,K$, TRIDYN calculation of the W sputter yield as a function of the implanted C shows good agreement with the experimental results (see Fig. 4.5). This means that the C surface concentration calculated by TRIDYN for corresponding n_c can be used as a first approximation of the actual C surface concentration in experiments. The C and W surface concentration calculated by TRIDYN averaged over three different depths are plotted in Fig. 4.6(a). With increasing average depth, the concentration of C increases due to the larger depth sampled. However, the difference in C concentration is $< 5\%$ for different sampling depths. Since the RMS surface roughness is below $10\,nm$ in the initial W erosion regime, it seems most appropriate to use the W surface concentration values averaged over $5\,nm$. Using the curve in Fig. 4.6(a), the x-axis of Fig. 4.5(a) can be converted from implanted C areal density to C surface concentration as seen in Fig. 4.6(b). At $T \geq 770\,K$, n_c can no longer correctly parametrize the W sputtering process since a certain n_c will no longer represent the correct local C surface concentration but instead a lateral average over the area of the analysis beam spot. A method to overcome this is discussed in section 6 and used in the phenomenological model.

4.2.1 Parametric representation

To allow a clearer distinction between continuous W erosion and continuous C deposition regimes, the sputtered W areal density is re-plotted in a parametric representation as function of the implanted C areal density as shown in Fig. 4.7. To understand the physical meaning of the curves, we introduce the rate differential equations governing the implanted C and sputtered W areal densities, n_c and n_w, respectively:

$$\frac{dn_c}{dt} = \Phi_{\mathrm{c}}\,(1 - R_{\mathrm{c}} - Y_c^c) \tag{4.1}$$

$$\frac{dn_w}{dt} = \Phi_{\mathrm{c}}\,Y_w^c \tag{4.2}$$

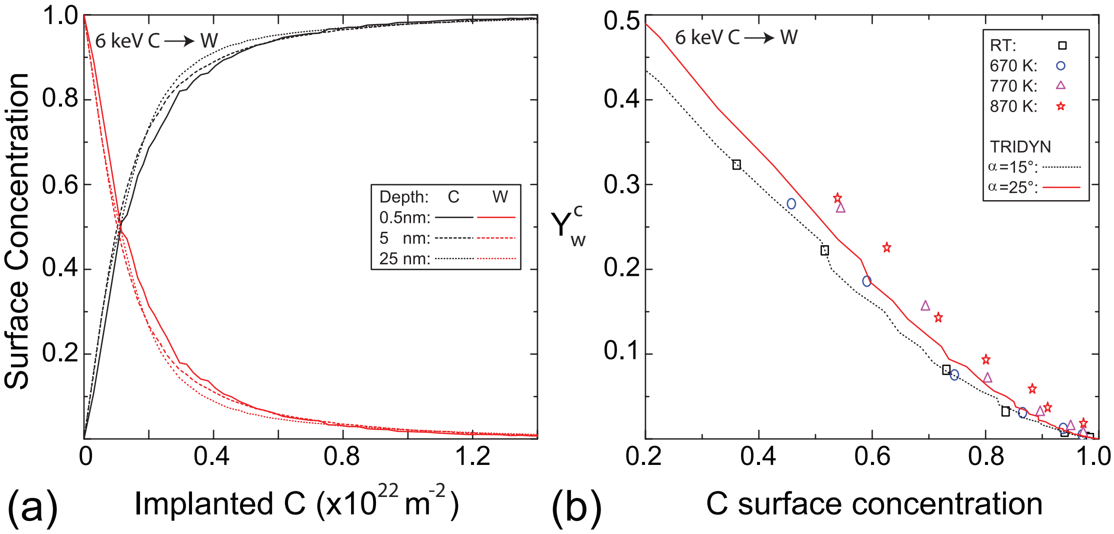

Figure 4.6: (a) Surface C and W concentrations calculated by TRIDYN plotted against the total implanted C areal density for varying averaged depths. (b) Fig. 4.5(a) re-plotted as a function of the C surface concentration.

where Φ_c is the C flux, R_c is the C reflection coefficient, and Y_a^b the sputter yield of target element a irradiated with projectile element b. A simple substitution for $\Phi_c\, dt$ will yield:

$$\frac{dn_w}{dn_c} = \frac{Y_w^c}{(1 - R_c - Y_c^c)} \tag{4.3}$$

Therefore, $dn_w/dn_c = 0$ means $Y_w^c = 0$ (i.e no W sputtering occurs), whereas $dn_w/dn_c = 1$ means that the C implantation and W sputtering processes are in equilibrium (i.e. W is continuously sputtered with yield $Y_w^c = (1 - R_c - Y_c^c)$). Fig. 4.7 shows that for all temperatures $dn_w/dn_c = 0$ is reached eventually, corresponding to the buildup and further growth of a closed C layer protecting the underlying W from further sputtering. The C areal density required to protect W from further sputtering is $n_c \approx 0.4 \times 10^{22}\, m^{-2}$ for all temperatures. Initially, no temperature dependence is observed in the implantation sputtering curves, however at $n_c \approx 0.1 \times 10^{22}\, m^{-2}$, corresponding to $n_w \approx 0.07 \times 10^{22}\, m^{-2}$ ($\approx 11\, nm$ of W sputtered), a temperature dependence can be seen. This indicates that the surface roughness increase from the annealing at temperatures $\geq 770\, K$ has a minor effect in the W sputtering behavior because if the effects were large, then it would be strongly observed at $n_c < 0.1 \times 10^{22}\, m^{-2}$. Therefore, the temperature effect on the W sputtered amount must arise from the reduction in C surface coverage for a given n_c, either by increased C sputtering or the formation of C clusters on the surface that expose a larger amount of W underneath.

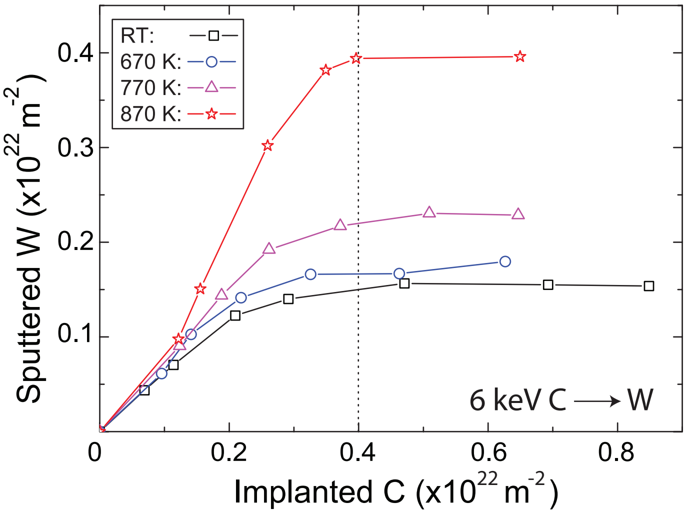

Figure 4.7: Parametric representation of C-only irradiation of W at various temperatures.

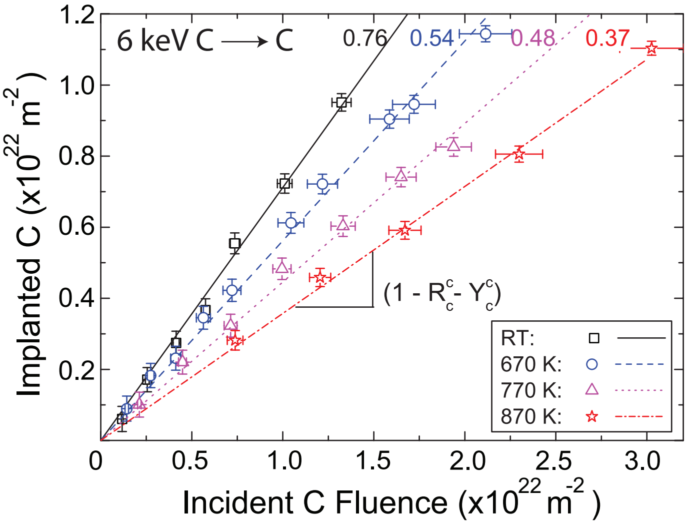

Figure 4.8: The increase of implanted C amount with increasing incident C fluence for temperature range $RT - 870\,K$ for C films irradiated by 6 keV C ions. The implanted C amount is the difference between the initial C areal density measured by NRA and the subsequent increase measured with each irradiation step. The numbers indicate the slope of the linear fit.

4.2.2 Carbon self-sputtering and comparison to TRIDYN

In previous experiments [60, 76], it was discovered that the C self-sputtering yield (Y_c^c) depends on temperature. This process is known as radiation enhanced sublimation (RES) and the C self-sputtering yield follows an exponential temperature dependence. RES involves the formation of C interstitials due to energy deposition in the near surface layer with subsequent diffusion of the C atoms to the surface which are weakly bound and are easily sputtered [76]. However C diffusion in C is negligible at $T < 970\,K$ [60], and therefore the increase in the C self-sputtering yields can be directly correlated to the decrease in surface binding energies at the present temperature range studied $(670 - 870\,K)$.

The increase in C self-sputtering with increasing temperature can be described in TRIDYN calculations by appropriate reduction of the surface binding energies ($SBEs$). The $SBEs$ used for TRIDYN calculations were determined experimentally by the following two steps: (1) C films deposited on polished W substrates were irradiated by $6\,keV$ C ions and the experimental C self-sputtering yield as a function of temperature was obtained. (2) A scan varying the $SBEs$ in TRIDYN was done to obtain the dependence of the C self-sputtering yield, and the resulting fit was used to obtain the $SBEs$ equaling the experimentally determined Y_c^c in step 1.

Temp	Slope	Y_c^c
RT	0.76±0.01	0.24±0.01
$670\,K$	0.54±0.03	0.46±0.03
$770\,K$	0.48±0.03	0.52±0.03
$870\,K$	0.37±0.05	0.63±0.05

Table 4.1: Experimentally measured carbon self-sputtering yields.

The increase in C areal density with increasing incident C fluence is shown in Fig. 4.8. The amount of C implanted was measured using NRA and was determined by subtracting the initial C areal density. According to Eqn. 4.1 in section 4.2.1, the slope in Fig. 4.8 equals $1 - R_c^c - Y_c^c$ or $1 - Y_{tot}$. The reflection yield of C on C (R_c^c) at $\alpha = 15°$ is roughly two orders of magnitude smaller than Y_c^c [90]. Therefore, neglecting R_c^c, the slope of the linear fits in Fig. 4.8 is equal to $1 - Y_c^c$. The resulting values of Y_c^c are listed in Table 4.1. The RT measurement is closer to the value measured in Ref. [88] than Ref. [87]. The measured yields are in good agreement at $T \leq 670\,K$, but are larger at $T > 670\,K$ compared to the exponential fit based on experimental C self-sputtering yields in Ref. [60] (see Fig. 4.9). The increased C self-sputtering yields are attributed to the higher incident ion energies ($6\,keV$) used in the present study in comparison to Ref. [60] ($2.4\,keV$), which result in increased energy deposition in the near surface region.

In order to determine the SBE_c values based on the experimental C self-sputtering yields, a scan varying SBE_c in TRIDYN was done to determine the dependence of Y_c^c. An exponentially decreasing function Eqn. 4.4 was fitted to the scan results as seen in Fig. 4.10:

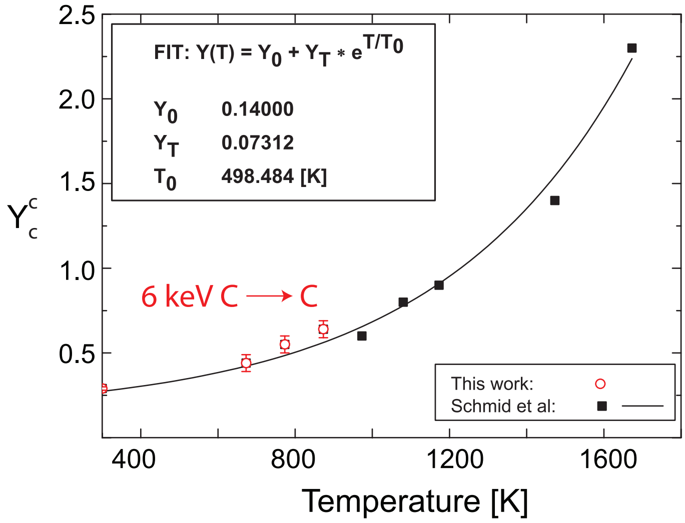

Figure 4.9: Comparison of C self-sputtering yield against Schmid et al. [60].

$$SBE_c^{'}(Y_c^c) = 1.4 + 13.7e^{-Y_c^c/0.3} \tag{4.4}$$

According to Eqn. 4.4, SBE_c of 4.3, 3.8, and 3.1 eV are required to correctly model the measured values of Y_c^c at temperatures 670 K, 770 K, and 870 K. For a system involving more than one element, the effective SBE of each target component can be chosen in dependence of the actual surface composition in TRIDYN using Eqn. 4.5:

$$SBE_i = \sum_{j=1}^{NCP} SBV_{ij} \cdot c_j \tag{4.5}$$

where NCP is the number of components, SBV_{ij} is the SBE of a surface atom i, to a target atom j, and c_j is the surface atomic fraction of a target atom j ($1 \leq j \leq NCP$, $\sum c_j = 1$). For the two component C-W system, the SBV_{ij} was obtained by averaging the SBE of pure W ($SBE_w^{'}$) and C ($SBE_c^{'}$) materials using Eqn. 4.6:

$$SBV_{ij} = \frac{1}{2}(SBE_w^{'} + SBE_c^{'}) \tag{4.6}$$

For all TRIDYN calculations, the SBE of W to W is taken as $SBV_{ww} = SBE_w^{'} = 8.68\,eV$ from the heat of sublimation value, while the SBE of W to C is taken as $SBV_{wc} = 8.0\,eV$ from the average of $SBE_w^{'}$ and $SBE_c^{'}$ values at RT using Eqn. 4.6. Physically, this represents the assumption that tungsten sputtering is independent of temperature and tungsten carbide formation. The SBE of C to C ($SBV_{cc} = SBE_c$) at different temperatures was determined using Eqn. 4.4, while the SBE of C to W is determined using Eqn. 4.6. The different values of the SBV_{ij} used in the following TRIDYN calculations are summarized in Table 4.2.

The experimental results from C-only irradiation of W were now compared to cor-

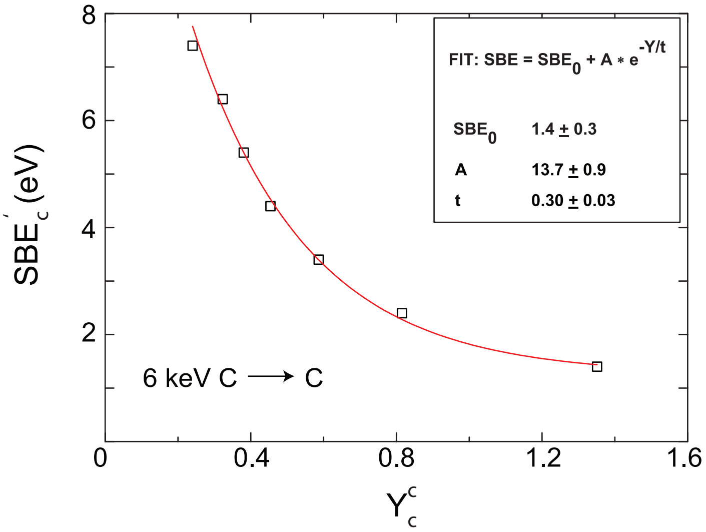

Figure 4.10: Parameter scan in TRIDYN to determine the dependence of Y_c^c on SBE_c.

Temp	$SBV_{\rm cc}(eV)$	$SBV_{\rm cw}(eV)$	$SBV_{\rm wc}(eV)$	$SBV_{\rm ww}(eV)$
RT	7.4	8.0	8.04	8.68
$670\,K$	4.3	6.5	8.04	8.68
$770\,K$	3.8	6.3	8.04	8.68
$870\,K$	3.1	5.9	8.04	8.68

Table 4.2: Experimentally measured carbon self-sputtering yields and the SBV_{ij} used in all TRIDYN calculations to simulate the increased C self-sputtering with temperature.

responding TRIDYN calculations as plotted in Fig. 4.11. Increased incident angles were chosen to approximate the increase of surface roughness with growing C layer as discussed in section 4.1.1. At RT and $670\,K$, the C implantation behavior is best fitted for $\alpha_T = 20°$, however the W sputtering behavior is better described assuming the actual value of $\alpha = 15°$. The results are consistent with the observed growth dynamics of the C layer in a radial direction from the W island structures. Basically, the W sputtering contribution arises mainly from the valleys or “floor” of the surface. However, the growing C layer includes also the morphology of the island structures, resulting in increased sputtering of areas with steeper slopes due to the angular dependence of physical sputtering. At $770\,K$, both W and C sputtering behavior is best described assuming $\alpha_T = 20°$. In this case, due to the higher C sputter yields, the valleys will remain exposed for a higher C fluence with the additional effect of an initially rougher surface from the heating process (see first row of Fig. 4.1). At $870\,K$, the C sputtering behavior is best described assuming $\alpha = 25°$, but large deviations in the W sputtering behavior is seen. With the available diagnostics it could not be resolved whether this effect is due to the combination of surface morphology and increased C self-sputtering, or from the onset of C diffusion from the implantation range. In summary, for $T < 870\,K$, the experimentally derived $SBEs$ provide a good description of the experimental data by the TRIDYN model, with deviations only arising from the experimental surface

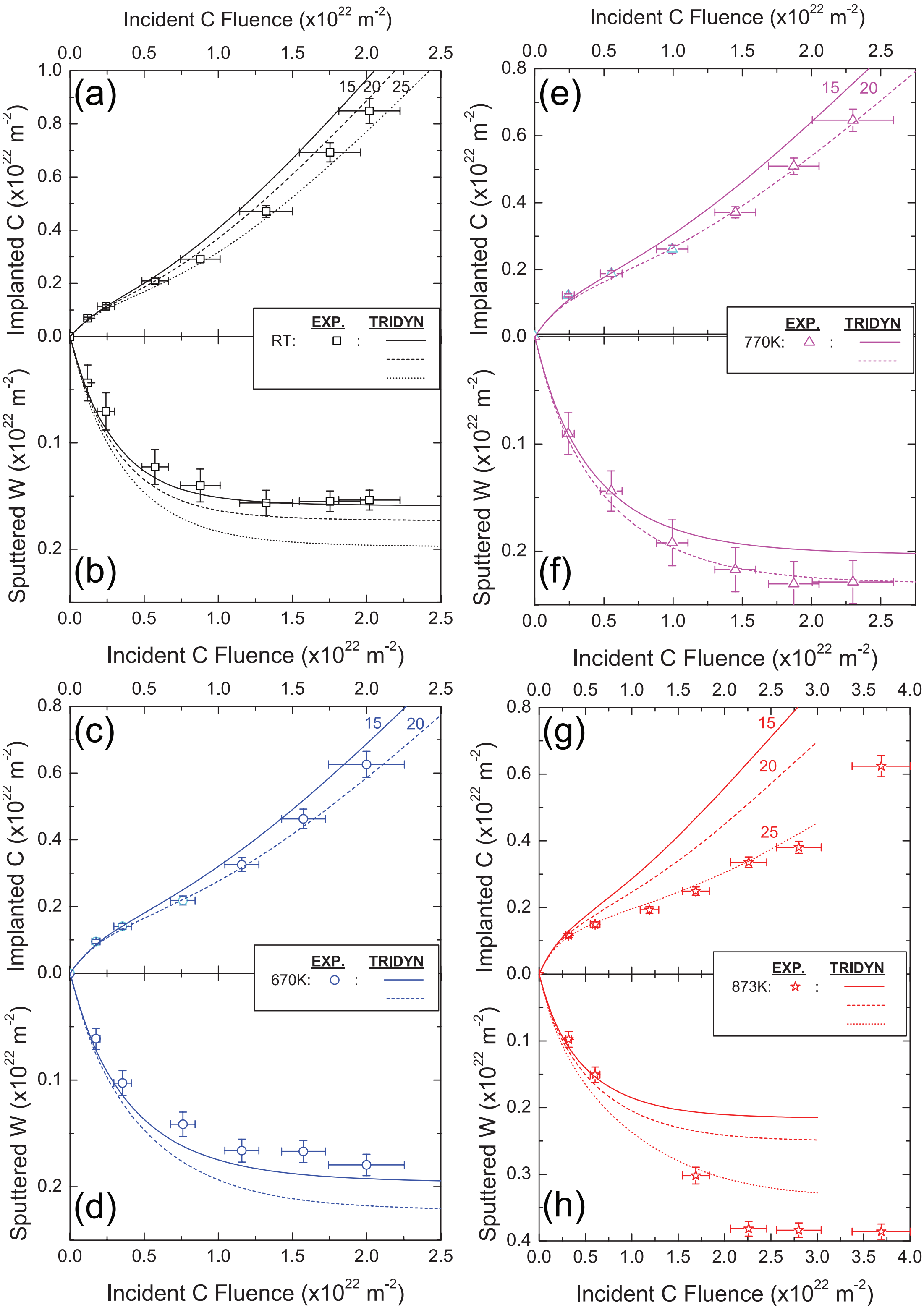

Figure 4.11: Comparison of TRIDYN calculations using SBV_{ij} from Table 4.2 with experimental data presented in Fig. 4.4. The numbers indicate the angle of incidence, α_T, used in TRIDYN simulations.

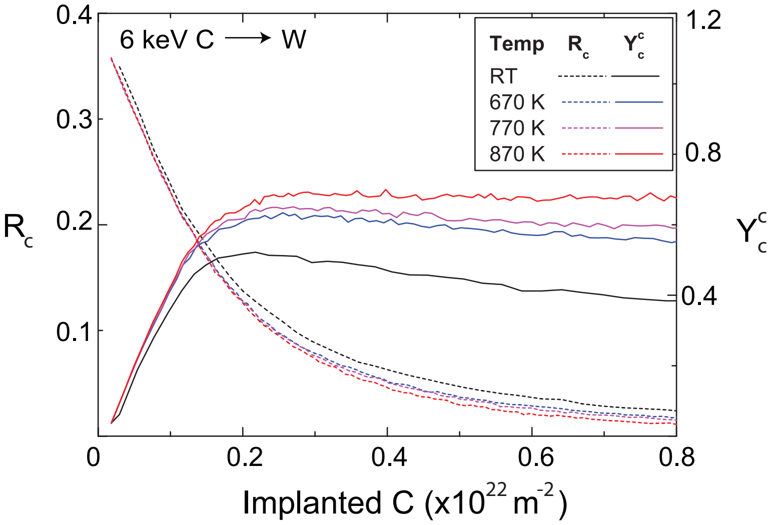

Figure 4.12: Calculated TRIDYN values of the C reflection and sputter yields as a function of implanted C for temperatures RT, $670\,K$, $770\,K$, and $870\,K$.

morphology compared to the planar 1-D surface assumed in TRIDYN. Modeling the system at $T = 870\,K$ becomes difficult due to the added uncertainty of diffusion effects.

The linear growth of C for $n_c \geq 0.4 \times 10^{22}\,m^{-2}$ with increasing fluence as seen in Fig. 4.11 indicates steady state C layer growth. However, TRIDYN calculations reveal that the reflection and sputter yields are still changing (see Fig. 4.12). Specifically, the reflection yield cannot be assumed to be zero nor the sputter yield to be equal to the C self-sputtering yields. Consequently, one has to acknowledge that the maximum C fluence achievable in the dual beam experiment in one experiment day do not allow to reach true steady state conditions. However, an important result of the simulations is that Y_c^c has a maximum at $n_c \approx 0.25 \times 10^{22}\,m^{\text{-}2}$. This can be explained by the fact that the scattering efficiency for C on W is greater than that of C on C due to the large mass difference in the former case. As the surface becomes enriched with C, the incident C ions will penetrate through the C layer formed and are reflected from the underlying W atoms knocking off C atoms on their way out or depositing energy into the surface region. With increasing C layer thickness, the amount of C ions reflecting from the underlying W decreases along with the energy deposited near the surface, resulting in a corresponding decrease of the sputter yield, which finally approaches the C self-sputter yield. The TRIDYN calculations also reveal the reason why Y_c^c fails to reach the experimentally measured C self-sputtering yields by the fact that the W fraction in the near surface layer never approaches zero in the considered fluence range.

Therefore, it is important in the case of light elements like C implanted in a heavy element like W, to consider not only the surface concentration of C, but also the depth profile and thickness of the C layer to properly understand the C sputtering behavior. Similar influence of reflective scattering collisions at high mass differences have been observed for D irradiation of C layers on W [172] as well as in the oscillation behavior of C sputtering by W [173].

4.2.3 Summary

Carbon-only irradiation of tungsten at elevated temperature was performed to fully characterize the C implantation and W sputtering behavior by C-ions only. For $T < 870\,K$, W sputtering and C layer growth are well described by the TRIDYN binary collision model using $SBEs$ derived from C self-sputtering measurements. Deviations from TRIDYN can be interpreted as surface morphology effects and the different dynamics of C layer growth from a smooth 1-D plane as compared to a realistic rough surface. At $T = 870\,K$, significant deviations from TRIDYN calculations arise from contributions of enhanced C self-sputtering and surface morphology, as well as possible onset of C diffusion from the implantation zone. The relative importance of the respective effects could not be determined with the presently available diagnostics. The C sputtering behavior depends on both the surface C concentration and the C depth profile, while W sputtering is parametrized by the C areal density.

5 Simultaneous irradiation by Deuterium and Carbon ions

Under fusion relevant conditions, plasma exposed tungsten (W) surfaces will face an influx of hydrogen fuel ions along with carbon (C) impurities. Increased C self-sputtering with temperature was shown to increase W sputtering by C due to the more efficient removal of C previously implanted in the W surface (section 4.2.2). Since C is chemically eroded by D at low energies and elevated temperatures, it is expected that in the case of simultaneous irradiation, C sputtering may further increase. Therefore, the dynamics of W sputtering and C implantation will depend on the sputtering effects caused by both C and D. In general, simultaneous irradiation results in one of the two principal regimes where either W erosion or C deposition dominates depending on the C fraction in the incident flux, f_c. Of particular importance and application to fusion research is the prediction of the transition point from erosion to deposition as it separates areas of continuous erosion from areas of C layer formation. C layer formation is important due to the issue of co-deposition and tritium inventory. Also, C layers affect the W sputtering behavior, which is of importance in estimating W impurities that can radiate away energy of the core plasma.

Implantation sputter curves for simultaneous irradiation at RT for various values of f_c in the incident ion flux are plotted together with respective TRIDYN calculations in Fig. 5.1. The two regimes of W erosion and C deposition and their dependence on the f_c is clearly seen from Fig. 5.1. The experimental results indicate that the transition point from continuous W erosion to C deposition regime lies in the interval $0.07 < f_\mathrm{c} < 0.11$, which is in the predicted range of $0.07 < f_\mathrm{c} < 0.08$ from TRIDYN. Unfortunately, better resolution within this region could not be achieved in the present work, since higher f_c's are achieved by lowering the D flux; meaning the C beam fluctuations (which are significantly higher than the D beam) become a limiting factor for maintaining a constant f_c throughout the entire irradiated fluence. Because of this experimental uncertainty, the resolution of 1% required to validate TRIDYN calculations cannot be reasonably met for experimental conditions where $f_\mathrm{c} > 0.07$ in the entire irradiated fluence range. However, it is possible to maintain a constant f_c for a limited fluence step, and by reducing the value of $f_\mathrm{c} = 0.11$ to $f_\mathrm{c} = 0.09$, it was observed (section 5.3) that the system shifts from a C deposition regime to a W erosion regime. From this, it is inferred that the transition point lies in the interval $0.09 < f_\mathrm{c} < 0.11$ for simultaneous C-D irradiation of W by $6\,keV$ C and $3\,keV$ and D ions.

In addition, surface roughness effect was found to contribute to the shifting of the transition point. Two specimens were irradiated at $f_\mathrm{c} = 0.11$ with R_q values of 15 and $5\,nm$ (marked (a) and (b) in Fig. 5.1, respectively). In case (a), the rougher initial surface resulted in continuous W erosion, whereas the smoother surface in case (b) resulted in C deposition. Since the nominal parameters of the incident ion beam mix were identical, the difference can only be attributed to slight variations of the aforementioned beam fluctuations and surface roughness. Therefore, for simultaneous irradiation: (1) surface roughness effects must be characterized and its effect considered when experimental results deviate from simulations, and (2) the dynamical roughening of the surface during irradiation must be taken into account because it can result in a

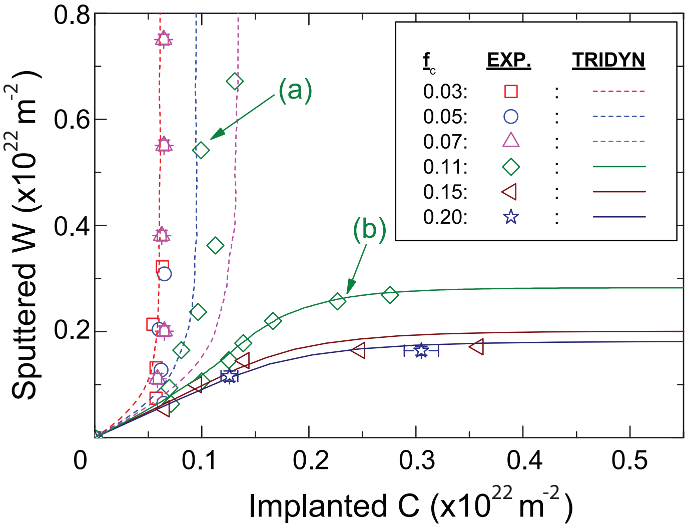

Figure 5.1: Implantation sputter curves for simultaneous irradiation at RT for various f_c compared against TRIDYN calculation using an incident angle of $\alpha_T = 15°$. Sample error bars for the C deposition and W sputtering regimes are shown. A discussion of the experimental results for $f_c \geq 0.11$ is found in section 5.1. The discrepancy between experimental results and TRIDYN for $f_c \leq 0.11$ will be discussed in section 5.2.

shift of the erosion-implantation dynamics, and depending on other parameters, affect the steady state end condition.

The following discussion is divided into two sections of carbon deposition and tungsten erosion regimes, respectively. The effect of increasing temperature on the erosion-implantation dynamics as well as the D retention behavior and its dependence on the implanted C is discussed in both sections. A phenomenological model presented in section 6 is used to determine the chemical sputtering component and is discussed in section 5.2.2.

5.1 Carbon deposition regime

In the carbon deposition regime, a pure C layer forms over the mixed C-W-D surface, shielding the underlying W from further sputtering. As seen in Fig. 5.1, C deposition takes place for $f_c \geq 0.11$ with the experimentally measured total amount of sputtered W within 10-20% of the TRIDYN calculations. The results are re-plotted as a function of the incident C fluence to show the evolution of the C-implantation and W-sputtering behavior in the C deposition regime (see Fig. 5.2). TRIDYN calculations systematically overestimates the amount of W sputtered which can be attributed to the overestimate of the W sputter yield by C ions previously observed at RT simulations in Fig. 4.5 in section 4.2. This discrepancy is primarily due to the uncertainty of the tungsten and carbon heat of sublimation values used as surface binding energies in TRIDYN calculations. Despite these uncertainties, a disagreement of 10-20 % between experimental results and TRIDYN calculations is considered very good, since deviations of normally a factor of two is observed in past experiments with TRIDYN

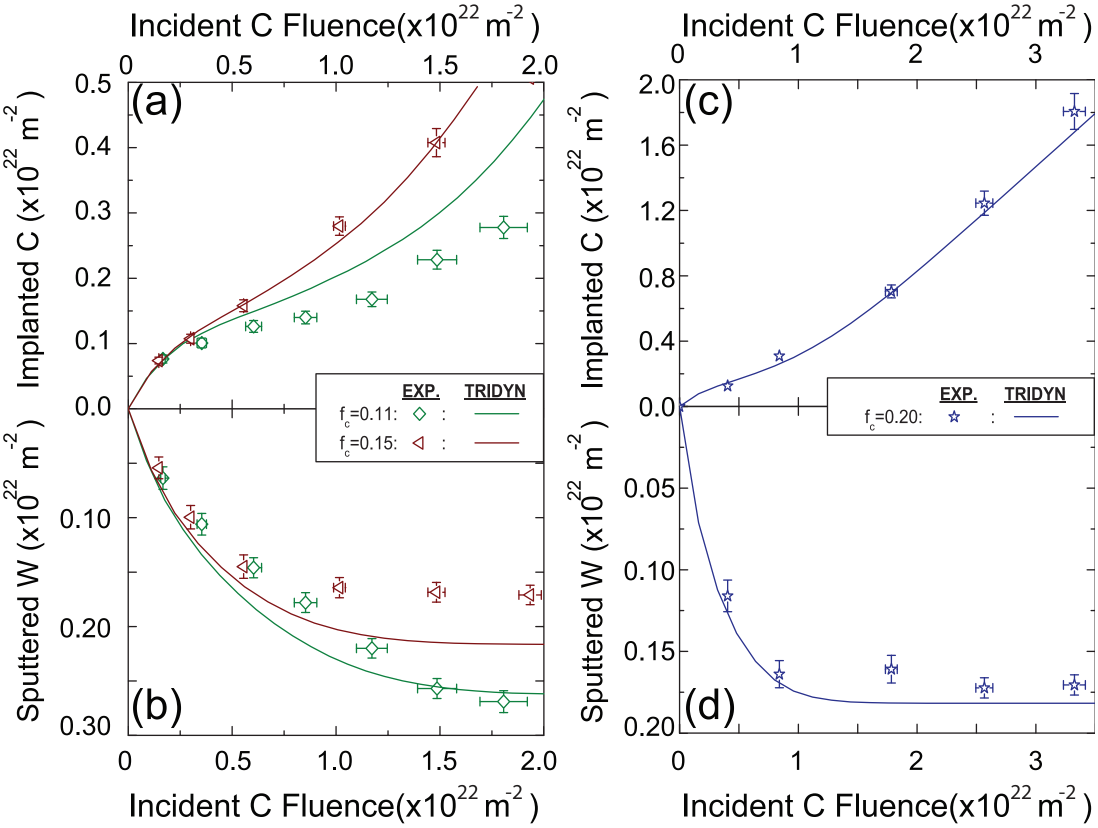

Figure 5.2: Comparison of: (a,c) C implantation, and (b,d) W sputtering behavior as a function of incident C fluence for varying values of f_c resulting in the C deposition regime. Also shown are results of TRIDYN simulations.

calculations [16]. This good agreement is due mainly to the formation of laterally smooth and uniform C surfaces grown with $R_q < 5\,nm$ as illustrated in Fig. 5.3. It is also noted that the disagreement between experiments and simulations is greatest for the $f_c = 0.11$ case indicative of a process not accounted for in TRIDYN. This discrepancy is due to a chemical sputtering process which will be discussed in greater detail in section 5.2.

Raman spectroscopy shows that the formed C layer under simultaneous irradiation has a similar structure to the C layer formed under C-only irradiation, with broad D and G peaks [174] indicating disordered graphite-like sp^2 bonding (see Fig. 5.4). Similar C structures are observed from C-W dust prepared by arc discharge [138] and in net deposition areas of a graphite limiter tile in TEXTOR [175].

5.1.1 Deuterium retention

The total amount of deuterium (D) trapped can be measured by NRA as outlined in section 3.3. At RT, the implanted D will diffuse through the W layer and into the Ni substrate, although trapping at the interlayer has to be considered as well. The cross section of the D(^{3}He, p)^{4}He reaction as a function of depth in pure C, W, and Ni materials is shown for ^{3}He energies of 0.69 and 2.5 MeV in Fig. 5.5. The cross-section

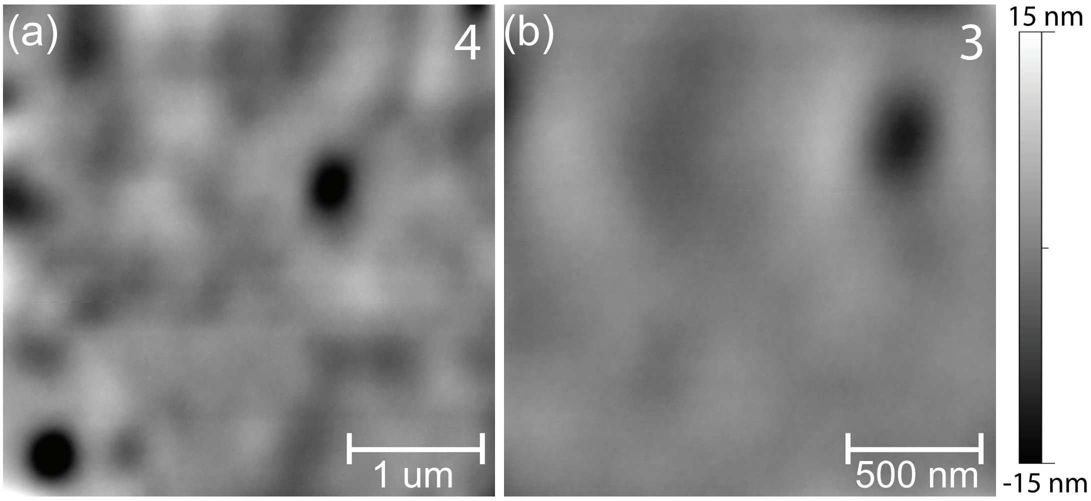

Figure 5.3: AFM images of the C surface layer grown during simultaneous irradiation at RT for $f_c = 0.20$ for scan area of: (a) $4\,\mu m \times 4\,\mu m$, and (b) $2\,\mu m \times 2\,\mu m$. The numbers indicate the roughness values, R_q in nm.

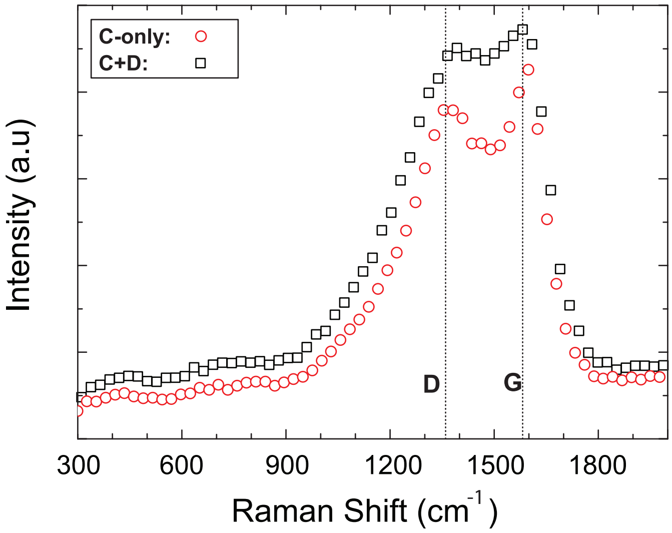

Figure 5.4: Raman spectroscopy results comparing the C layer growth by C-only irradiation (red circle) against simultaneous irradiation (black square). Also shown are the D and G peak locations at $1360\,cm^{-1}$ and $1550\,cm^{-1}$, respectively (from Ref. [174]).

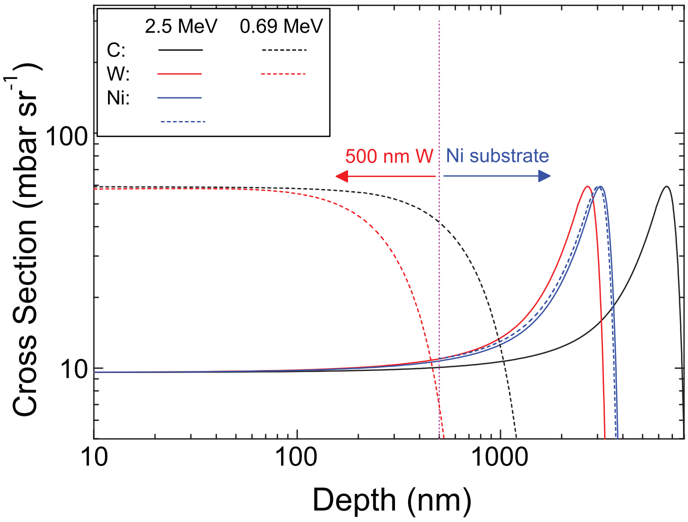

Figure 5.5: Changes in the cross section of 2.5 MeV D(^{3}He, p)^{4}He reaction as a function of depth for C, W, and Ni using the energy loss calculated by the TRIM.SP code [84] and using the cross section data of Ref. [176].

depth profiles were calculated using the energy loss calculated by TRIM.SP [84] and using the cross section data of Ref. [176].

First, from Fig. 5.5, it is clear that the 2.5 MeV D(^{3}He, p)^{4}He cross section is sufficiently constant within the depth range of the W film thickness for D trapped in W or C. Therefore, in principal, the energy of the collected protons resulting from ^{3}He-D nuclear reactions in the W film will scale with depth. However, it is clear that the cross sections in pure W increase at depths beyond 500 nm. For the present specimens, this means that a correspondingly disproportionate contribution of protons originating from D trapped in the Ni substrate must be taken into account. It is noted that the changes in cross section vs. depth is small in comparing pure W and Ni. Therefore at RT, the total D amount measured from the region $< 1\,\mu m$ consists of equally weighted contributions of D trapped from both tungsten and nickel. Deuterium trapping in Ni at $T \geq 670\,K$ is negligible [177], and therefore the substrate contribution from regions $>1\mu m$ can be neglected for experiments at elevated temperatures.

The D depth profile can be determined by the shape of both the proton and α-particle spectra from the D-^{3}He reaction. For ^{3}He primary energy 2.5 MeV, the energy of the α-particle is less than the energy of the backscattered ^{3}He ions from the tungsten material and cannot be separated. Therefore, the α-spectrum was measured at a ^{3}He primary energy of 0.69 MeV. A detector with a large solid angle (61.64 msr) is used for the detection of protons from nuclear reaction analysis due to the small reaction cross-sections for ^{3}He primary energy of 2.5 MeV. However, the corresponding weak energy resolution of the detector (20 eV) prevents depth profiling of D from the shape of the proton spectra. The protons from the D-^{3}He reaction are also not fully stopped within the detector resulting in further broadening of the proton spectra. However, as seen from Fig. 5.5, the cross section of the reaction for ^{3}He primary energy 0.69 MeV decreases sharply within the W film thickness and therefore proton contributions from the Ni substrate can be neglected in this case.

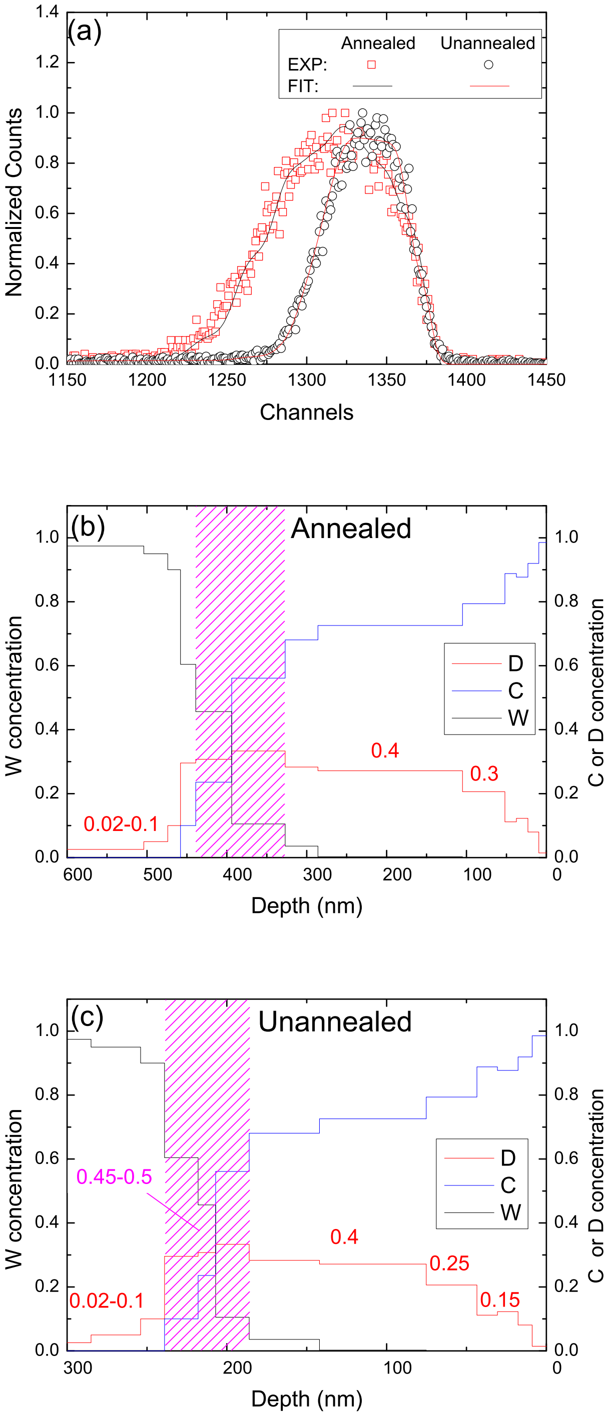

Figure 5.6: NRA α-spectrum at a scattering angle of 105° using the cross section of $0.69\,MeV$ D(^{3}He, ^{4}He)p reaction for $f_c = 0.20$ for an annealed and unannealed specimen. Shown are: (a) the raw data fitted with SIMNRA [158], and (b,c) converted to a depth scale assuming the densities of pure C and W. The numbers indicate the ratios of D/C, D/(C+W), and D/W at the indicated depth, while the C-W mixed material region is approximately highlighted by the hatched magenta box.

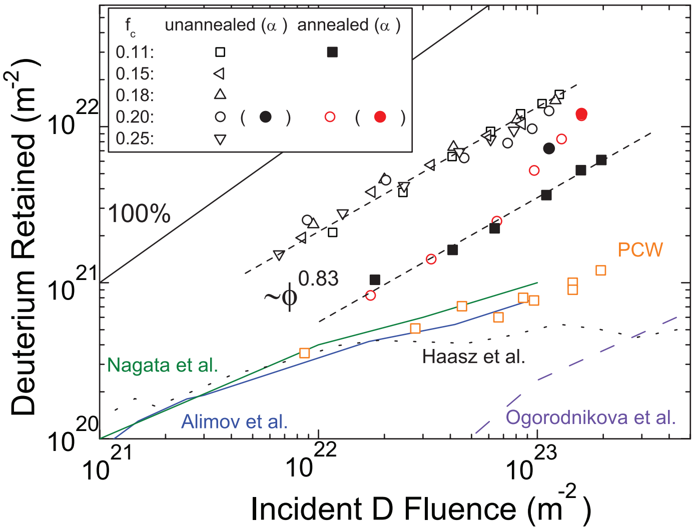

Figure 5.7: Total deuterium retention as function of incident D fluence for varying f_c's in the C deposition regime. Also plotted for the $f_c = 0.20$ case is the integrated D amount obtained from the α-spectrum of both annealed and unannealed specimens. For comparison, D retention results from ITER grade polycrystalline W (PCW) specimens (section 5.2) are plotted (orange squares) together with literature values for single crystal tungsten: 6 keV - Alimov et al. [145] (blue line) and 5 keV - Nagata et al. [180] (green line); and PCW: 1 keV - Haasz et al. [181] (dashed black line) and 0.2 keV - Ogorodnikova et al. [139] (dashed purple line).

The α-spectra measured at a scattering angle of 105° using 0.69 MeV D(^{3}He, ^{4}He)p reaction for $f_c = 0.20$ for an annealed and unannealed specimen following irradiation are shown in Fig. 5.6(a). The total fluence in the case of the annealed specimen was twice as high than the case of the unannealed specimen resulting in thicker C layer growth. The difference in C layer thickness results in the difference in width of the collected α-spectra as seen in Fig. 5.6(a). From these α-spectra, the D depth profile was determined using SIMNRA [158] in two steps: (1) First, the target layer structure (i.e. C layer thickness and areal density) was obtained by fitting the W leading edge of the 165° detector RBS spectrum. The total C areal density was compared against the proton peak integrals collected from the ^{12}C(^{3}He, p)^{14}N reaction to ensure that the fitted C depth profile gives the correct integral C areal density, and (2) using this target layer, the contribution of D was added keeping the C and W areal densities and ratios constant to fit the α-spectrum detected by the 105° detector. Once fitted, the corresponding total D areal density is calculated and compared against the D areal density measured from the 2.5 MeV D(^{3}He, p)^{4}He reaction. Assuming the atomic densities in the mixed material layer can be approximated by weighting the pure C and W densities with their atomic percentage, the α-spectrum can be plotted as a function of depth as seen in Figs. 5.6(b,c). Also plotted are the relative C and W concentration depth profiles with the numbers indicating the ratios of D/C, D/(C+W), or D/W in the given depth region. Outlined in magenta is the approximate boundary region of the C-W mixed material layer.

From Figs. 5.6(b,c), four regions of D trapping can be distinguished in both specimens: (1) At depths $< 100\,nm$, an unsaturated C layer is observed with a measured D/C ratio below 0.4, (2) From depths $> 100\,nm$ up to a depth where W concentration is observed, the measured D/C ratio is saturated at 0.4 (a value typically measured for H [178] and D [17, 179] ion irradiation of graphite at keV energies at RT), (3) At depths where the C-W mixed material layer is observed (outlined by magenta box), the measured D/(C+W) ratio is highest at 0.45-0.5, which is similar to the ratio measured from C-W dust prepared by D arc discharge [138], (4) At depths beyond the C-W mixed material layer, the measured D/W ratio is 0.02-0.1, which is a typical value of D trapping in bulk tungsten [17, 131]. From all the above observations, it can be concluded that the relative amount of D trapped is highest in the C-W mixed material layer, which is attributed to the synergistic effect of energetic ion-induced traps in W and D trapping with C in the C-W mixed material.

Published deuterium retention data in tungsten as a function of incident D fluence are plotted in Fig. 5.7 (Refs. [139, 145, 180, 181]), along with the corresponding D retention for various values of f_c in the C deposition regime. Also plotted for the case of $f_c = 0.20$, is the D retention in the C-W layer determined from the α-spectrum. D retention in ITER grade bulk W specimens measured in the continuous W erosion regime at $f_c = 0.07$ (further discussed in section 5.2) are plotted for comparison. There are four main observations in Fig. 5.7: (1) The total retained D amount from experiments are significantly higher than the published literature data for pure W. This indicates that the contribution from D trapped in the Ni substrate to the measured D amount cannot be neglected. It should be considered that in present experiments, the amount of implanted D is measured within minutes following irradiation, which may also contribute to the observed higher retention compared to literature data. Deuterium release from W following irradiation results in the reduction in the total D amount by up to $\approx 50\,\%$, depending on the time between irradiation and measurement [182]; (2) Comparison of the unannealed specimen against the annealed specimen at $f_c = 0.11$ indicates that the unannealed specimen retains $4\times$ as much D, but both specimens follow a fluence dependence of $\sim \phi^{0.83}$. D trapping in bulk W normally follow a fluence dependence of $\sim \phi^{0.45}$ [134] (also see experimental results for PCW-orange squares), which indicates that D is mainly trapped in the Ni substrate. The reduction in D amount is mainly due to the annealing of the Ni substrate, although the contribution from the reduced W film stress cannot be separated; (3) For $f_c = 0.20$, comparison of the retained D amount calculated from the α-spectrum indicates good agreement for the annealed specimen, but $\approx 40\%$ lower for the unannealed specimen. This is due to the thicker C layer formed on the annealed specimen ($\approx 400\,nm$) compared to the unannealed specimen ($\approx 200\,nm$) as seen earlier in Figs. 5.6(b,c). Consequently, in the case of the unannealed specimen, the $2.5\,MeV$ ^{3}He beam probes deeper regions where D has diffused and trapped in the Ni substrate and possibly also at the interlayer. From (2) and (3) it can be concluded that the D fraction trapped within the W-film cannot be separated from the Ni substrate from the measured total D retention amount during RT irradiation using both annealed and unannealed specimens; (4) Comparison of the annealed specimens but at different C fraction values of $f_c = 0.11$ and $f_c = 0.20$ show that for the $f_c = 0.20$ case, a change in slope at incident fluence of $F_D = 6.5 \times 10^{22}\,m^{-2}$ occurs, corresponding to $n_c = 0.7 \times 10^{22}\,m^{-2}$. This results from the fact that the C layer has reached a sufficient thickness which can trap all incident D within the growing C layer. The change in the slope is seen only for the higher f_c case is due to the increased rate of C layer growth, resulting in thicker C layer for a given incident D fluence.

In conclusion, the fraction of deuterium trapped in the W-films could not be clearly separated from the D amount trapped in the Ni substrate from the total D retention amount measured during simultaneous C-D irradiation at *RT* (Fig. 5.7). However, from the α-spectrum in Fig. 5.6, the relative amount of D trapped in the C-W mixed material layer was the maximum observed (>0.4). Such high concentration is typical of hydrogen trapping in carbon and is not observed in tungsten. Therefore at RT, deuterium trapping behavior in C-W mixed materials follow more closely the D trapping behavior in carbon. However, the contribution of the total trapped amount is still small when compared to the amount trapped in the C layer because the C-W mixed material layer is limited in depth (typically the C ion implantation range), while the C layer can grow indefinitely with the measured D/C ratio of 0.4 with fluence. At elevated temperatures where carbon diffusion into bulk W become significant, the C-W mixed material range will not be limited to the surface and therefore significant trapping of deuterium may occur. However, it will be shown in the next section that at elevated temperatures, the deuterium trapping behavior in the C-W mixed material follow the D trapping behavior in tungsten.

5.1.2 Elevated temperature

In the carbon deposition regime, it is clear that the incident D will initially interact with W, then a C-W mixed material, and finally C, with the formation of a thick enough C layer on the surface. Therefore, the C-W-D system should tend towards a C-D system with increasing fluence. It is well known that chemical sputtering processes increase with temperature for a C-D system as outlined in section 2.2 and the references therein. Also, in section 4.2.2, it was shown that C self-sputtering increases with temperature. Both effects will reduce the rate of C layer buildup with increasing temperature and the effects are quantified in the analysis below.

The implantation sputter curves for simultaneous irradiation at $f_{\mathrm{c}} = 0.20$ at *RT*, $670\,K$, $770\,K$, and $870\,K$ are plotted in Fig. 5.8(a) with TRIDYN calculations using the *SBEs* derived in section 4.2.2, and (b) with the phenomenological model developed in section 6. First, from Fig. 5.8(a), it is clear that TRIDYN calculations overestimate n_w at small n_c, resulting in the slight shift between TRIDYN curves and experimental data. The reason is that in TRIDYN calculations, $Y_w^c > 0.4$ for small n_c. It is noted that in the phenomenological model, with an upper limit of $Y_w^c = 0.4$ taken from the revised Bohdansky formula, this shift does not occur. Second, the slope, dn_w/dn_c, calculated by TRIDYN at $\alpha_T = 15°$, is in good agreement with the experimental data at $670\,K$ and $770\,K$. This demonstrates that the balance between C and W sputtering processes is correctly described by TRIDYN. However, in the $770\,K$ case, TRIDYN calculations predict the transition to zero W sputtering at $n_c \approx 0.3 \times 10^{22}\,m^{-2}$, in contrast to the experimental data where the transition occurs at larger n_c. This is attributed to the increased clustering of the C layer growth with increasing temperature which exposes the underlying W. To account for the deviation in experiments from the laterally uniform surface assumed in TRIDYN, the W sputtering yield which is dependent

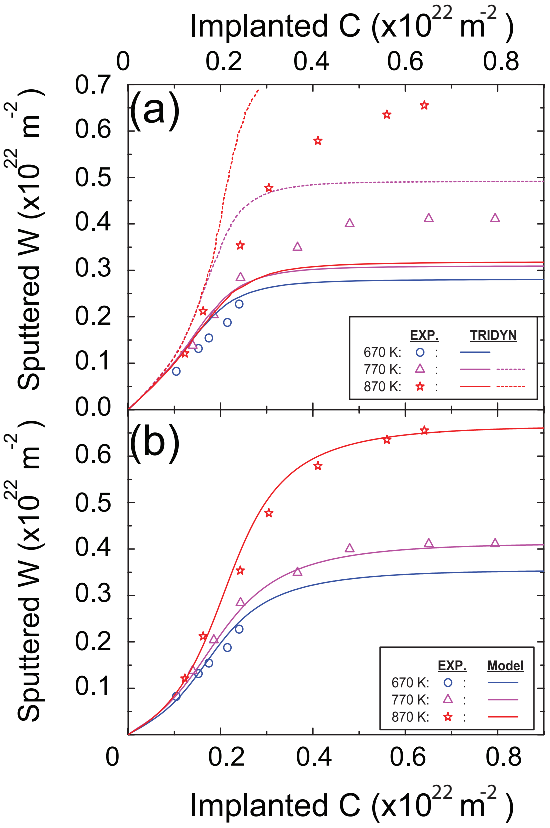

Figure 5.8: Comparison of experimental results for $f_{\mathrm{c}} = 0.20$ at increasing temperatures against: (a) TRIDYN calculations using *SBEs* derived in section 4.2.2, and (b) phenomenological model discussed in section 6. The dashed TRIDYN calculations correspond to $\alpha_T = 20°$.

on the C areal density was modified (details in section 6). The W sputter yield is approximated to be proportional to the surface concentration of W which is provided by TRIDYN calculations. Comparison to the phenomenological model predictions using this modified W sputtering yield show good agreement with the experimental data (see Fig. 5.8(b)). Therefore, the observed behavior is purely attributed to kinematic scattering processes, which leads to the question why chemical sputtering is not observed with the buildup of C layer. The answer lies in the thickness of the C layer deposited.

The thickness of the C layer can be estimated from the α-spectrum by taking the depth of the peak maximum of D as seen in Fig. 5.9, since this is a clear marker of the interface between the mixed material and the C layer. It should be noted that the D/C ratio in the C layer is significantly smaller than at *RT* with a maximum value of ≈ 0.05. From C-only irradiation as well as simultaneous irradiation (Fig. 5.8), the onset of temperature dependent effects was observed at implanted C areal density of $n_c \approx 0.1 \times 10^{22}\, m^{-2}$. Assuming further C implantation occurs within the growing C layer, the thickness of the C layer can be calculated from:

$$D = (n - \delta)\, \rho \tag{5.1}$$

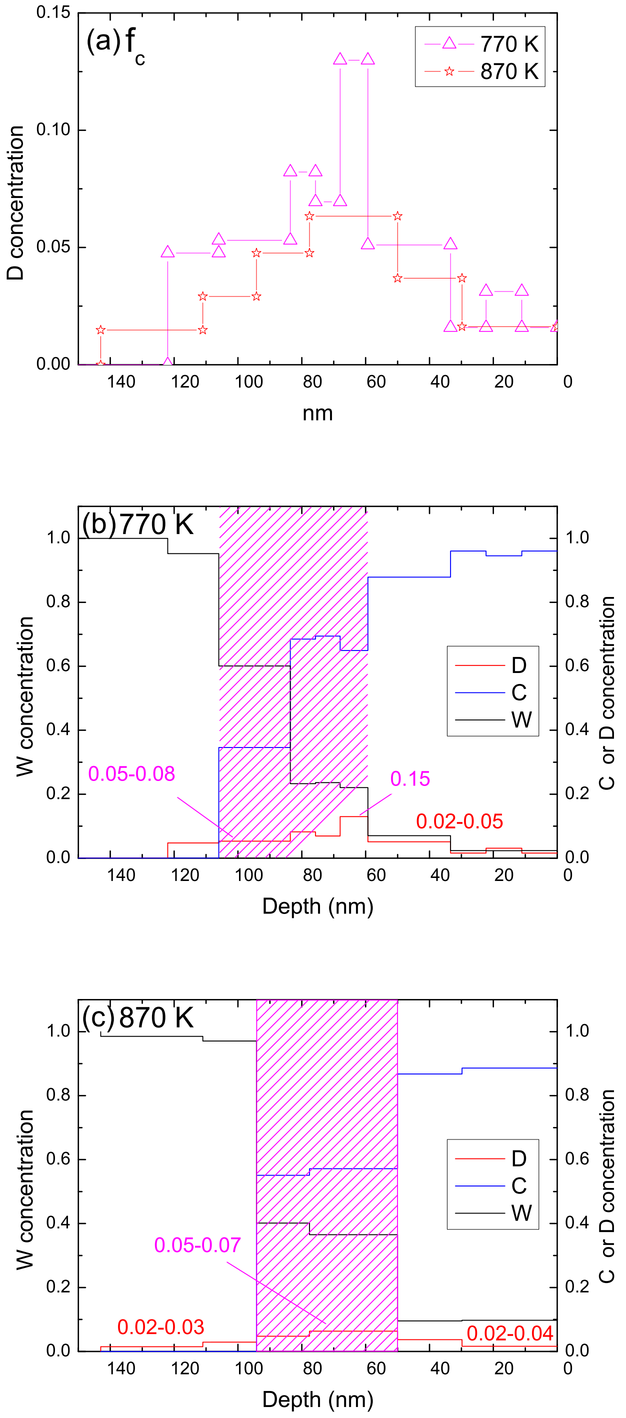

Figure 5.9: NRA α-spectrum measured at a scattering angle of 105° using the cross section of $0.69\,MeV$ D(^{3}He, ^{4}He)p reaction for $f_{\mathrm{c}} = 0.20$ for: (a) $670\,K$, and $770\,K$. Also, shown are the relative concentrations of D, C, and W as a function of depth for: (b) $770\,K$, and (c) $870\,K$ data. The numbers indicate the ratios of D/(C+W) and D/W at the indicated depth, while the C-W mixed material region is approximately highlighted by the hatched magenta box. .

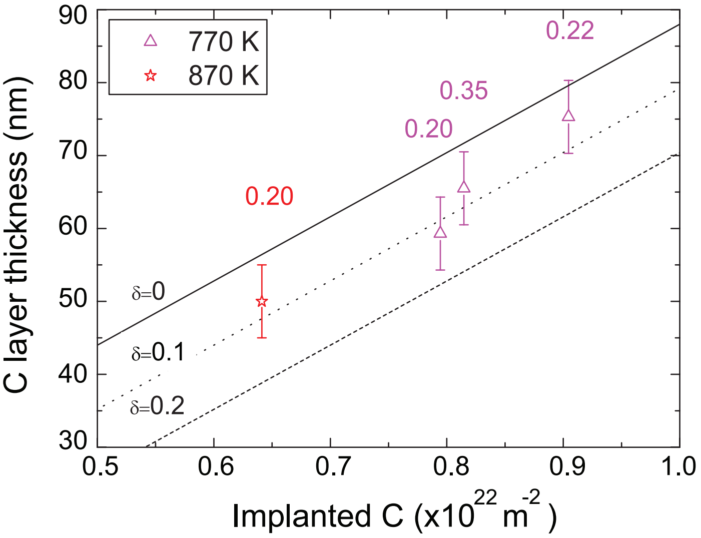

Figure 5.10: C layer thickness estimated by the maximum D peak depth in the α-spectrum for various f_{C}'s indicated by the colored numbers at 670 K and 770 K. Eqn. 5.1 is plotted for varying δ's.

where $\delta = 0.1 \times 10^{22}\, m^{-2}$ is the minimum C areal density required before the onset of C layer growth, and ρ is the density of pure graphite ($1.136 \times 10^{23}\, cm^{-3}$). Plotting both approximations for various f_c's at 670 K and 770 K and δ's yields Fig. 5.10. The error associated with the experimental data is taken to be the typical averaged surface roughness value, $R_q \approx 10\, nm$, observed in the W erosion regime, since this largely determines the interface topology where the mixed material layer is changing to a pure C layer. Shown also is the variation in δ corresponding to the upper and lower limits of the experimental error. The estimate of the C layer thickness from the α-spectra and the thickness calculated by Eqn. 5.1 are in agreement within the error bars of measurement. The carbon layer thicknesses vary from $45 - 75\, nm$ depending on the C flux available and temperature for each experiment. For example, the enhanced C self-sputtering yields at 870 K result in thinner C layers for equal incident total C fluences (compare the two cases of $f_c = 0.20$ at 770 K and 870 K in Fig. 5.10).

Hence, given the available carbon flux in experiments, it was only possible to produce C layers with thicknesses $< 80\, nm$ during simultaneous deuterium and carbon ion irradiation due to the enhanced C self-sputtering at 670 K and 770 K. Considering the mean ion range calculated by TRIM.SP [84] of 3 keV D ions in pure C is $\approx 60\, nm$, it is clear that even at the maximum C layer thickness (i.e. end of experiment), most of the D is still stopped at the mixed material layer and beyond. Since formation of volatile molecules at chemical sputtering of C by energetic D ions is understood to occur only at the end of the D range, it is reasonable why chemical sputtering effects was not observed at 670 K and 770 K. In principal, a maximum chemical sputtering yield of $Y_{chem} \approx 0.015$ would be compatible with experiments if included in the 770 K case, but this effect is certainly within experimental error, and therefore its inclusion is not justified.

5.1.3 Summary

In the carbon deposition regime, the dynamics of W sputtering and C layer growth can be well modeled accurately by TRIDYN at RT. Using the additional adapted model that treats W sputtering proportional to the W surface concentration, a good match is also found at elevated temperatures. Therefore, one can conclude that the main governing process is kinematic scattering of projectile and target atoms with the increase in C self-sputtering being the dominant effect at elevated temperatures. Possible effects of chemical sputtering of the deposited C layer were found to be smaller than the uncertainty, due to the fact that the available C flux allows only to produce C layers with thicknesses $< 80\,nm$ from the enhanced C self-sputtering. Therefore, most of the D was decelerated to the low energies required to form volatile molecules only in the region of the C-W mixed material or beyond.

Deuterium retention at RT was observed to be higher than reported literature results due to contributions of D trapped in the Ni substrate that could not be separated from the D amount trapped in the W film. However from the α-spectra, the highest relative concentration of D trapping was found in the mixed material layer with a D/(C+W) ratio greater than 0.4 observed in the co-deposited C layer at RT. At elevated temperatures this trend is also observed with D/(C+W) ratio greater than 0.05 observed in the co-deposited layer.

5.2 Tungsten erosion regime

In the tungsten (W) erosion regime, the surface remains a constant mixture of C-W-D due to the equilibrium of implantation and sputtering processes. Significant deviations are observed between experimental results and TRIDYN calculations for $f_{\mathrm{c}} \leq 0.07$ (Fig. 5.1). A magnified view of the low fluence range is presented in Fig. 5.11 to reveal the details of the discrepancies.

One can see that the TRIDYN calculations predict an increase of the steady state C areal density, n^{c}_{ss} with increasing f_{c}, due to the shift of the balance between C implantation and erosion flux. At higher incident C fraction, there has to be a higher C fraction in the mixed layer to obtain a balanced C erosion flux. In contrast, the experimental results indicate a constant $n^{c}_{ss} \approx 0.065 \times 10^{22}\,m^{-2}$ independent of f_{c}.

As discussed earlier in section 4, the carbon sputtering efficiency can only increase from an increase in surface roughness, C self-sputtering, or changes to the carbon depth profile from diffusion or segregation processes leading to carbon enrichment at the surface. At RT, increase in C self-sputtering and changes to the depth profile from diffusion and segregation effects can be ruled out. Therefore, the only remaining sputtering related mechanism which could lead to an increase of C erosion flux despite a constant C fraction at the surface is surface roughness. To determine the potential surface roughness contribution, AFM measurements were performed both on and off the irradiated area, and are summarized in Table 5.1.

The results show no significant change of surface roughness at the irradiated areas for $0.03 \leq f_{\mathrm{c}} \leq 0.07$. Therefore surface roughness effects cannot explain the observed behavior. With all sputtering related effects ruled out, there still remains the alternative chemically induced release of carbon from the C-W-D mixed material under

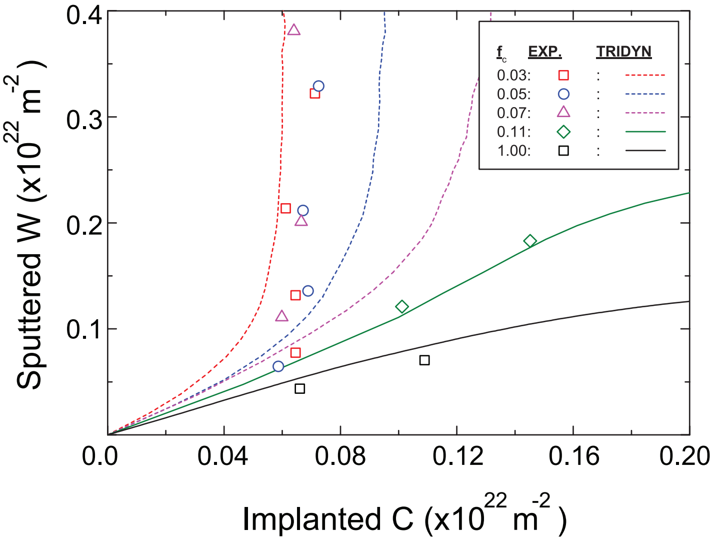

Figure 5.11: Comparison of experimental results for varying f_c in the W sputtering regime with TRIDYN calculations. The steady state C areal density is constant at $n^c_{ss} \approx 0.065 \times 10^{22}\, m^{-2}$.

f_c	0.03	0.05	0.07	0.11(a)	0.11(b)
Off $[nm]$	5	5	5	15.	5
On $[nm]$	10	9	14.	17.	-

Table 5.1: AFM measurements of irradiated specimens for $f_\mathrm{c} \leq 0.11$ presented in Fig. 5.11 for both on- and off- the irradiated areas. The numbers indicate the root mean square surface roughness values, R_q in nm.

simultaneous irradiation. To determine whether the observed behavior is truly due to chemical processes, experiments were performed at elevated temperatures and with lower D energies, which will be discussed in some detail in section 5.2.2. But first, this requires discussion of the mechanism of tungsten sputtering under simultaneous irradiation.

5.2.1 Tungsten sputtering

As a first approximation, it is assumed that the total tungsten (W) areal density sputtered, n_w, is proportional to the linear combination of the amount of W sputtered by C and D individually:

$$n_w \propto n^c_w + n^D_w \tag{5.2}$$

where n^c_w and n^D_w can be expressed in terms of the W sputter yields of pure W irradiated by C-only, Y^c_w, and D-only, Y^D_w, and their respective fluences F_C and F_D:

$$n_w^c = Y_w^c \, F_C$$

$$n_w^D = Y_w^D \, F_D$$

With the following expressions for the total fluence, F_T, and C fraction in the beam, f_c, respectively:

$$F_{\mathrm{T}} = F_C + F_D$$

$$f_{\mathrm{c}} = \frac{F_{\mathrm{C}}}{F_{\mathrm{T}}}$$

the expressions for n_w^c and n_w^D can be expanded to:

$$n_w^c = Y_w^c \, F_{\mathrm{C}} = Y_w^c \, f_{\mathrm{c}} \, F_{\mathrm{T}}$$

$$n_w^D = Y_w^D \, F_D = Y_w^D \, (1 - f_{\mathrm{c}}) \, F_{\mathrm{T}}$$

with the above expressions, Eqn. 5.2 becomes:

$$n_w \propto Y_w^c \, f_{\mathrm{c}} \, F_{\mathrm{T}} + Y_w^D \, (1 - f_{\mathrm{c}}) \, F_{\mathrm{T}}$$

$$\frac{n_w}{F_{\mathrm{T}}} \propto Y_w^c \, f_{\mathrm{c}} + Y_w^D \, (1 - f_{\mathrm{c}})$$

$$Y_w = \frac{n_w}{F_{\mathrm{T}}} = K_{f_c} \, \left[Y_w^c \, f_{\mathrm{c}} + Y_w^D \, (1 - f_{\mathrm{c}}) \right] \tag{5.3}$$

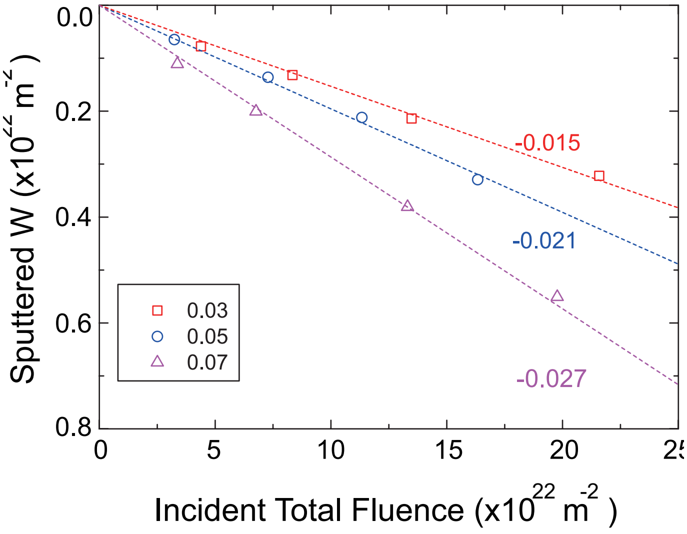

Figure 5.12: The amount of W sputtered as a function of total incident fluence for $f_c \leq 0.07$. The numbers indicate the slope of the linear fit, which is the total W sputter yield, Y_w.

Eqn. 5.3 simply states that the total W sputter yield is proportional by a factor K_{f_c} to the weighted W sputter yields of pure W by C- or D- only irradiation. The Y_w^c and Y_w^D values can be obtained analytically from the revised Bohdansky formula or experimental data as summarized in Table 2.1 in section 2.1.3. Y_w is the slope obtained from experimental results by plotting the change in W areal density against the total incident fluence as seen in Fig. 5.12, while f_c is determined from the beam profiles measured by the BVS system.

The resulting values for K_{f_c} are summarized in Table 5.2 below. The D fluence is an order of magnitude larger than the C fluence and largely determines the error in determining the slope. However, in all cases, the D flux did not vary by more than a few percent over the entire fluence range and was also uniform across the entire analyzed area. Therefore, the error in the total fluence measurements can be neglected.

f_c	Y_w	K_{f_c}	S_w
0.03	0.015	0.69	0.65
0.05	0.021	0.71	0.64
0.07	0.027	0.72	0.70

Table 5.2: Summary of the experimentally derived W sputter yield, Y_w, and the resulting proportionality factor, K_{f_c} along with the W surface concentration, S_w, measured by ex-situ XPS analysis following irradiation. S_w was determined by first normalizing the tungsten XPS peak in Fig.5.13(a) by its known sensitivity factor, then by taking the quotient of the normalized area against the total sum of the W, C, and O peaks.

Comparison to tungsten surface concentration measurements by XPS shown in Fig. 5.13(a) show good agreement with K_{f_c}. From these results, it is inferred that W sputtering under simultaneous irradiation can be described by a sum of the weighted Y_w^c

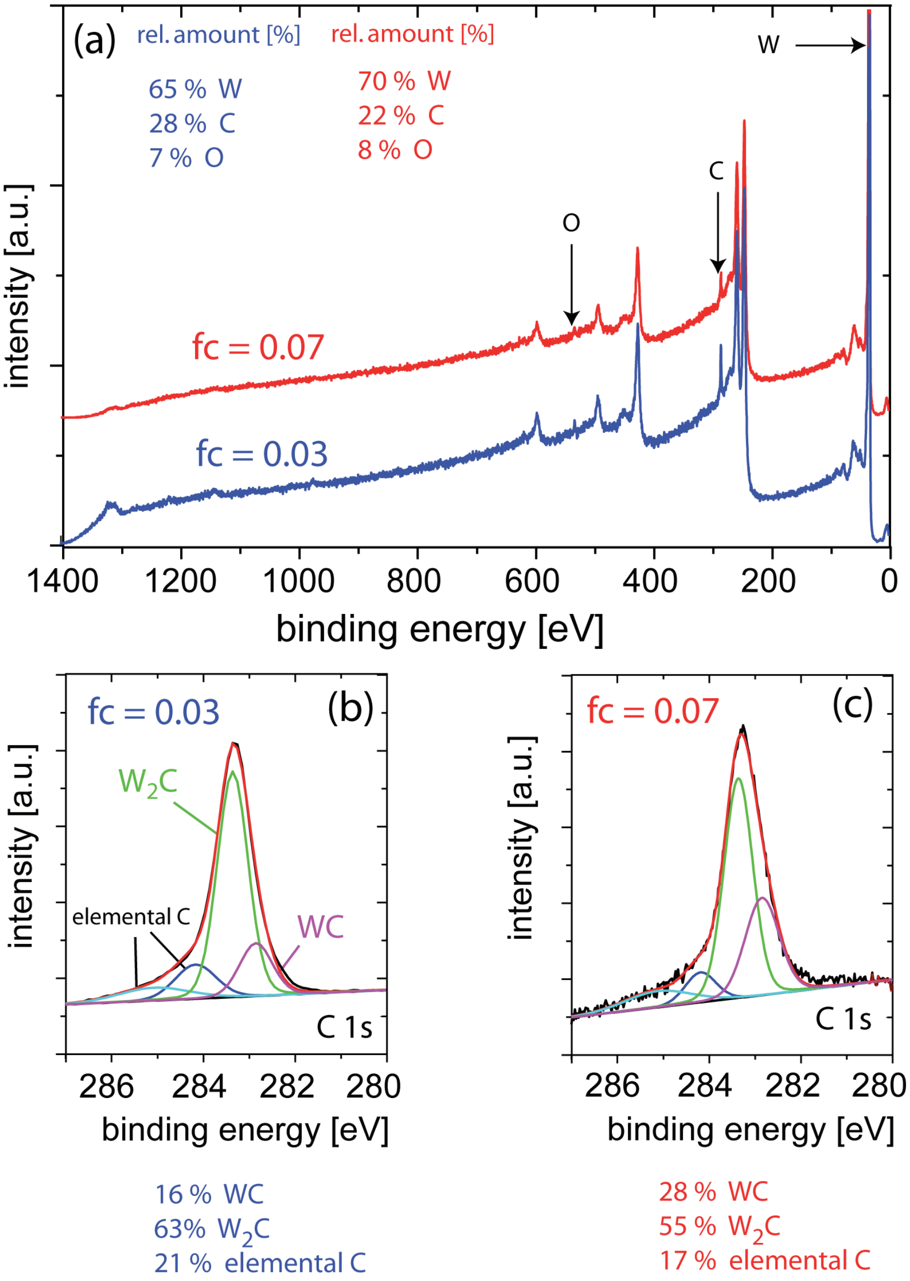

Figure 5.13: Ex-situ XPS analysis following irradiation of the specimens with two different f_c's to determine: (a) the surface C and W elemental compositions, and (b,c) corresponding chemical binding information . The relative peak areas in (a) do not directly reflect the relative amounts due to the difference in photoionisation cross section.

and Y_w^D yields, that is proportional to the surface concentration of tungsten, S_w. Furthermore, comparison to the TRIDYN simulation case for the experimentally observed steady state C areal density $n_{ss}^c \approx 0.065 \times 10^{22}\, m^{-2}$ (see Fig. 4.6) show excellent agreement with $S_w = 0.7$ as in the experiments. From this we conclude that for a given n_c, the corresponding TRIDYN depth profile and S_w can approximate the experimental C depth profile and W surface concentration, which are experimentally unavailable.

The chemical structure of the surface according to the XPS results shown in Figs. 5.13(b,c) is characterized by carbon being mostly in carbide form with an elemental C fraction $< 20\%$. Carbon films deposited on W substrates show a stepwise carbide formation from W_2C to WC when heated, but the carbonization process does not start until $T > 870\, K$ [183]. Therefore, carbide formation in this case occurs due to the mixing induced by energetic ion irradiation [184] in the mixed material layer. Similar concentrations of 70% W and 30% C is observed in the interlayer between deposited C and the W substrate in plasma experiments in PISCES [185]. If one takes into account that for dense, nonporous materials, the chemical sputtering process is generally surface limited, the carbonization of the mixed material C-W-D surface can explain the thresholding effect of n_{ss}^c. However, it will be shown in section 5.2.2 that the experimental results cannot be interpreted fully by assuming the carbon loss is only from the sputtering of weakly bound hydrocarbons at the surface.

5.2.2 Chemical sputtering of C-W mixed material

The significant discrepancy between TRIDYN simulations and experimental results for tungsten erosion at RT, which was preliminarily attributed to chemical sputtering effect can be examined quantitatively by fitting the experimental data with the phenomenological model (section 6). The comparison between the model and the fitting to the experimental data to obtain the chemical sputtering yield, as well as the amount of D fraction retained is discussed below.

A clear indicator of a chemical process is the normally observed corresponding temperature dependence. Therefore, at $f_c = 0.07$ where the largest discrepancy between TRIDYN and RT experimental results was observed, specimens were irradiated at elevated temperature. In Fig. 5.14, the results of $f_{\mathrm{c}} = 0.07$ irradiation of W-film specimens at increasing temperature are shown against RT results. Also shown is the n_{ss}^c range observed for ITER grade bulk tungsten specimens. Since these specimens were not tungsten films as the standard specimens used in this study, the integrated W sputtered amount could not be determined using RBS.

Fig. 5.14 shows that the lowest n_{ss}^c is always observed at RT. At elevated temperatures, n_{ss}^c remains constant within experimental error and is independent of temperature with good agreement to TRIDYN calculations using the $SBEs$ derived in section 4.2.2. However, compared to RT results, an increase in n_{ss}^c is observed, in accordance to the assumed chemical sputtering process, which decreases with increasing temperature. This behavior is opposite to that of chemical sputtering of pure carbon materials. Furthermore, comparison of n_w against the total fluence for RT and $770\, K$ as plotted in Fig. 5.15, indicates that there is no significant difference in the total W sputter yield. This indicates that the C loss at RT cannot be due to increased W sputtering, which could result in increased C loss by an increased rate of surface recession and

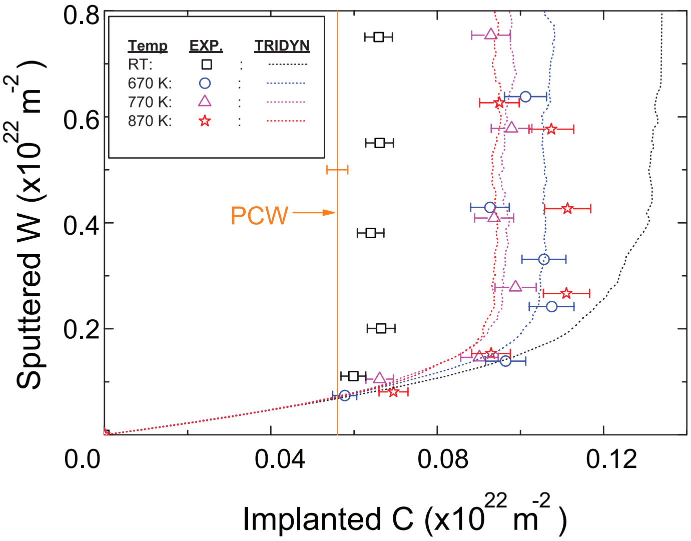

Figure 5.14: Comparison of C implantation and W sputtering behavior for $f_c = 0.07$ at different temperatures compared against TRIDYN calculations using the *SBEs* derived in section 4.2.2. Also included is the range of the C areal density observed for ITER grade PCW specimens irradiated at *RT* outlined in orange.

corresponding changes in n_{ss}^{c}. The constant W sputter yield indicates also that the surface composition is the same in both cases. From this one can infer that the C loss must arise from within the C-W mixed material layer.

Combining all these observations, one can develop an interpretation based on the model of chemical sputtering [117], where energetic ions break C-C bonds within their penetration range and the resulting dangling bonds are passivated by the hydrogen atoms. Consecutive bond breaking and passivation lead to the formation of volatile hydrocarbons at and below the surface which diffuse to the surface and desorb. This model is based on experiments with irradiation of an amorphous hydrogenated layer with atomic hydrogen provided by a radical source [117]. This model can be applied to the present results, if one assumes that the D trapped within the mixed material layer can passivate the broken bonds caused by both energetic D and C ions. Hydrogen trapping in W is often interpreted by a model where hydrogen atoms become trapped at vacancies or adsorbed on the inner walls of voids created during irradiation [186]. In addition, D trapped in tungsten carbides are only observed to release as D atoms [128, 133, 145]. Therefore, it is plausible to assume at this point that the trapped D can also passivate the broken C-C or C-W bonds created during ion irradiation. However, from the fact that the surface is mostly in carbide form, broken C-W bonds seem unlikely to contribute to the chemical sputtering process, and that only the C-C bonds are affected. Confirmation of this hypothesis will, however, require detailed molecular dynamic simulations (MD). Experimental signs of chemical sputtering at *RT* is observed from methane release by Bizyukov et al. [187] during simultaneous C-D irradiation of PCW in the range of $\frac{CD_4}{D} \approx 0.01$, and $\frac{CD_4}{D} \approx 0.02$ by Wang et al. [126] in tungsten carbide. Interestingly, the methane release is only observed following an initial D accumulation in the implanted near-surface layer [126].

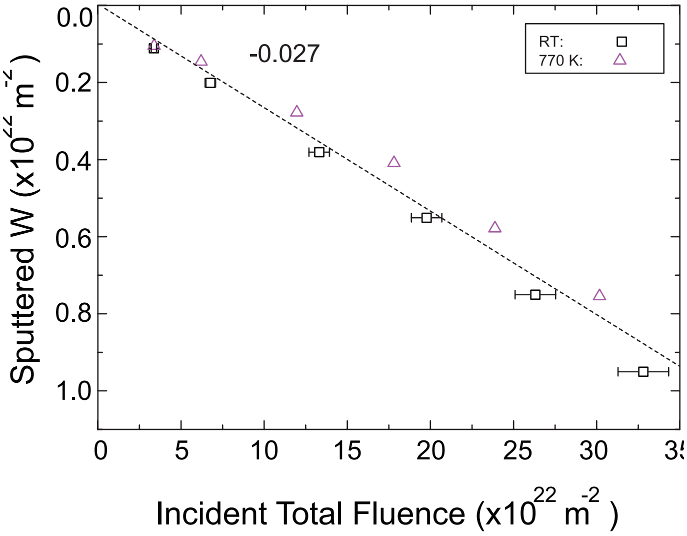

Figure 5.15: Comparison of the W sputtering as a function of incident total fluence. The number indicates the slope and yields the total W sputter yield.

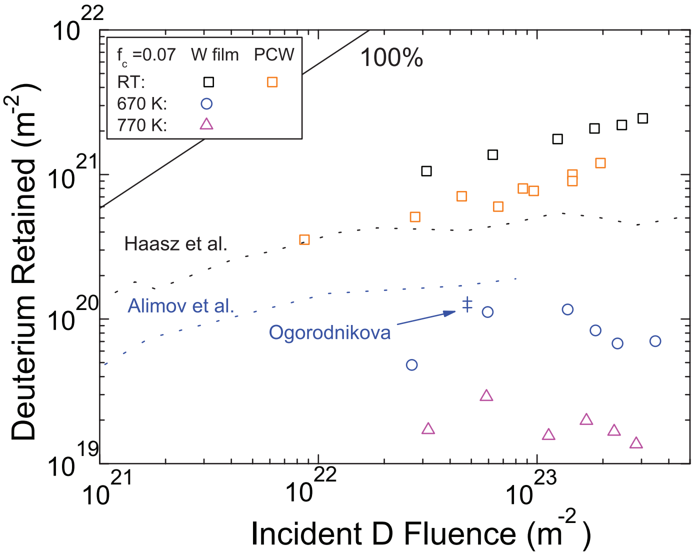

Figure 5.16: Total D retention as function of incident D fluence for $f_c = 0.07$ for W-film specimens at various specimen temperatures. Also plotted are D retention results from ITER grade polycrystalline tungsten specimen (orange squares) irradiated at RT. The published literature values for tungsten single crystal: $6\,keV$ at $650\,K$ - Alimov et al. [145] (dashed blue line) and PCW: $1\,keV$ at RT - Haasz et al. [181] (dashed black line) with unpublished values at $3.33\,keV$ at $500\,K$ - O. Ogorodnikova (blue cross) are also plotted for comparison.

In Fig. 5.16, the total deuterium retention amount is plotted as a function of incident D fluence for various temperatures. The amount of retained D decreases by an order of magnitude if the specimen temperature is increased from $670\,K$ to $770\,K$. At $870\,K$, D retention was below the sensitivity limit of the NRA measurement of 10^{15} at/cm^2. Consequently, with increasing temperature, the available amount of D that is able to passivate the broken C-C bonds decrease, which results in the observed decrease of chemical sputtering with increasing temperature. TDS spectra show two distinct regions of D release in the range $300 - 700\,K$ and $900 - 1100\,K$ from D irradiated tungsten carbides [126, 135, 136]. However, there is no clear interpretation of the exact nature of these traps, although the peak found in the high temperature range is normally interpreted to be D trapped at carbon sites. Irradiation at $T > 673\,K$, results in negligible D trapping in the lower temperature region [135], and therefore it appears that the D trapped at the lower temperature regions are responsible for the passivation of C-C bonds.

To illustrate the projectile energy dependence in the chemical sputtering process, Eqn. 5.4 is introduced below for the case of an a-C:H layer simultaneously bombarded by atomic H and H ions [117]:

$$Y_{chem}(E)\,\alpha \int y(x,E)p_{pass}(x)dx \tag{5.4}$$

where $y(x, E)$ denotes the number of bond breaking events per ion in an interval of thickness dx, and $p_{pass}(x)$ the probability of passivation of a broken bond by atomic H. For simultaneous irradiation, $p_{pass}(x)$ can be approximated by the D concentration profile, and $y(x, E)$ by carbon displacement yields of D and C ions, yielding:

$$Y_{chem}\,\alpha \int y_{C/D}(x, E_C, E_D, t)y_D(x, E_D, t)dx \tag{5.5}$$

The main difficulty in applying Eqn. 5.5 to develop an analytical model for Y_{chem} is the experimentally inaccessible $y_{C/D}(x, E_C, E_D, t)$ function. First, it is unknown whether bond breaking events by C or D ions, or bond breaking by both ions, result in passivation. Only molecular dynamics studies can elucidate the correct mechanism. Second, in the case of simultaneous C-D irradiation of W, the C depth profile is fluence dependent in the C layer growth regime, and in the W sputtering rate in the W erosion regime. This is in contrast to the known C distribution in the a-C:H layer used in Ref. [117]. Consequently, to apply the method used in Ref. [117] of approximating the bond breaking events by the C displacement yields calculated by TRIM [188] will require information on the evolving C depth profiles. The C depth profiles can be calculated from TRIDYN simulations, or experimentally measured by fitting the leading edge of the tungsten RBS spectra. However, in practice, the RBS spectra yields poor depth resolution within the C ion range ($\approx 30\,nm$) to accurately resolve the implanted C depth profile. A further complication arises from the fact that the bonding of the

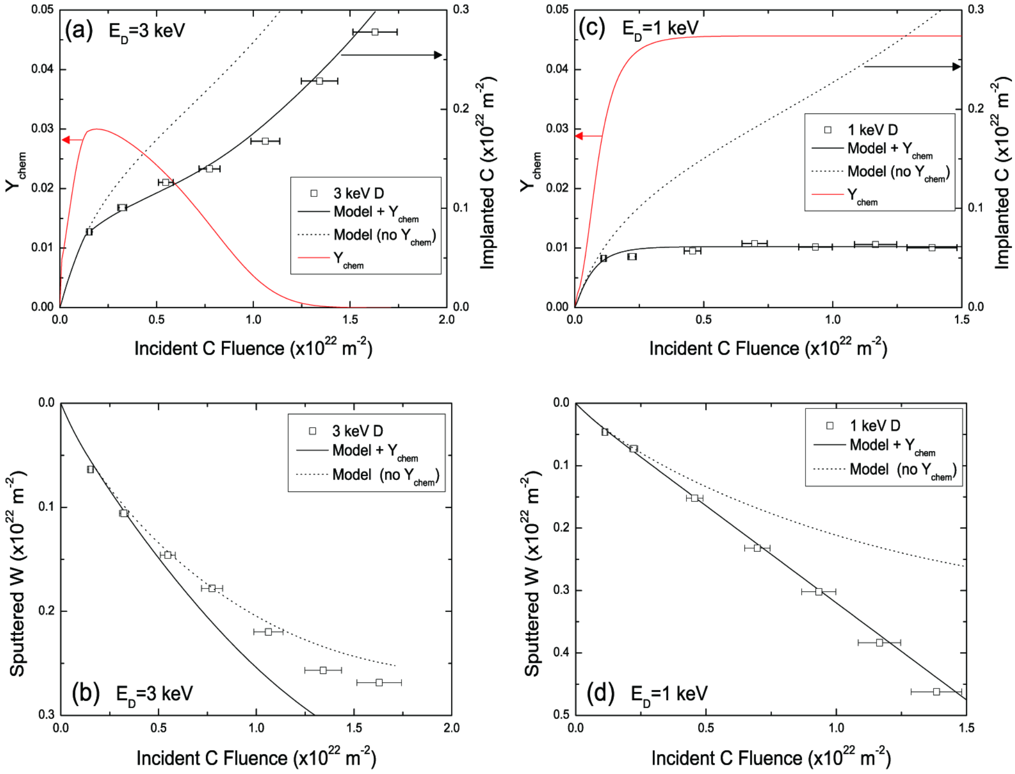

Figure 5.17: Comparison of C implantation and W sputtering behavior for: (a,b) $E_D = 3\,keV$, and (c,d) $E_D = 1\,keV$ at $f_c = 0.11$ plotted with the model and the fitted Y_{chem} component.

implanted C varies with depth from the formation of tungsten carbides and C-C clusters dependent on the local C concentration. This important physical state of the C bonding must be included in the model and measured experimentally. Third, the D depth profile is required to approximate the passivation probability function $y_D(x, E_D, t)$, and can be experimentally measured from the α-spectrum using NRA. However, a decrease in energy of the ^{3}He analysis beam is required from $2.5\,MeV$ to $0.69\,MeV$ to sufficiently separate the α-spectrum from the tungsten RBS peak. The decrease in energy results in a large decrease in beam current, and requires extended analysis time ($> 1\,h$) to collect sufficient statistics of the D depth profile. This additional time requirement makes it difficult to reach steady state fluences given the available fluxes in present experiments. In addition, the focusing of the analysis beam following the change in ^{3}He energy shifts the beam, in some cases by more than $2\,mm$, resulting in analysis of a totally different irradiated area. Therefore, calibration of the beam spot is required using the BVS following each change in energy from $2.5\,MeV$ to $0.69\,MeV$ and from $0.69\,MeV$ to $2.5\,MeV$. These calibration steps place additional time constraints on the experiment which could not be reasonably met in the present work.

In view of these experimental limitations and complications, only a qualitative description of the chemical sputtering process is provided based on experimental results obtained by lowering the incident D energy. It should be noted that the reduction of the incident D energy resulted in extremely low D fluxes, and as a result, experiments with low f_c's in most cases were not possible because the fluences required to reach steady state could not be reached.

The carbon implantation and tungsten sputtering behavior at $f_c = 0.11$ is shown for $E_D = 3\,keV$ and $E_D = 1\,keV$ D ions in Fig. 5.17, along with the Y_{chem} component required to match the model and experimental data. First by comparing Figs. 5.17(a-c), it can be seen that a larger reduction in n_c is observed with increasing C fluence by decreasing the D energy from $E_D = 3 \rightarrow 1\,keV$. This reduction can actually not entirely be attributed to the chemical erosion component, since Y_c^D also increases from $E_D = 3 \rightarrow 1\,keV$. This can be seen by the decrease of the slope of the C growth curve if one omits the Y_{chem} component in the model (dotted lines) as shown in Figs. 5.17(a,b). As the model includes the energy dependence of Y_c^D, one can conclude from the fitted Y_{chem} contribution, shown in red, that Y_{chem} clearly increases if the D energy is lowered from $E_D = 3 \rightarrow 1\,keV$. In fact, at $E_D = 1\,keV$, the chemical sputtering even results in the system to switch from continuous C layer growth to the steady state W erosion regime.

Qualitatively, the increase in chemical sputtering by reduction of the incident D energy can be illustrated by comparing the ranges of the D ions at $n_c = 0.06 \times 10^{22}\,m^{-2}$ as seen in Fig. 5.18, where the carbon concentration depth profile calculated by TRIDYN is plotted together with the D ion ranges. Fig. 5.18 shows that at $E_D = 1\,keV$, a larger fraction of D will be stopped in the mixed material layer compared to the case of $E_D = 3\,keV$. This result confirms the previous hypothesis that the reduction in D energy increases the chemical sputtering yield by increasing the relative D amount trapped in the mixed material layer that can passivate the broken C-C bonds. Furthermore, Fig. 5.17(a) shows that with increasing C fluence, Y_{chem} decreases, in contrast to Fig. 5.17(b), where Y_{chem} is constant. This is because at $E_D = 3\,keV$, the balance between the erosion and implantation of carbon leads to C layer formation while at $E_D = 1\,keV$, the system is, as noted before, in the W erosion regime. With the onset of C layer growth, the dynamics of chemical sputtering will change since both C and D ions lose energy in the developing C layer, altering first the amount of C bond breaking events and secondly the D ion range. This effect is more pronounced for C implantation and W sputtering at $f_c = 0.23$ as seen in Fig. 5.19 at three different D energies.

First, aside from the $E_D = 3\,keV$ case (herein referenced as case (c)), the trend of increasing and decreasing chemical sputter yield is observed much like in Fig. 5.17(a). However, the nearly constant value of Y_{chem} obtained for case (c) contradicts the earlier observation in Fig. 5.17(a). The only difference for case (c) compared with the other cases was the increase in C flux (2×). From this, one can infer that the chemical sputtering process in C-W mixed material may also depend on the C flux. Comparison of the maximum chemical yield observed at $E_D = 3\,keV$ for $f_c = 0.11$ and $f_c = 0.23$ respectively, yields $Y_{chem} \approx 0.03 - 0.04$, indicating a threshold to the maximum density of damage sites available for chemical sputtering. Therefore, assuming the probability of passivation by incident or trapped D remains constant (due to fixed D range), a higher C flux keeps the damage sites active, which implies that the C ions are primarily responsible for the bond breaking events. Lowering the D energy from $E_D = 1 \rightarrow 0.53\,keV$ results in an increase of the chemical yield to $Y_{chem} \approx 0.08 - 0.09$. Following the discussion of the case of $f_c = 0.07$, this is explained by the closer overlap of the D ion range with the mixed material layer and the corresponding increase of the passivation probability for an active site. Aside from case (c), Y_{chem} becomes effectively

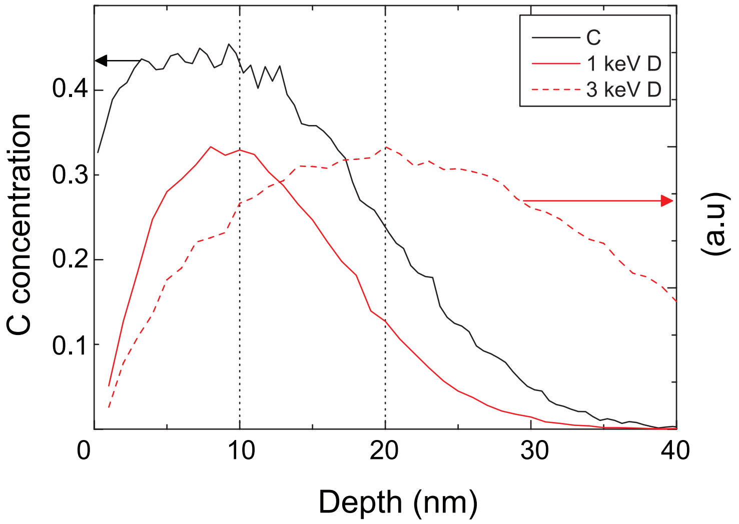

Figure 5.18: Comparison of the normalized D ranges calculated with TRIM [188] for $E_D = 3\,keV$ and $E_D = 1\,keV$ in pure W. The C depth profile is taken from TRIDYN simulations at $n_c = 0.06 \times 10^{22}\,m^{-2}$ and corresponds to an absolute scale. The dotted black lines indicate the mean ion ranges.

zero for $n_c > 0.2 \times 10^{22}\,m^{-2}$, corresponding to a C layer thickness of $\approx 10\,nm$ (see Fig. 5.10). As this thickness is not significant in terms of its effect on the incident ion ranges, the rather sharp decline can only be explained by a barrier action of the layer leading to a steep decrease of the escape probability for out-diffusing hydrocarbon molecules. This is probably due to the corresponding changes of surface composition, but again molecular dynamics simulations will be needed to validate this hypothesis. The large deviation between experimental results and the model prediction with Y_{chem} in Fig. 5.19(f) may indicate the effects of out-diffusing hydrocarbon molecules that trap at the surface, resulting in a decrease in W surface coverage and corresponding decrease in W sputtering. Fig. 5.19(b) shows that the C loss due to Y_{chem} is not from surface depletion, since that would lead to a corresponding change of the slope of the W sputtering curve which is not observed.

At $670\,K$, simultaneous irradiation at low D energies does not show contribution of chemical effects and can be fully described by kinematics alone as seen in Fig. 5.20. The corresponding D retention results are independent of incident D ion energies as seen in Fig. 5.21. Again, the reduction in D retention compared to RT retention fractions infers a negligible chemical sputtering contribution at $670\,K$, confirming the results of simultaneous deuterium and carbon ion irradiation experiments using $E_D = 3\,keV$ D ions as previously shown in Fig. 5.14. In contrast, a pronounced energy dependence of the total D retention is observed at RT. Since all specimens were unannealed, a possible substrate contribution cannot be entirely excluded. However, the clear decrease of D retention with decreasing D energy can be well explained by the decreasing defect creation rate, while for $670\,K$ results, one can conclude that either defect creation by D is negligible or that defects are annealing out at a rate greater than the creation rate. Therefore, the decrease in D retention observed at RT results from a combination of decreased defect creation and increased D loss from the chemical sputtering processes.

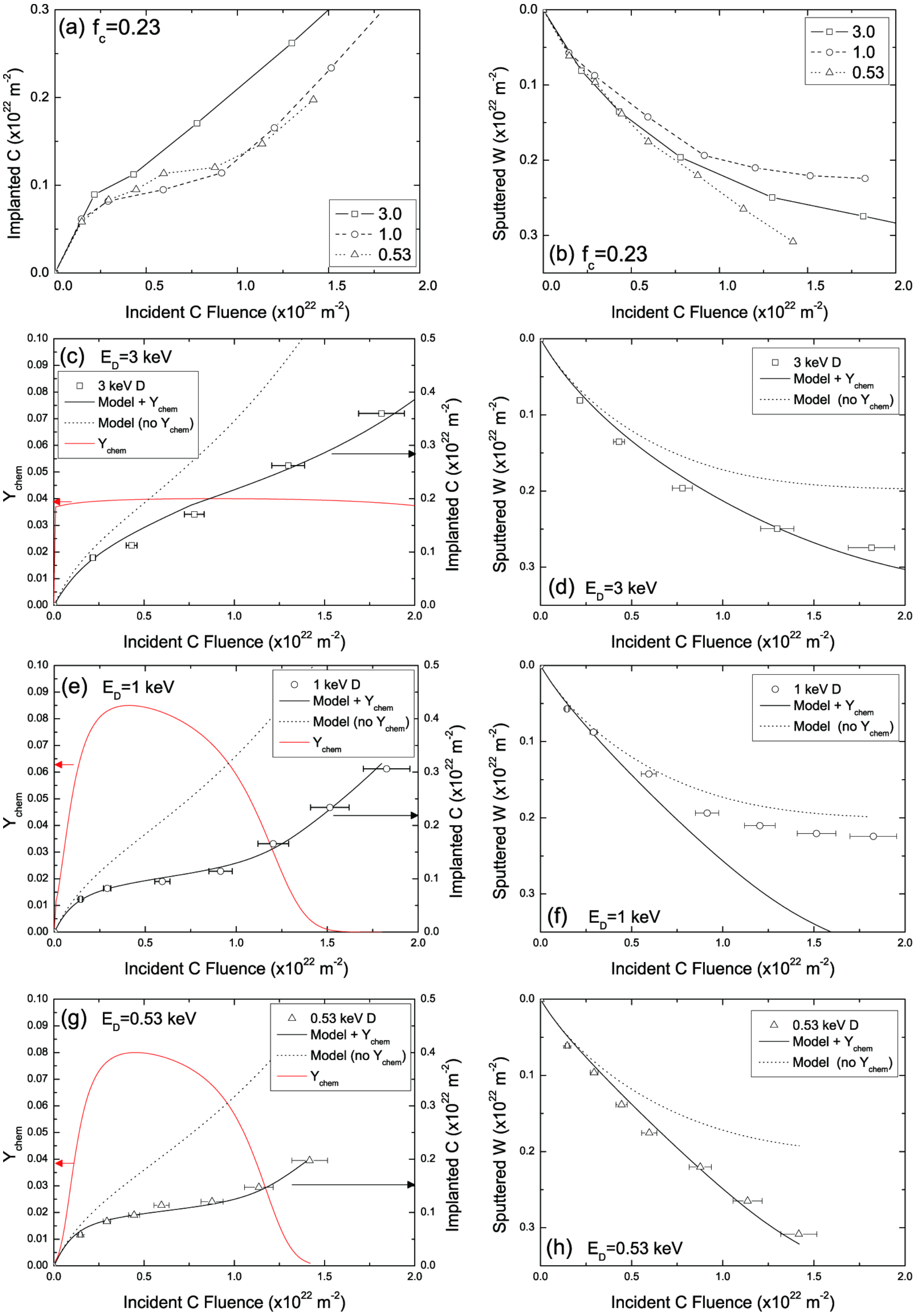

Figure 5.19: Comparison of: (a) C implantation, and (b) W sputtering behavior as a function of incident C fluence for varying incident D energies: (c,d) $E_D = 3\,keV$, (e,f) $E_D = 1\,keV$, and (g,h) $E_D = 0.53\,keV$ at $f_c = 0.23$ plotted with model predictions including and excluding the Y_{chem} component respectively. Also shown is the fitted Y_{chem} component in red.

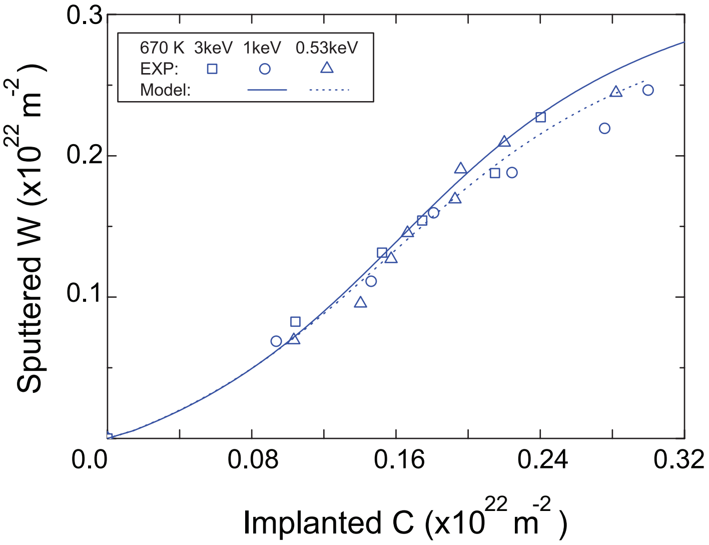

Figure 5.20: Comparison of C implantation and W sputtering behavior for $f_c = 0.23$ at $670\,K$ for varying incident D energies. Shown also are the results calculated by the model without any Y_{chem} component.

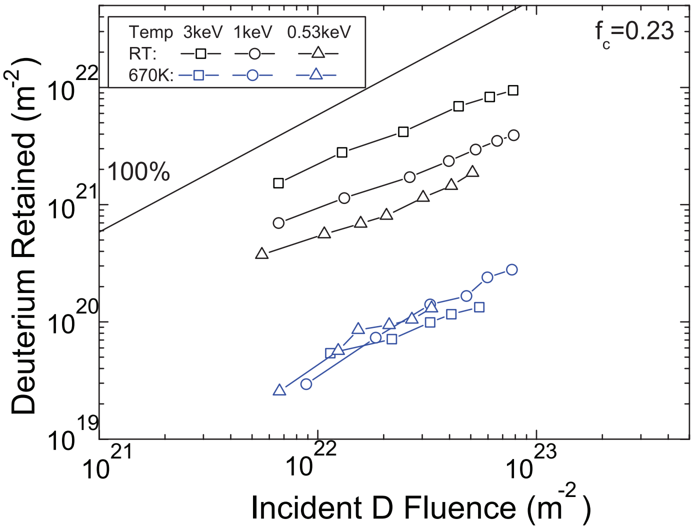

Figure 5.21: Total D retention as function of incident D fluence for $f_c = 0.23$ at RT and $670\,K$ for various incident D energies.

5.2.3 Summary

In the tungsten erosion regime, a lower C areal density is observed at RT compared to that at elevated temperatures. The loss is attributed to chemical sputtering of carbon. A qualitative description of the corresponding processes was discussed, and the magnitude of the chemical sputtering quantified by fitting the experimental data to the phenomenological model. A maximum value of the chemical sputtering yield, $Y_{chem} \approx 0.04$, is observed for $E_D = 3\,keV$ D ion irradiation at RT, which increases with decreasing D energy to a value of $Y_{chem} \approx 0.08$ at $E_D = 1\,keV$ and $E_D = 0.53\,keV$. In the W erosion regime, Y_{chem} remains constant due to the steady state composition of the C-W mixed layer, but in the C deposition regime with continuous growth of a C layer, the initial increase in the chemical yield is followed by a rapid decrease with the formation of a C layer over the mixed C-W layer. The chemical sputtering effect can be directly correlated to the amount of D retained in the specimen. Consequently by increasing the temperature above $670\,K$ the chemical contribution becomes negligible for all D energies. The development of a quantitative model was not possible given the current experimental data set and experimental procedures. A detailed kinetic model will require measurement of C and D depth profiles, which are accessible by ion beam analysis, as well as measurement of the released hydrocarbons (line-of-sight quadrupole). Detailed molecular dynamics simulations are also required to elucidate the bond breaking processes. In principle, if C bond breaking by D ions is the underlying principal process, the chemical sputter yield at RT will display an isotope dependence which has to be confirmed by future studies.

5.3 Discussion and conclusion

In the carbon deposition regime, the dynamics of simultaneous irradiation can be well described by accounting for the increased C self-sputtering with increasing temperature as discussed in section 5.1. In the W erosion regime, the dynamics at RT requires inclusion of a chemical sputtering component in the kinetic BCA model which becomes negligible with increasing temperature as discussed in section 5.2. Therefore, the dominant mechanism that governs the dynamics of simultaneous deuterium and carbon ion irradiation at elevated temperature is the increased C self-sputtering. The effect on the transition point between C deposition and W erosion regimes is clearly seen in Fig. 5.22. The trend of increased initial W sputtering in the C deposition case clearly increases with temperature. In fact, at $870\,K$, the system switches to the W erosion regime, despite the fact that $f_c = 0.14$ is above the transition point of $f_c = 0.11$ at RT. Essentially, the surface C coverage changes very slowly with fluence due to the higher efficiency of C sputtered from the surface, resulting in longer W exposure times that result in an increased amount of W sputtering. Therefore, the major effect of increased C self-sputtering with increasing temperature is an increase in the total fluence required to reach steady state and a shift in the transition point to higher f_c as long as the fractional C sputtering yield is high enough.

Therefore at elevated temperatures, the surface remains a mixed C-W layer to significantly higher incident fluences. Because the steady state mixed C-W region in the W erosion regime is maintained by the continuous source of C provided by the incident

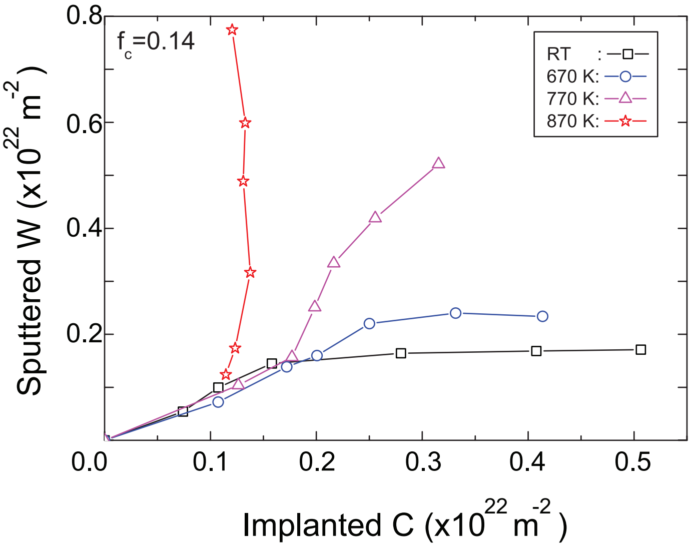

Figure 5.22: Comparison of C implantation and W sputtering behavior for $f_c = 0.14$ at different temperatures with $3\,keV$ D.

C ions, the dynamic equilibrium of the system is very susceptible to changes in the incident parameters (i.e. changes in f_c or ion energies) and target parameters (surface roughness and temperature). The corresponding effects on the dynamic equilibrium state are illustrated in Fig. 5.23 for the case of: (a,b) changing f_c, and (c,d) increase in surface roughness. For the case of C deposition, the incident C flux, f_c, was deliberately reduced and increased leading to corresponding changes in the implanted C areal density, n_c, that is well reproduced by the model as seen in Fig. 5.23(a). In Fig. 5.23(c), a decrease in n_c is observed that is well fitted by the sputtering model using $\alpha = 20°$, to approximate the increased sputtering due to increased surface roughness. Contributions from beam fluctuations is ruled out and corresponding changes in f_c, while the RMS roughness value measured following irradiation ($R_q = 14\,nm$) was larger than typical roughness measured for other specimens in the W erosion regime ($R_q = 10\,nm$). These examples demonstrate how the dynamics of the system can be significantly altered by changes in the incident ions and target morphology parameters, especially in regions close to the transition point.

In conclusion, a comprehensive study examining the processes affecting the dynamics of simultaneous irradiation at RT and elevated temperature was performed. The increase in C self-sputtering was shown to be the dominant mechanism governing the dynamics at elevated temperatures. The processes can be well modeled using the BCA with modified $SBEs$ derived from independent C self-sputtering measurements. The transition point from continuous W erosion to C deposition shifts to higher values of f_c due to the higher efficiency of C sputtered from the surface. This behavior results also in an increase of the total amount of W sputtered. Further, increased C loss from the surface keeps the system in the phase of dynamically varying C-W mixed material layer for a longer period of time. Such behavior can be triggered either by changes in f_c or by the surface roughening due to the prolonged sputtering. At RT, the dominant mechanism governing the erosion-deposition dynamics was determined to be chemical

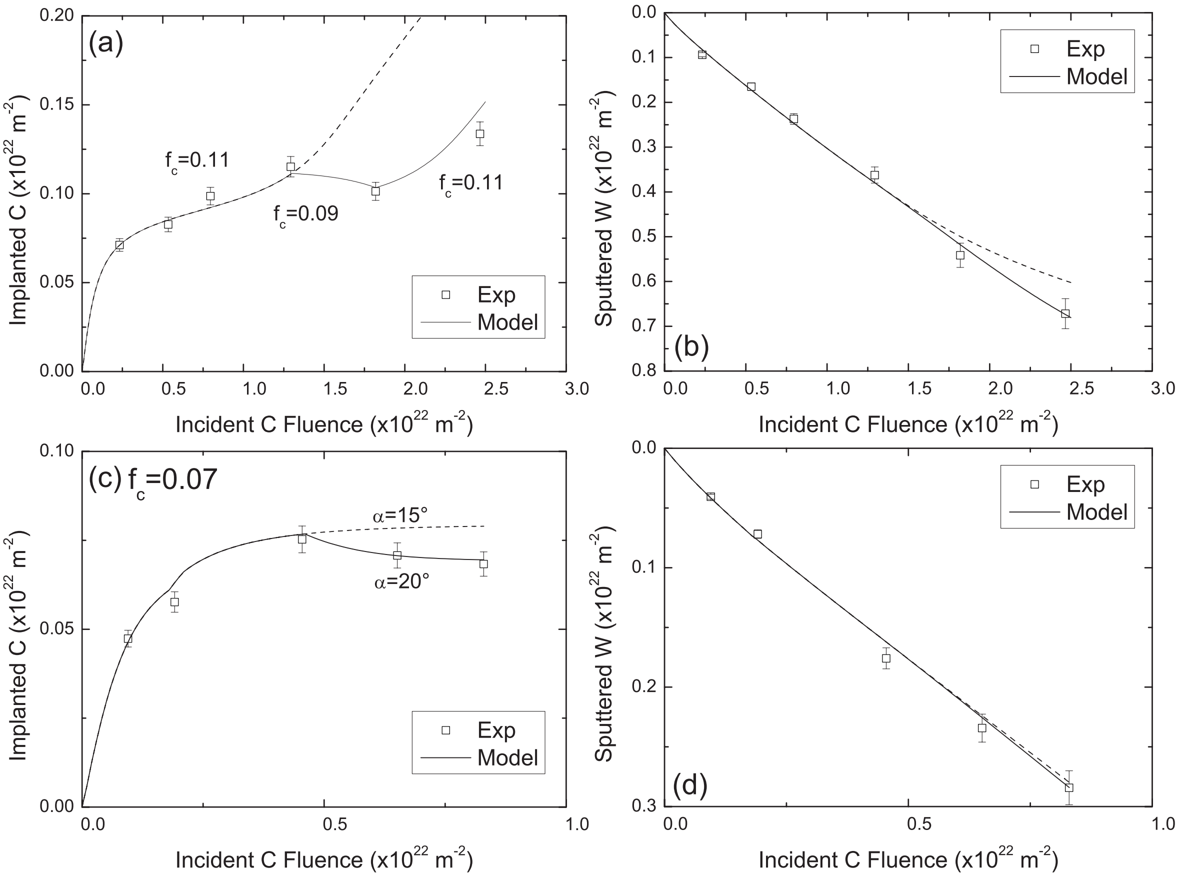

Figure 5.23: The effect of changing f_c on: (a) C implantation, and (b) W erosion. Similarly, the effect of surface roughening on the dynamics of: (c) C implantation, and (d) W erosion, is shown.

sputtering of C in the mixed C-W layer. In the W erosion regime, an upper limit of the chemical erosion yield, $Y_{chem} \approx 0.04$ is observed that decreases with increasing f_c. The chemical effect is more pronounced for decreasing D energies from $E_D = 1 \rightarrow 0.53\,keV$ ($Y_{chem} \approx 0.08$). This synergistic effect requires further experimental studies and additional modeling by molecular dynamics simulations to elucidate the exact reaction mechanisms. The W sputtering behavior was found to be a sum of the weighted Y_w^c and Y_w^D yields, proportional to the surface concentration of tungsten, S_w. Therefore, no synergistic effects on W sputtering behavior was observed. The entire dynamics can be well described by knowing only the C fraction in the incident flux, f_c, and the implanted C areal density, n_c.

6 Modeling

The dynamics of simultaneous irradiation at elevated temperatures involves implantation, reflection, sputtering and diffusion processes to occur at the same time. Therefore, the assumption of constant parameters, like sputtering yields or reflection coefficients is only true for a steady state system where dynamic changes in composition no longer occur. The present work has followed the dynamic evolution of a pure W surface to either a mixed C-W surface with corresponding continuous W erosion or to a pure C surface at a continuously growing C layer. By modeling the experimental data, a quantitative model of the influence of the system's base parameters on the processes governing the dynamics of simultaneous irradiation at elevated temperatures is possible. The kinematic processes governing the C and D ion interactions with W, and the changes to the near surface composition can be well described by the binary collision approximation model implemented in the TRIDYN code. The effect of increased C self-sputtering, discussed in section 4.2, can also be described by using accordingly lower $SBEs$ that fit the measured increase in C self-sputtering yield with temperature. Therefore, TRIDYN allows for a full kinematic description of the C-W system up to $T \leq 870\,K$ studied in this work. Further increase in temperature results in C diffusion, with corresponding changes to the C depth profile, which significantly alters the dynamics. However, diffusion effects are negligible in the temperature range studied and can, if they occur, be modeled by iterative coupling of TRIDYN with an appropriate diffusion code [93]. The question remains how to best model the chemical sputtering processes observed at RT as well as at elevated temperatures. As mentioned earlier, a full quantitative treatment of the chemical sputtering process in C-W mixed materials is not possible yet due to the many unknown parameters that govern this process. Therefore, the chemical component is derived by fitting the experimental data to a phenomenological model outlined below.

The planned approach is to: (1) derive analytic approximations to the kinematic process calculated by TRIDYN using one parameter, n_c, (i.e. the implanted C areal density) that treats both C and W sputtering processes, and (2) incorporating a chemical loss term corresponding to a yield, Y_{chem}, that is varied to fit the experimental data. The goal of the present model is, given a set of initial incident parameters for C and D ions, to correctly describe the dynamics of the W erosion and C implantation rate as a function of incident ion fluence. This will allow in turn to correctly predict the total amount of W eroded and C implanted, as well as to predict what steady state regime the system reaches depending on the system's basic parameters. A key assumption is that the implanted C depth profiles calculated by TRIDYN corresponding to the implanted C areal density, n_c, is representative of the actual experimental C depth profile.

6.1 Kinematic component

The planned approach is to parametrize the reflection yield, R_c, and sputter yield, Y_c^c, as a function of implanted C areal density, n_c, reducing Eqn. 4.1 to an ordinary differential equation:

$$\frac{dn_c}{dt} = \Phi_{\mathrm{c}}(t)\,(1 - R_{\mathrm{c}}(n_c) - Y_c^c(n_c)) \tag{6.1}$$

Setting the initial implanted carbon amount to zero, $n_c(t_o) = n_o = 0$, will allow Eqn. 6.1 to be solved numerically as an initial value problem using the forward Euler method [189] with the following definition for the implanted C areal density, $n_i \triangleq n_{c_i}$:

$$n_c^{'}(t) = f\,(t,\, n_c(t))$$

$$n_{i+1} = n_i + h\,f\,(t_i,\, n_i) = n_i + h\,\Phi_{\mathrm{c}}(t)\,(1 - R_{\mathrm{c}}(n_i) - Y_c^c(n_i))$$

where h is the time step size, resulting in the expression $h\,\Phi_{\mathrm{c}}(t)$ to equal the fluence step size for the present model. The Euler method is a first order method and suffers from larger numerical error as compared to higher order methods like the Runge-Kutta method. However, for the present model, the limiting factor in determining n_c is the accuracy of the $R_{\mathrm{c}}(n_c)$ and $Y_c^c(n_c)$ function parametrization. This means that the fluence step $h\,\Phi_{\mathrm{c}}(t)$ must be chosen small enough to account for all regions where the $R_{\mathrm{c}}(n_c)$ and $Y_c^c(n_c)$ functions are changing rapidly with n_c. It will be shown that this condition is fulfilled for a step size of $h\,\Phi_{\mathrm{c}}(t) = 0.01 \times 10^{22}\,m^{-2}$.

To obtain the parametrized $Y_c^c(n_c)$ and $R_{\mathrm{c}}(n_c)$ functions for RT, $670\,K$, $770\,K$, and $870\,K$, TRIDYN results from Fig. 4.12 are used to fit the following functions as shown in Fig. 6.1:

$$Y_c^c(n_c) = (P_1 + P_2\,n_c)\,exp(-P_3\,n_c) + P_4 \tag{6.2}$$

$$R_{\mathrm{c}}(n_c) = 0.38\,exp(-n_c/0.18) + 0.015 \tag{6.3}$$

with the resulting parameters for varying angles of incidence and temperatures listed in Table 6.1 for $Y_c^c(n_c)$. Table 6.1 shows that the increase in roughness, approximated by increasing the incident angle, shifts the entire $Y_c^c(n_c)$ curve by a constant factor.

So far the model does not differ from the TRIDYN results, and therefore the model should equal TRIDYN calculations. As an example, comparisons of the model curves to TRIDYN calculations for C-only irradiation at $\alpha_T = 15°$ are shown in Fig. 6.2. Good agreement with TRIDYN results is achieved by choosing a fluence step size $\leq 0.01 \times 10^{22}\,m^{-2}$. In section 5.2, the W sputtering dynamics was determined to be a function of the W surface concentration, S_w, as seen from Eqn. 6.4 which is repeated

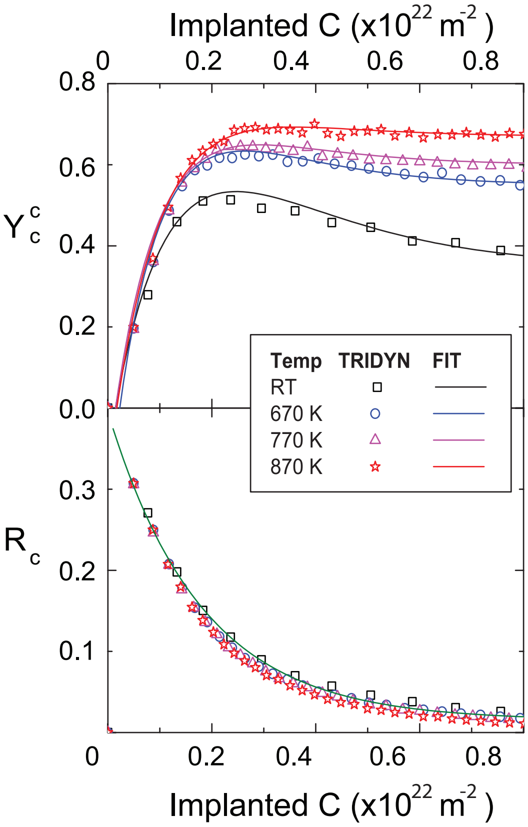

Figure 6.1: Analytical fits for $Y_c^c(n_c)$ and $R_c(n_c)$ for varying temperature using the parameters listed in Table 6.1.

Temp	P_1	P_2	P_3	$P_{4_{\alpha_T=15°}}$	$P_{4_{\alpha_T=20°}}$
RT	-0.46	5.33	6.23	0.345	0.38
$670\,K$	-0.79	5.68	8.10	0.54	0.6
$770\,K$	-0.74	4.37	8.19	0.59	0.65
$870\,K$	-0.83	3.52	8.20	0.660	0.72

Table 6.1: Parameters for the fitting function described in Eqn. 6.2 for varying temperatures and angles of incidence.

below:

$$Y_w = S_w \left[Y_w^c f_c + Y_w^D (1 - f_c) \right] \tag{6.4}$$

Therefore, the S_w corresponding to the amount of C implanted can be obtained from Fig. 4.6, by the following fit:

$$S_w(n_c) = exp(-5.48\, n_c) \tag{6.5}$$

The W sputtered amount corresponding to each fluence step can then be calculated for every n_i:

$$n_{w_i} = h\, \Phi_c(t)\, Y_w(S_w(n_i)) \tag{6.6}$$

A comparison of the model to TRIDYN results for $f_c = 1$ (C-only irradiation) is shown in Fig. 6.3, where a W sputter yield of $Y_c^w = 0.4$, based on the W sputter yield by C calculated using the revised Bohdansky formula was used. Deviations from TRIDYN calculations are observed at low n_c, since $Y_c^w \approx 0.5 > 0.4$ in TRIDYN calculations. This contradiction arises primarily from the approximation of using the W heat of sublimation value ($8.68\, eV$) as the SBE for W atoms in TRIDYN calculations. Deviations at higher n_c arises from the fact that in the phenomenological model, W sputtering is still observed even at low W concentrations, to account for the inhomogeneous coverage of the surface resulting from clustering of carbon atoms on the surface.

A similar procedure is followed to obtain the parametrized $Y_c^D(n_c)$ at varying temperatures and D energies by fitting Eqn. 6.2 to the partial sputtering yields calculated by TRIDYN for simultaneous irradiation at varying temperatures and D energies. The resulting parameters are shown in Table 6.2 for varying temperatures and Table 6.3 for varying incident D energies and temperature.

Temp	P_1	P_2	P_3	$P_{4_{\alpha_T=15}}$	$P_{4_{\alpha_T=20}}$
RT	-0.034	0.39	6.23	0.0100	0.0125
$670\, K$	-0.066	0.59	7.19	0.0200	0.0225
$770\, K$	-0.040	0.37	6.51	0.0230	0.0255
$870\, K$	-0.049	0.38	6.31	0.0275	0.0300

Table 6.2: Parameters for the function $Y_c^D(n_c)$ based on Eqn. 6.2, fitted against the partial D sputter yields from TRIDYN calculations for varying temperatures and angles of incidence.

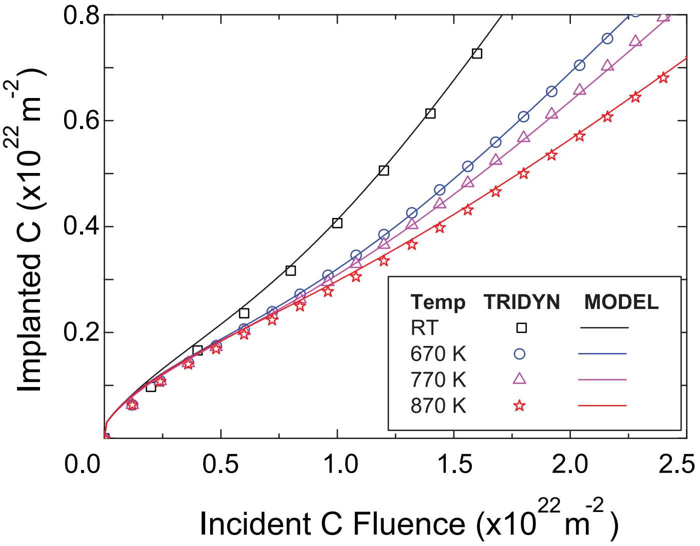

Figure 6.2: Comparison of TRIDYN calculations of n_c, against the model using the analytical forms of $Y_c^c(n_c)$ and $R_c(n_c)$ for varying temperature using the parameters listed in Table 6.1.

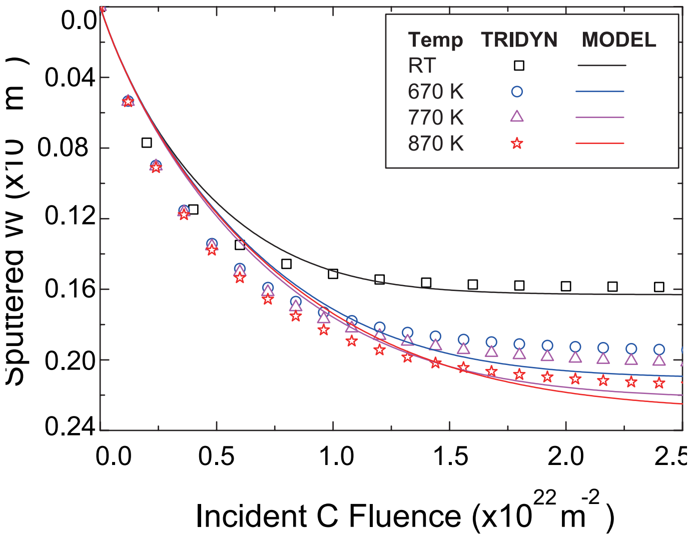

Figure 6.3: Comparison of TRIDYN calculations of n_w, against the model using Eqn. 6.4, where $Y_w(S_w(n_c))$ for varying temperatures.

Energy	Temp	P_1	P_2	P_3	$P_{4_{\alpha_T=15}}$
1.0	RT	-0.021	0.24	6.15	0.0175
0.7	RT	-0.020	0.20	4.81	0.0185
0.53	RT	-0.021	0.24	5.53	0.0190
1.0	$670\,K$	-0.046	0.23	7.75	0.0350
0.53	$670\,K$	-0.048	-0.004	9.96	0.041

Table 6.3: Parameters for the function $Y_c^D(n_c)$ based on Eqn. 6.2, fitted against the partial D sputter yields from TRIDYN calculations for varying D energies at RT and $670\,K$.

It is clearly seen from P_4 (i.e. the steady state sputter yield) in Table 6.2, that Y_c^D increases with increasing temperature due the decreasing SBE of carbon to carbon. In addition, from Table 6.3 it follows that, Y_c^D increases with decreasing D energy due to the increase in energy deposited in the near surface layer. The D contribution to the sputtering of the implanted C is considered independent of the C self-sputtering, resulting in an additional term in Eqn. 6.1:

$$\frac{dn_c}{dt} = \Phi_c(1 - R_\mathrm{c} - Y_c^c) - \Phi_\mathrm{D} Y_c^\mathrm{D} = \Phi_c \left[(1 - R_\mathrm{c} - Y_c^c) - \frac{(1-f_c)}{f_c} Y_c^\mathrm{D} \right] \tag{6.7}$$

$$n_{i+1} = n_i + h\,\Phi_\mathrm{c}(t) \left[(1 - R_\mathrm{c}(n_i) - Y_c^c(n_i) - \frac{(1-f_c)}{f_c} Y_c^\mathrm{D}(n_i) \right]$$

To summarize, Eqns. 6.6 and 6.7 represent a description of the temperature dependent C sputtering behavior and the corresponding W sputtering by both C and D ions based on analytical fit functions using only the C areal density, n_c, as a parameter against TRIDYN calculations. Therefore, the kinematic description of the simultaneous irradiation is complete. As discussed earlier in section 4.2, Y_c^c is dependent on not only the surface concentration of C but also on its depth profile. Therefore, by parametrizing Y_c^c as a function of n_c, the present model takes both dependencies into account. However, this naturally leads to the assumption that the depth profile for a given n_c calculated by TRIDYN correctly describes the experimental results. It will be shown in section 6.3, that this is a valid assumption for $T \leq 870\,K$ where C diffusion into the W bulk can be neglected.

6.2 Chemical sputtering

To model the chemical sputtering process, a chemical component, $Y_{chem}(n_c)$, is added to the D contribution in Eqn. 6.7:

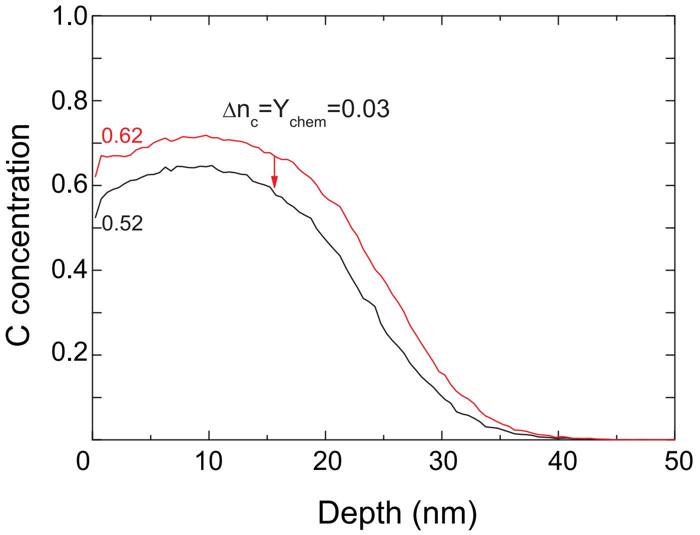

Figure 6.4: Comparison of TRIDYN calculated depth profiles for increasing implanted carbon areal density, n_c. The numbers indicate the surface concentration of carbon.

$$\frac{dn_c}{dt} = \Phi_c \left[(1 - R_\mathrm{c} - Y_c^c) - \frac{(1-f_c)}{f_c} (Y_c^\mathrm{D} + Y_{chem}) \right] \tag{6.8}$$

$$n_{i+1} = n_i + h\, \Phi_\mathrm{c}(t) \left[(1 - R_\mathrm{c}(n_i) - Y_c^c(n_i) - \frac{(1-f_c)}{f_c} (Y_c^\mathrm{D}(n_i) + Y_{chem}(n_i)) \right] \tag{6.9}$$

The function $Y_{chem}(n_c)$ is assumed to be a simple Gaussian function in the form below to model the variation of chemical sputtering with the growth of a C layer:

$$Y_{chem} = a\, e^{-\frac{(n_i - b)^2}{2c^2}} \tag{6.10}$$

All parameters a, b, and c are free parameters determined by fitting the model function 6.10 to the experimental data. Essentially, the Y_{chem} term transforms the system to a state corresponding to a lower implanted C amount as seen in Fig. 6.4. This method is physically justified, since the C loss by chemical sputtering is not limited to the surface only, but occurs throughout the mixed material layer. The validity of using TRIDYN depth profiles for n_c is discussed below.

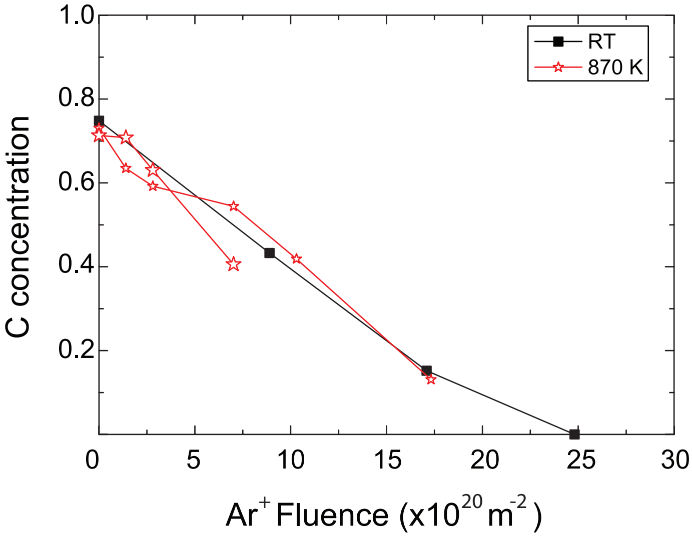

Figure 6.5: Comparison of XPS sputter depth profiles at *RT* and 870 *K* for simultaneous irradiation with $f_c = 0.28$.

6.3 Depth profiles

Parametrizing the Y_c^c and Y_c^D functions against TRIDYN calculations in the model inherently assumes that the calculated depth profiles correspond to experimental results. As discussed in section 4, the thickness of the mixed material layer measured by profilometry of the sputter depth crater corresponded well with the depth calculated by TRIDYN. Therefore, TRIDYN depth profiles can be assumed to correctly describe the experimental data at *RT*. However, this assumption needs to be validated for the case of elevated temperatures. Therefore, XPS sputter depth profiles were obtained at *RT* and 870 *K* for simultaneous irradiation. However, TRIDYN depth profiles cannot be quantitatively compared to the sputter XPS depth profiles. The reason is that the unknown density of the C-W mixed material coupled with a large difference in the partial sputter yields of tungsten and carbon atoms by Ar^+ leads to large uncertainties in the conversion of incident Ar^+ fluence to a depth scale. Still, it is possible to compare the shape of the experimental depth profiles on a relative depth scale. Since there is a buildup of C layer for *RT* results, the first step is to normalize the incident Ar^+ fluence to the same starting point (i.e. the surface C fraction measured by XPS). If there is no change in the relative C concentrations with depth, then the C concentration measured as a function of incident Ar^+ fluence must be equal. This is clearly the case as seen in Fig. 6.5, indicating that no significant changes to the depth profile occur with temperature. Therefore, C diffusion into the W bulk and resulting changes to the C depth profile can be neglected. Consequently, the depth profiles calculated by TRIDYN can be used.

6.4 Summary

A simple model that follows the dynamics of carbon implantation and tungsten sputtering has been developed using the implanted C areal density, n_c, as a parameter.

Analytic fit functions of the kinematic component were derived from TRIDYN calculations, while a chemical loss term, Y_{chem}, allows for the fitting of the experimental data to obtain absolute values. The W sputtering behavior was parametrized against n_c using Eqn. 6.6, which is based on the experimental finding in section 5.2 that the W sputtering is the sum of the weighted Y_w^c and Y_w^D yields, proportional to the surface concentration of tungsten, S_w.

7 Implications for next step fusion reactor

The key plasma facing materials issues which the ITER experiment is facing are outlined by Federici et al. [9] and more recently by Roth et al. [15], while the different requirements for a future fusion reactor, DEMO, have been discussed by Bolt et al. [8]. The main focus in this study has been on interactions of carbon (C) and tungsten (W) plasma facing materials which are mainly applicable within the framework of ITER. Use of carbon materials is at the moment not expected in DEMO, and therefore, the implication of the experimental results specifically to ITER applications will be stressed in the following analysis. The most critical issues ITER is facing have been identified as: (i) lifetime of plasma facing components (PFCs), (ii) dust production from eroded plasma facing material, and (iii) tritium inventory in the vessel, mainly resulting from co-deposition with C and Be. All three issues require an understanding of material sputtering, and more importantly of the erosion, deposition, and re-erosion of the sputtered wall materials and their transport within the vessel.

At present, simulation codes like EDDY [190] and ERO [191] can model local impurity release and the resultant dynamic material mixing due to re-deposition and re-erosion processes following transport in the plasma. The erosion yields by physical sputtering are calculated by TRIDYN or using the TRIM database, while the chemical sputtering process is defined by input or using the analytic formula by Roth et al. [73]. Therefore, improving the predictive quality of the TRIDYN model requires benchmarking against well controlled laboratory experiments that can quantify the sputtering processes in mixed materials.

To extend the scarce knowledge on physics and plasma wall interactions of C-W mixed materials obtained by studies in tokamak experiments, this study examined the dynamics and formation conditions of C-W mixed materials by ion beam experiments with well controlled conditions and experimental parameters. It has yielded quantitative data on surface processes and on the erosion of W as well as of D retention under simultaneous C and D irradiation. It has also identified the main mechanisms that affect the dynamics of mixed material formation and behavior at elevated temperatures. From this data, the TRIDYN model has been successfully bench-marked, and demonstrated to correctly account for the C-implantation and W sputtering behavior under C and D co-bombardment. The successful benchmarking of the TRIDYN model relies on modified surface binding energies used as inputs parameters to account for the increase in C self-sputtering yields.

Therefore, the main achievement in the framework of fusion research is that the TRIDYN model has been bench-marked for a C-W mixed material system at $T \leq 870\,K$. Experimental deviation from TRIDYN calculations have been identified as effects of chemical sputtering and surface roughness, which in some cases are not negligible. Further experimental findings and their respective implications to future fusion reactor are discussed below.

7.1 Tungsten erosion and impact on component lifetime

Tungsten sputtering is an important issue determining the W erosion rate and correspondingly the lifetime of W plasma facing components as well as the W impurity concentration in the plasma. In the case of ITER, off-normal events such as edge-localized modes (ELMs) and disruptions will further limit carbon and tungsten component lifetime in the divertor due to crack formation under repetitive thermal stress or melt layer ejection and sublimation of the material. At present, material solutions do not exist to overcome the reduction of component lifetime by these off-normal events. The only viable solution at hand is the development of discharge plasma scenarios with tolerable ELMs and the development of disruption mitigation systems. In the desired scenario of a quiescent plasma (i.e. with small ELM impact and free of disruptions), the steady state erosion of the components will remain as the only limiting factor for component lifetime. The discussion below follows the assumption that such plasma conditions have been achieved, which is absolutely necessary in the case of future fusion reactors such as DEMO.

Description of tungsten sputtering: The tungsten sputter yield in C-W mixed materials was determined to be the product of the surface concentration of W, S_w, and the linear combination of the sputter yields of pure W by the incident species' weighted to their respective fraction in the incident flux. Therefore, no synergistic effects in the W sputtering behavior was seen. This means that the determination of the total W sputtering yield by additional impurity particles, such as Ar or Ne arising from the seeding of the plasma edge for radiative cooling, or He generated from the D-T reaction is rather straightforward. The literature data for the W sputtering yield by single species irradiation is well known, and therefore, predictions of the total W erosion amount will require only the energy and flux distribution of each incident species with the target dependent parameter being S_w. This allows to use approximated average sputter yields to account for the respective energy and angle distributions of the single species contribution [192]. In practice, plasma simulation codes can provide the required incident parameters, but the W surface concentration is not readily accessible. Especially if one views the problem in terms of integrated discharges and long term exposure of PFCs. However, provided there are diagnostics that can access S_w in-situ before plasma discharges, one would be able to provide certain predictions to the amount of W sputtered to better predict component lifetime and calculate the impurity concentration that can potentially enter the plasma.

Formation of tungsten carbides: In areas of continuous tungsten erosion, the surface of the C-W mixed material is primarily in the form of tungsten carbide whose erosion properties were not significantly different to that of pure W. This is because the enhanced C self-sputtering at elevated temperature appear to affect only the C-C bonds present and do not affect the C-W bonds. Therefore, tungsten carbide formation in ITER is not an issue with respect to altering the W erosion behavior. However, degradation of mechanical properties by embrittlement due to tungsten carbide formation is of concern. A further detrimental effect of carbide formation and C-W mixing is the increased hydrogen trapping.

Effect of chemical sputtering: The fact that chemical sputtering effects in C-W mixed materials is highest at RT and is not observed at $T \geq 670\,K$ indicates that C re-erosion from W surfaces by chemical sputtering processes, and subsequent further

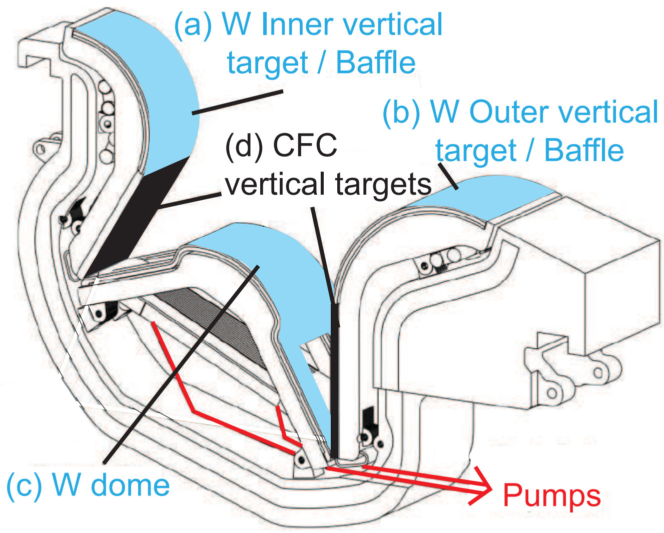
(a) W Inner vertical target / Baffle
(b) W Outer vertical target / Baffle
(d) CFC vertical targets
(c) W dome
Pumps

Figure 7.1: Schematic of ITER divertor cassette showing the locations of the W plasma facing components on: (a) the inner vertical target and baffle, (b) the outer vertical target and baffle, and (c) the dome. The carbon plasma facing components at: (d) the vertical strike plates.

increase in W sputtering, will not be of primary importance under fusion relevant temperatures. However, it is possible that increased D retention in C-W mixed materials at elevated temperatures (possibly from D trapping with He bubbles) can result in higher concentration of D atoms than observed in this study that can then efficiently remove the implanted C resulting in increased W sputtering.

Estimate of tungsten plasma facing component lifetime: As a first approximation in estimating the component lifetime of tungsten PFCs, erosion of W is calculated for the conditions at the (a) inner and (b) outer vertical target area and baffle (see Fig. 7.1) using the following parameters [15, 13, 193]: (1) D flux of $10^{20}\,m^{-2}s^{-1}$ with $400\,sec$ long discharge, (2) W surface temperature of $400\,K$, (3) ion incident angles of $\alpha_T = 65°$, (4) impurity C and Be fractions of $f_c = 0.03$ and $f_{Be} = 0.03$, (5) Charge state, q, of the C and Be ions of $q = 5$ (C^{5+}) and $q = 2$ (Be^{2+}), and (6) with the following plasma ion and electron temperatures at the inner ($T_i = T_e = 10\,eV$) and outer divertor ($T_i = 60\,eV$, $T_e = 30\,eV$). The energy of the ions are approximated by the sum of thermal energy and sheath acceleration energy, $E_{ion} = 3qT_e + 2T_i$, resulting in $E_D = 50\,eV$, $E_{Be} = 80\,eV$, $E_c = 190\,eV$ at the inner divertor and $E_D = 210\,eV$, $E_{Be} = 300\,eV$, $E_c = 570\,eV$ at the outer divertor. Tungsten erosion by physical sputtering processes in the (c) W dome region (see Fig. 7.1) was assumed negligible due to the very low plasma temperatures in this region.

A summary of W gross erosion rates and corresponding lifetime in number of $400\,sec$ plasma discharges (shots) are shown for the inner and outer divertor areas in Table 7.1. The thickness of the tungsten PFC has been taken as $10\,mm$ with the lifetime of the material reached when $2/3$ of its initial thickness is eroded as assumed in Ref. [15]. It is noted that re-deposition of the sputtered W has not been accounted for and therefore the lifetime estimate provides a lower boundary condition. Chemical erosion processes were neglected in the simulations since the C surface concentration was below 30%, and the C on the surface was assumed to be in the form of tungsten carbides as observed earlier in section 5. Chemical sputtering processes were neglected as well since the chemical sputtering processes in mixed C-W material were observed only at RT (see section 5.2.2). Be alloy formation with W can also be neglected for surface temperatures below $900\,K$ [194].

Location of tungsten PFC	Impurity	Erosion rate $[nm/sec]$	Lifetime [shots]
Inner divertor/ Baffle	C	0.0020	8.5×10^6
	C, Be	0.0017	1.0×10^7
Outer divertor/ Baffle	C	0.016	1.0×10^6
	C, Be	0.020	8.2×10^5
Target plate	Ar, Be	0.33	5.0×10^4

Table 7.1: Estimated gross erosion rates for the tungsten plasma facing components (plasma exposed side) at various divertor locations.

The erosion of the tungsten plasma facing component in the inner divertor area is approximately an order of magnitude lower than the outer divertor area. The low erosion rate is due to the low C ion energy which dominates W sputtering, since the D and Be ion energies are below the threshold for W sputtering. Tungsten is continuously eroded for the impurity C and Be fractions of $f_c = 0.03$ and $f_{Be} = 0.03$ used in the calculations. However, in the case of C+Be, accumulation of Be on the surface reduces the W erosion rate. The calculations also show a shift to C deposition regime occurs at C fraction above $f_c = 0.20$, which is significantly higher than the observed impurity transport from spectroscopic measurements (a few %) or modeling. This indicates that significant recycling and re-deposition of the eroded C must occur in the inner divertor regions of tokamaks to explain the strong deposition patterns that is common in all machines [195, 196, 197, 198]. Results of impurity transport modeling indicate that the Be flux fractions at the inner divertor will be higher than in the outer divertor [199], with the highest flux ($f_{Be} = 0.06$) found at the baffle near the inner divertor entrance. The increase in Be flux will correspondingly increase the Be concentration at the surface reducing the W erosion rate even further.

The erosion of the tungsten plasma facing components in the outer divertor is dominated by physical sputtering by C and Be ions. As seen from Table 7.1, the addition of Be increases the erosion rate by 25%. Although a maximum Be flux fraction in the outer divertor was estimated to be below 1% in Ref. [199], a recent extension of the modeling grid from the SOL to the walls indicate an increase in this Be flux amount [200]. Accurate estimates of the impurity fluxes are needed to correctly predict the W component lifetime in the outer divertor region, where clearly the highest W erosion rate occurs. From Table 7.1, it is clear that steady state erosion processes will not be a limiting factor of the W component lifetime in areas of the inner and outer vertical target.

In the case of a full tungsten divertor, tungsten PFCs will also be used at, (d) the target strike plates (see Fig. 7.1), where the ion fluxes are significantly higher ($10^{23} - 10^{24}\,m^{-2}s^{-1}$) and steady state surface temperatures of $500 - 750\,K$ are expected.

The plasma temperature is expected to be similar to conditions at the inner divertor ($T_{i,e} = 10\,eV$) and a simple extrapolation of the C+Be results of the inner divertor calculations will yield a component lifetime of $10^3 - 10^4$ shots. This amount is in good agreement with the most recent estimates of gross W erosion in Ref. [15] using the ERO code [191]. A more realistic assumption is the replacement of the C impurity ions with Ar ions (from plasma seeding) at $E_{Ar} = 10\,eV$ and $f_{Ar} = 0.003$ calculated using the B2/Eirene background plasma [199]. The calculations result in component lifetimes of 5.0×10^4 shots, which is still an order of magnitude higher than the number of discharges planned during the first 10 years of ITER operation [32]. The additional erosion by incident He ions is limited by the low plasma temperature near the strike point. From these basic approximations, the steady state erosion of tungsten plasma facing components, including their use in strike plates, will not significantly affect the component lifetimes in ITER. In the case of DEMO, extrapolating using ITER-like plasma discharges of 5.0×10^4 shots will equal 230 days of continuous operation. Meaning, the use of tungsten PFCs can exclude component lifetime issues from one of the many limiting factors that affect the operation of a fusion reactor. However, such progress can only be made with a disruption free quiescent plasma.

7.2 Issue of fuel inventory and co-deposition

From the above discussion, steady state erosion of the tungsten plasma facing components will not be the limiting factor in the operation of ITER. On the one hand, formation of C-W mixed materials will result in decreased W sputtering in comparison to a pure W material due to the C impurity coverage of the tungsten surface. On the other hand, this beneficial aspect is negated by the re-erosion of C from previously clean surfaces and a corresponding increase of tritium co-deposition with carbon. The co-deposited layers can grow indefinitely with high tritium/carbon ratios, especially in areas that are remote and plasma shadowed, with the consequence of unsaturated tritium inventory in the ITER vessel. In addition, such co-deposited layers are often not stable and can delaminate resulting in dust particles and flakes that are difficult to collect and remove, and can lead to potential explosions at off-normal ingress of air or water. The impact of C-W mixed material formation on tritium retention behavior is discussed below.

Deuterium trapping in C-W mixed material layer: At all temperatures, the relative concentration of D trapped in the mixed material C-W layer was found to be higher than D trapping in pure bulk W or in co-deposited C layers. It is postulated that the additional defects caused by keV C ion irradiation as well as the presence of the implanted C results in the increased trapping within the mixed material layer. As a consequence, in areas of continuous W-erosion, the D trapped at the near surface will be higher than the D retention fraction expected at D-only irradiation. This highlights the importance of considering mixed beam studies to better simulate plasma wall interactions under actual fusion plasma conditions. It is noted that under fusion plasma conditions, this effect of damage creation is not limited to C as was the case in this study. All impurities (Ar, Be, He, W) will result in an increase in D trapping at the near surface by ion-induced damage.

In the tungsten erosion regime, this synergistic effect may, however, keep the D trapped at the near surface and prevent significant D diffusion into the W bulk, alleviating the main concern of hydrogen inventory forming in the W bulk material. It is noted that although the absolute amount decreases with increasing temperature, D trapping at the mixed material layer is still observed at $870\,K$. Therefore, under divertor conditions, these traps do not appear likely to be annealed. However, since the trapping amount in C-W mixed material decreases sharply with temperature, following the behavior of pure W, a hot divertor can keep the hydrogen inventory low in C-W mixed material. Therefore at elevated temperatures, the formation of C-W mixed material does not alter significantly the D retention behavior compared to pure W.

Conversely, in areas of carbon layer growth on top of the C-W mixed material, the high levels of defects created at the mixed material layer can act as a sink for diffusing deuterium. Provided a large D concentration can accumulate in this area, delamination of the overlying C layer may occur by formation of D blisters that rupture. This will have significant consequences to dust generation, considering that most of the D will be co-deposited in the C layer. Obviously, temperature and C layer thickness will be the parameters that determine whether this effect will be important.

Determination of carbon layer thickness: The *SBEs* used in TRIDYN simulations were determined up to a temperature of $T = 870\,K$, and therefore the carbon sputtering behavior can now be well described by TRIDYN in this range. This will allow improved predictions of the C layer growth rate in areas of net carbon deposition, provided the incident flux of C and hydrogen, and the surface temperature are known. The hydrogen/carbon trapping ratio in co-deposited layers as a function of temperature is known from independent experiments, and therefore the improved C sputtering rate can provide in turn, improved predictions of the fuel inventory at least for the plasma exposed surface of the components. It is assumed that the chemical erosion yield by hydrogen as well as the proper sticking coefficients of the sputtered hydrocarbon molecules are correctly accounted for. However, in reality, the contribution to total fuel inventory from C layer growth in gaps in the castellated structure of the PFCs [10, 24] and shadowed and remote areas in the vessel must also be considered. Here, different mechanisms of deposition and erosion dominate [201] and TRIDYN calculations cannot be applied. However, improved modeling of the erosion, re-deposition, and re-erosion cycle can provide improved estimates to the C source term that leads to C buildup in remote areas.

7.3 Limitation of TRIDYN use in modeling plasma wall interactions

The derivation of TRIDYN *SBEs* for carbon sputtering at elevated temperature will allow for better accuracy in determining the physical sputtering behavior of carbon in all areas where carbon is deposited. It has been demonstrated in this study that simultaneous irradiation by impurity and fuel ions at elevated temperatures can be described by TRIDYN provided the surface roughness contribution is not significant. However, as observed from experimental results, surface roughening from erosion is an inevitable process and will be so for plasma facing components in ITER. This results in surface roughness and morphology effects to become a free parameter in the erosion and deposition process that will introduce large uncertainties and making accurate predictions of the erosion behavior of plasma facing components difficult. However, it has been shown that increased surface roughness will result in a shift of the transition point to higher C fractions in the case of carbon layer growth. Therefore, in this case, the transition point calculated by TRIDYN can be taken as the lower limit separating areas of carbon deposition and tungsten erosion. For cases, where the surface roughness dimensions are such that the sputtered carbon can be redeposited in its outward trajectory, resulting in decreased C sputtering, a version of TRIDYN capable of modeling lateral non-uniform surface topography would be required. For surface roughness in one dimension (the other still assumed uniform) such an extension has been developed and used for qualitative interpretation of roughness effects [71].

8 Conclusions

A comprehensive study has been undertaken to examine both the dynamic behavior of carbon (C) implantation and tungsten (W) sputtering under simultaneous irradiation by C and D ions, and the corresponding D retention behavior. The aim of the study was to understand mixed material formation and behavior during plasma wall interactions in fusion devices by controlled ion beam experiments in a laboratory setting. The developed understanding can be applied to provide experimentally bench-marked input parameters used in present day impurity transport codes to better model the erosion and redeposition processes in tokamak devices and extrapolation to ITER and DEMO conditions.

In the experiments, the amount of C implanted, the amount of W sputtered, and the amount of D retained as a function of incident fluence were measured in-situ by ion beam analysis. The parameters considered were: (1) the C fraction in the incident flux, f_c, (2) the specimen temperature ($RT - 870\,K$), and (3) the incident energy of the D ions ($0.53 - 3\,KeV$). A phenomenological model based on TRIDYN calculations has been developed to describe the chemical sputtering component observed during simultaneous irradiation at RT. A fully characterized description of the W sputtering behavior by C was an important prerequisite for separating the effect of additional D bombardment during simultaneous irradiation and quantifying the correspondingly invoked synergistic effects. Therefore, additional experiments examining C and W irradiation by C ions only were performed. The corresponding results are summarized first, followed by the conclusions drawn from the simultaneous C and D irradiation experiments. A discussion of the experimental results in the framework of ITER and future fusion reactors was discussed in section 7.

8.1 Carbon-only irradiation

Two sets of experiments were conducted with $E_c = 6\,keV$ C ions in the temperature range of $RT - 870\,K$. First, W-films deposited on polished Ni substrates were irradiated with C ions to study the C implantation and W sputtering behavior as a function of incident C fluence and temperature. Second, C films deposited on polished W substrates were irradiated with C ions to measure the C self-sputtering yields as a function of temperature. The main conclusions and original contributions are as follows: (1) The W sputtering behavior can be fully characterized by the implanted C, (2) The C self-sputtering yields have been measured in the previously unexamined temperature range of $RT - 870\,K$, (3) The increased C self-sputtering at $T < 870\,K$ has been attributed to correspondingly decreased surface binding energies in the binary collision approximation model implemented in the TRIDYN code. The temperature dependent effects are summarized below.

(i) Dependence of tungsten erosion on implanted carbon: Irradiation of tungsten by $E_c = 6\,keV$ C ions at RT showed that the W sputter yield is a function of the implanted carbon amount, n_c. Therefore, the W sputtering behavior can be fully parametrized by n_c, effectively reducing the problem of C implantation and W sputtering processes at a given incidence energy to one parameter. The W sputtered amount was gradually reduced by the corresponding increase of the implanted C amount, until at $n_c \approx 0.4 \times 10^{22}\,m^{-2}$ (for $E_c = 6\,keV$), the formation of a closed C layer suppressed further sputtering of W. This dependency allows one to correlate the implanted C amount to the C surface concentration, which critically governs the W sputtering yield. The experimentally unavailable C surface concentration can be approximated by TRIDYN calculations, provided the experimental C implantation and W sputtering process can be modeled assuming a laterally uniform smooth surface. Deviations from a smooth surface topography arise at increasing temperature leading to additional effects discussed below. The structure of the growing C layer was determined by Raman spectroscopy and showed a highly disordered network of graphite-like carbon with its structure independent of temperature in the range studied ($RT - 870\,K$).

(ii) Effect of temperature on tungsten erosion and implanted carbon: A change in the C implantation and W sputtering behavior was observed following $n_c \approx 0.1 \times 10^{22}\,m^{-2}$ (for $E_c = 6\,keV$). With increasing temperature, the C sputtering rate increased, requiring higher incident C fluences to form a closed C layer to protect the underlying W. The increased C sputtering resulted in longer exposure of W, which increased the total amount of W sputtered before formation of a closed C layer. For example, an increase of $\approx 50\,\%$ in the total amount of W sputtered is observed at $770\,K$ compared to RT. The increase in the sputtering of implanted C was determined to be from the combined effects of increased C self-sputtering and surface roughness effects, discussed below. Carbon diffusion into the bulk was ruled out by the temperature independent implanted C depth profile determined using XPS. However, possible effects of C diffusion or segregation to the very surface during irradiation could not be determined with the available diagnostics.

(iii) Effect of temperature on C self-sputtering: To quantify the increase of C self-sputtering with temperature, experimental C self-sputtering yields at $670\,K$, $770\,K$, and $870\,K$ were measured by irradiation of C films deposited on polished W substrates using $6\,keV$ C ions. The sputtering yields at $E_c = 6\,keV$ measured were 0.29 ± 0.01, 0.45 ± 0.03, 0.55 ± 0.03, 0.64 ± 0.05 at RT, $670\,K$, $770\,K$, and $870\,K$, respectively. The increase in C self-sputtering yields can be described by the binary collision approximation model (TRIDYN) by reducing the surface binding energies ($SBEs$). The $SBEs$ were obtained by comparison of the BCA results with the experimental C self-sputtering yields resulting in C-C $SBEs$ of 7.4, 4.3, 3.8, and $3.1\,eV$ for RT, $670\,K$, $770\,K$, and $870\,K$, respectively. These $SBEs$ were used to successfully model the experimental results of $6\,keV$ C irradiation of W at $RT \rightarrow 870\,K$. At $T < 870\,K$, the TRIDYN model of reducing the carbon $SBEs$ correctly describes the increased W sputtering and decreased C implantation rate caused by increased C self-sputtering yields with increasing temperature. The good agreement using constant C-W and W-W $SBEs$ for calculations at higher temperatures indicates that the sputtering of tungsten carbides can be assumed to be the same as that of pure W and is independent of temperature. However, at $T = 870\,K$, the increased C self-sputtering alone cannot correctly model the C implantation and W sputtering behavior. Possible changes to the C surface concentration by diffusion or segregation effects and the observed increase in surface roughness are not included in the TRIDYN model and therefore are attributed to the remaining discrepancies. These additional temperature effects need to be implemented in a quantitative model incorporated in TRIDYN, to extend the present model to higher temperatures.

(iv) Effect of temperature on surface topography and roughness: A slightly larger incident angle, $\alpha_T = 20°$ in TRIDYN as compared to the experimental, $\alpha = 15°$, was required to best model the experimental data at $T = 770\,K$ using the benchmarked $SBEs$. The increased angle of incidence was used to approximate the effect of an increase in surface roughness from the annealing process. However, at $T = 870\,K$, the necessity of using an even larger incident angle, $\alpha_T = 25°$, indicates that contributions from surface roughness become significant resulting in different dynamics compared to a laterally uniform smooth surface. Images of surface topography measured using AFM indicate that the C layer growth at higher temperatures is driven by formation of island like structures, indicating a surface growth process based on the mobile C atoms on the surface. With increasing temperature, the C layer is observed to grow increasingly inhomogeneously with larger island like structures that result in a rough surface with a root mean square roughness value, R_q, greater than the mean C ion range of $10\,nm$. The increased temperature facilitates the growth of such island structures, either by diffusion or segregation effects, which have a large effect on the C sputtering behavior by increasing the local angle and also in longer exposure period of the underlying tungsten.

8.2 Simultaneous irradiation by Deuterium and Carbon ions

The C implantation and W sputtering behavior during simultaneous irradiation of W films deposited on polished Ni substrates with $6\,keV$ C ions and $0.53 - 3\,keV$ D ions was studied. The system develops into two distinct steady state regimes of continuous W erosion or continuous C layer growth depending on the key parameters discussed below. The main conclusions and original contributions are as follows: (1) A synergistic effect of combined C and D irradiation at RT results in a significant discrepancy between the BCA-based TRIDYN simulations and the experimental results. This is interpreted as a chemical sputtering process of the trapped D passivating the broken C bonds resulting from both implanted C and D ions. (2) With increasing temperature, the C implantation and W sputtering behavior is described well by the TRIDYN model using $SBEs$ derived from C-only experiments. Therefore, the dominant effect was identified as increased C loss by the increased C self-sputtering yield. No synergistic effects were observed meaning the system can be fully described by the combination of each individual species' contribution to the C loss and growth rate. (3) The W sputtering yield was determined to be a linear superposition of the partial sputter yields weighted to their fraction in the incident flux, which is proportional to the W surface concentration. Conclusions from varying the main parameters in the experiments are summarized below.

(i) Carbon fraction in the incident flux: At RT, the transition point separating the two regimes of continuous W erosion and continuous C layer growth was determined to be in the interval $0.09 < f_c < 0.11$. The system can be primarily characterized by the behavior of the implanted C and its surface concentration and depth distribution as seen from C-only experiments. The effect of simultaneous irradiation with D ions is the introduction of an additional loss mechanism for the implanted C. At f_c values lower than at the transition point concentration, the system is in dynamic equilibrium where the combined C loss rate from both C sputtering by C and D ions and the reflected C ions equals the C implantation rate, resulting in a constant steady state value of the total C amount in the mixed material. Increasing f_c correspondingly increases the C implantation rate and the sharp boundary between the W erosion and C layer growth regimes occurs due to the shift in balance to net C implantation. The consequence of high irradiation fluences in the dynamic W erosion regime can lead to surface roughening that alters the dynamics of the system by increasing the sputter yields. This has the effect of increasing the C loss rate and higher C fractions will be required to shift the system to the C layer growth regime.

(ii) Effect of increased specimen temperature: A temperature increase has two main effects in: (1) increasing the C self-sputtering yields, and (2) decreasing the D retention amount. The increase in C self-sputtering yields has the effect of shifting the transition point to higher f_c with increasing temperature by increasing the C loss rate. At $T = 770\,K$, the transition point was determined between $0.11 < f_c < 0.14$ and at $T = 870\,K$, the transition point was $f_c > 0.14$. In the C deposition regime, the dynamics leading up to a growing C layer can be described by the fitting model based on TRIDYN simulations using the $SBEs$ derived from C self-sputtering experiments. Therefore, the dominant effect is the increase in C loss by the increase in C self-sputtering. The only difference in the fitting model and TRIDYN is the treatment of the W sputtering behavior, where the fitting model assumes the W sputter yield is proportional only to the surface concentration of W. Also, in the W erosion regime, the effect of enhanced C self-sputtering can fully describe the system and chemical sputtering effects were not observed from the mixed material layer. Chemical sputtering effects with the growth of a C layer was not observed due to the experimental limitation of a maximum achievable C layer thickness of $< 80\,nm$. Therefore, the formation of volatile molecules that primarily occurs at the end of the implanted D ions' range still occurred only in the mixed material transition layer and not within the C layer on top. The decrease in D retention fraction with increasing temperature has the effect of reducing the D/C ratio of the co-deposition from 0.4 at RT to 0.05 at $670\,K$ and $770\,K$ in the C deposition regime. In the W sputtering regime, the decreased D retention amount results in negligible chemical sputtering contributions in the mixed material region that were largest at RT. Carbon diffusion into the bulk tungsten at $870\,K$ was shown to be negligible.

(iii) Effect of decreased D energy: At RT, the discrepancy between TRIDYN simulations and experimental results observed in the W erosion regime was interpreted as a chemical sputtering processes. It is postulated that the trapped D in the mixed material is able to passivate the broken C bonds resulting from C and D ion irradiation. The chemical yield was determined by fitting the experimental results using a model developed based on TRIDYN calculations. The effect of reducing the incident D energy from $E_D = 3 \rightarrow 0.53\,keV$ results in an increase in the chemical sputtering yield. A maximum value of $Y_{chem} \approx 0.04$ at $E_D = 3\,keV$ and $Y_{chem} \approx 0.08$ for lower D energies was required to fit the experimental data. The quantitative validation of this hypothesis and of the fit used here as approximation will require detailed molecular dynamics studies and further experiments requiring in-situ surface analysis and line of sight mass spectroscopy diagnostics.

(iv) D retention: At RT, the total D retention amount in unannealed specimens was found to be an order of magnitude higher ($10^{21} - 10^{22}\,m^{-2}$) than literature data. This is due to the contribution of D diffusion and trapping in the Ni substrate to the total D retention amount measured. In the case of annealed specimens, the contribution of the Ni substrate greatly decreased, but D retention amount was still a factor of two higher than published data from bulk tungsten. This increase is partially attributed to the additional D trapping sites formed by simultaneous irradiation of W with energetic keV C ions, as well as the short time interval between irradiation and analysis. In the C deposition regime, the mixed material region contained the highest relative concentration of D trapped compared to the amount trapped in the W bulk or even in the co-deposited C layer. The absolute amount of D trapped in this mixed material layer was observed to decrease with temperature, but D trapping was still observed at $870\,K$, indicating high trap energies normally associated with D trapping at C or vacancy sites. D trapped in these sites does not appear to contribute to chemical sputtering of C. In the W erosion regime, the amount of D retained decreases with increasing temperature and agrees within a factor of two with published data. No dependence on the value of f_c was observed in the retained D amount.

9 List of publications and posters

9.1 Publications

1. H.T. Lee and K. Krieger. *Modeling tungsten and carbon sputtering by carbon at elevated temperatures.* Physica Scripta, accepted.

2. H.T. Lee and K. Krieger. *Simultaneous irradiation of tungsten with deuterium and carbon at elevated temperatures.* Journal of Nuclear Materials, 390-391, 971-974, 2009.

9.2 Poster presentations

1. H.T. Lee and K. Krieger. *Tungsten and carbon sputtering by carbon at elevated temperatures.* 12th International Workshop on Plasma-Facing Materials and Components for Fusion Applications, May 11 - 14th 2009, Jülich, Germany.

2. H.T. Lee and K. Krieger. *Simultaneous irradiation of tungsten with deuterium and carbon at elevated temperatures.* 18th International Conference on Plasma Surface Interactions, May 26 - 30th 2008, Toledo, Spain.

References

[1] R. Toschi. Nuclear fusion, an energy source. *Fusion Engineering and Design*, 36(1):1–8, April 1997.

[2] J D Lawson. Some criteria for a power producing thermonuclear reactor. *Proceedings of the Physical Society. Section B*, 70(1):6–10, 1957.

[3] M. Keilhacker, A. Gibson, C. Gormezano, P.J. Lomas, P.R. Thomas, M.L. Watkins, P. Andrew, B. Balet, D. Borba, C.D. Challis, I. Coffey, G.A. Cottrell, H.P.L. De Esch, N. Deliyanakis, A. Fasoli, C.W. Gowers, H.Y. Guo, G.T.A. Huysmans, T.T.C. Jones, W. Kerner, R.W.T. Konig, M.J. Loughlin, A. Maas, F.B. Marcus, M.F.F. Nave, F.G. Rimini, G.J. Sadler, S.E. Sharapov, G. Sips, P. Smeulders, F.X. Soldner, A. Taroni, B.J.D. Tubbing, M.G. von Hellermann, D.J. Ward, and JET Team. High fusion performance from deuterium-tritium plasmas in jet. *Nuclear Fusion*, 39(2):209–234, 1999.

[4] R. Aymar. Iter r&d: Executive summary: Design overview. *Fusion Engineering and Design*, 55(2-3):107–118, July 2001.

[5] G. Federici, C.H. Skinner, J.N. Brooks, J.P. Coad, C. Grisolia, A.A. Haasz, A. Hassanein, V. Philipps, C.S. Pitcher, J. Roth, W.R. Wampler, and D.G. Whyte. Plasma-material interactions in current tokamaks and their implications for next step fusion reactors. *Nuclear Fusion*, 41(12):1967–2137, 2001.

[6] V. Barabash, A. Peacock, S. Fabritsiev, G. Kalinin, S. Zinkle, A. Rowcliffe, J.-W. Rensman, A.A. Tavassoli, P. Marmy, P.J. Karditsas, F. Gillemot, and M. Akiba. Materials challenges for iter - current status and future activities. *Journal of Nuclear Materials*, 367-370(Part 1):21–32, August 2007.

[7] R. Toschi, P. Barabaschi, D. Campbell, F. Elio, D. Maisonnier, and D. Ward. How far is a fusion power reactor from an experimental reactor. *Fusion Engineering and Design*, 56-57:163–172, October 2001.

[8] H. Bolt, V. Barabash, G. Federici, J. Linke, A. Loarte, J. Roth, and K. Sato. Plasma facing and high heat flux materials - needs for iter and beyond. *Journal of Nuclear Materials*, 307-311(Part 1):43–52, December 2002.

[9] G. Federici, P. Andrew, P. Barabaschi, J. Brooks, R. Doerner, A. Geier, A. Herrmann, G. Janeschitz, K. Krieger, A. Kukushkin, A. Loarte, R. Neu, G. Saibene, M. Shimada, G. Strohmayer, and M. Sugihara. Key iter plasma edge and plasma-material interaction issues. *Journal of Nuclear Materials*, 313-316:11–22, March 2003.

[10] Mario Merola, W. Dänner, J. Palmer, G. Vielder, and C. H. Wu. European contribution to the development of the iter divertor. *Fusion Engineering and Design*, 66-68:211–217, September 2003.

[11] M Balden. Overview on the effects of dopants on chemical erosion and res of carbon-based materials. *Physica Scripta*, T81:64–69, 1999.

[12] C. Garcia-Rosales and M. Balden. Chemical erosion of doped graphites for fusion devices. *Journal of Nuclear Materials*, 290-293:173–179, March 2001.

[13] Joachim Roth, Emmanuelle Tsitrone, Thierry Loarer, Volker Philipps, Sebastijan Brezinsek, Alberto Loarte, Glenn F Counsell, Russell P Doerner, Klaus Schmid, Olga V Ogorodnikova, and Rion A Causey. Tritium inventory in iter plasma-facing materials and tritium removal procedures. *Plasma Physics and Controlled Fusion*, 50(10):103001 (20pp), 2008.

[14] Alberto Loarte. Implications of the use of carbon-based plasma facing components in next step fusion devices. *Physica Scripta*, T111:13–22, 2004.

[15] Joachim Roth, E. Tsitrone, A. Loarte, Th. Loarer, G. Counsell, R. Neu, V. Philipps, S. Brezinsek, M. Lehnen, P. Coad, Ch. Grisolia, K. Schmid, K. Krieger, A. Kallenbach, B. Lipschultz, R. Doerner, R. Causey, V. Alimov, W. Shu, O. Ogorodnikova, A. Kirschner, G. Federici, and A. Kukushkin. Recent analysis of key plasma wall interactions issues for iter. *Journal of Nuclear Materials*, 390-391:1–9, June 2009.

[16] W. Eckstein, C. Garcia-Rosales, J. Roth, and W. Ottenberger. Sputtering data. Technical report, Max-Planck-Institut fur Plasmaphysik, IPP 9/82 (1993).

[17] Rion A. Causey. Hydrogen isotope retention and recycling in fusion reactor plasma-facing components. *Journal of Nuclear Materials*, 300(2-3):91–117, February 2002.

[18] R. Tivey, M. Akiba, D. Driemeyer, I. Mazul, M. Merola, and M. Ulrickson. Iter r&d: Vacuum vessel and in-vessel components: Divertor cassette. *Fusion Engineering and Design*, 55(2-3):219–229, July 2001.

[19] K. Krieger, H. Maier, and R. Neu. Conclusions about the use of tungsten in the divertor of asdex upgrade. *Journal of Nuclear Materials*, 266-269:207–216, March 1999.

[20] A. Kallenbach, P.T. Lang, R. Dux, C. Fuchs, A. Herrmann, H. Meister, V. Mertens, R. Neu, T. Pütterich, and T. Zehetbauer. Integrated exhaust control with divertor parameter feedback and pellet elm pacemaking in asdex upgrade. *Journal of Nuclear Materials*, 337-339:732–736, March 2005.

[21] D. E. Post, R. V. Jensen, C. B. Tarter, W. H. Grasberger, and W. A. Lokke. Steady-state radiative cooling rates for low-density, high-temperature plasmas. *Atomic Data and Nuclear Data Tables*, 20(5):397–439, November 1977.

[22] Tetsuo Tanabe, Nobuaki Noda, and Hiroo Nakamura. Review of high z materials for psi applications. *Journal of Nuclear Materials*, 196-198:11–27, December 1992.

[23] D. Naujoks, J. Roth, K. Krieger, G. Lieder, and M. Laux. Erosion and redeposition in the asdex upgrade divertor. *Journal of Nuclear Materials*, 210(1-2):43–50, June 1994.

[24] J Linke. Plasma facing materials and components for future fusion devices: development, characterization and performance under fusion specific loading conditions. *Physica Scripta*, T123:45–53, 2006.

[25] A. R. Raffray, J. Schlosser, M. Akiba, M. Araki, S. Chiocchio, D. Driemeyer, F. Escourbiac, S. Grigoriev, M. Merola, R. Tivey, G. Vieider, and D. Youchison. Critical heat flux analysis and r&d for the design of the iter divertor. *Fusion Engineering and Design*, 45(4):377–407, August 1999.

[26] P. Andrew, P. D. Brennan, J. P. Coad, J. Ehrenberg, M. Gadeberg, A. Gibson, D. L. Hillis, J. How, O. N. Jarvis, H. Jensen, R. Lässer, F. Marcus, R. Monk, P. Morgan, J. Orchard, A. Peacock, R. Pearce, M. Pick, A. Rossi, P. Schild, B. Schunke, and D. Stork. Tritium retention and clean-up in jet. *Fusion Engineering and Design*, 47(2-3):233–245, December 1999.

[27] C. H. Skinner, E. Amarescu, G. Ascione, W. Blanchard, C. W. Barnes, S. H. Batha, M. Beer, M. G. Bell, R. Bell, M. Bitter, N. L. Bretz, R. Budny, C. E. Bush, R. Camp, M. Casey, J. Collins, M. Cropper, Z. Chang, D. S. Darrow, H. H. Duong, R. Durst, P. C. Efthimion, D. Ernst, N. Fisch, R. J. Fonck, E. Fredrickson, G. Y. Fu, H. P. Furth, C. A. Gentile, M. Gibson, J. Gilbert, B. Grek, L. R. Grisham, G. Hammett, R. J. Hawryluk, H. W. Herrmann, K. W. Hill, J. Hosea, A. Janos, D. L. Jassby, F. C. Jobes, D. W. Johnson, L. C. Johnson, J. Kamperschroer, M. Kalish, H. Kugel, J. Langford, S. Langish, P. H. Lamarche, B. Leblanc, F. M. Levinton, J. Machuzak, R. Majeski, J. Manikam, D. K. Mansfield, E. Mazzucato, K. M. McGuire, R. Mika, G. McKee, D. M. Meade, S. S. Medley, D. R. Mikkelsen, H. E. Mynick, D. Mueller, A. Nagy, R. Nazikian, M. Ono, D. K. Owens, H. Park, S. F. Paul, G. Pearson, M. Petrov, C. K. Phillips, S. Raftopoulos, A. Ramsey, R. Raucci, M. H. Redi, G. Rewoldt, J. Rogers, A. L. Roquemore, E. Ruskov, S. A. Sabbagh, G. Schilling, J. F. Schivell, G. L. Schmidt, S. D. Scott, S. Sesnic, B. C. Stratton, J. D. Strachan, T. Stevenson, D. P. Stotler, E. Synakowski, H. Takahashi, W. Tang, G. Taylor, W. Tighe, J. R. Timberlake, A. von Halle, S. von Goeler, R. T. Walters, R. B. White, J. R. Wilson, J. Winston, K. L. Wong, K. M. Young, M. C. Zarnstorff, and S. J. Zweben. Plasma wall interaction and tritium retention in tftr. *Journal of Nuclear Materials*, 241-243:214–226, February 1997.

[28] M J Rubel, J P Coad, P Wienhold, G Matthews, V Philipps, M Stamp, and T Tanabe. Fuel inventory and co-deposition in grooves and gaps of divertor and limiter structures. *Physica Scripta*, T111:112–117, 2004.

[29] K. Krieger, W. Jacob, D.L. Rudakov, R. Bastasz, G. Federici, A. Litnovsky, H. Maier, V. Rohde, G. Strohmayer, W.P. West, J. Whaley, and C.P.C. Wong. Formation of deuterium-carbon inventories in gaps of plasma facing components. *Journal of Nuclear Materials*, 363-365:870–876, June 2007.

[30] D L Rudakov, W Jacob, K Krieger, A Litnovsky, V Philipps, W P West, C P C Wong, S L Allen, R J Bastasz, J A Boedo, N H Brooks, R L Boivin, G De Temmerman, M E Fenstermacher, M Groth, E M Hollmann, C J Lasnier, A G

McLean, R A Moyer, P C Stangeby, W R Wampler, J G Watkins, P Wienhold, and J Whaley. Dimes studies of temperature dependence of carbon erosion and re-deposition in the lower divertor of diii-d under detachment. *Physica Scripta*, T128:29–34, 2007.

[31] A. Litnovsky, P. Wienhold, V. Philipps, K. Krieger, A. Kirschner, D. Matveev, D. Borodin, G. Sergienko, O. Schmitz, A. Kreter, U. Samm, S. Richter, and U. Breuer. Investigations of castellated structures for iter: The effect of castellation shaping and alignment on fuel retention and impurity deposition in gaps. *Journal of Nuclear Materials*, 390-391:556–559, June 2009.

[32] M. Shimada, R. Pitts, A. Loarte, D.J. Campbell, M. Sugihara, V. Mukhovatov, A. Kukushkin, and V. Chuyanov. Iter research plan of plasma-wall interaction. *Journal of Nuclear Materials*, 390-391:282–285, June 2009.

[33] J. Roth, V.Kh. Alimov, A.V. Golubeva, R.P. Doerner, J. Hanna, E. Tsitrone, Ch. Brosset, V. Rohde, A. Herrmann, and M. Mayer. Deuterium retention in carbon fibre composites nb31 and n11 irradiated with low-energy d ions. *Journal of Nuclear Materials*, 363-365:822–826, June 2007.

[34] G Counsell, P Coad, C Grisola, C Hopf, W Jacob, A Kirschner, A Kreter, K Krieger, J Likonen, V Philipps, J Roth, M Rubel, E Salancon, A Semerok, F L Tabares, A Widdowson, and JET EFDA contributors. Tritium retention in next step devices and the requirements for mitigation and removal techniques. *Plasma Physics and Controlled Fusion*, 48(12B):B189–B199, 2006.

[35] P.C. Stangeby and J.D. Elder. Calculation of observable quantities using a divertor impurity interpretive code, divimp. *Journal of Nuclear Materials*, 196-198:258–263, December 1992.

[36] D. Naujoks, R. Behrisch, J.P. Coad, and L.C.J.M. De Kock. Material transport by erosion and redeposition on surface probes in the scrape-off layer of jet. *Nuclear Fusion*, 33(4):581–590, 1993.

[37] A. Kirschner, V. Philipps, J. Winter, and U. Kogler. Simulation of the plasma-wall interaction in a tokamak with the monte carlo code ero-textor. *Nuclear Fusion*, 40(5):989–1001, 2000.

[38] D P Coster, X Bonnin, and M Warrier. Extensions to the solps edge plasma simulation code to include additional surface interaction posibilities. *Physica Scripta*, T124:9–12, 2006.

[39] D. Reiter, Chr. May, D. Coster, and R. Schneider. Time dependent neutral gas transport in tokamak edge plasmas. *Journal of Nuclear Materials*, 220-222:987–992, April 1995.

[40] P.C. Stangeby, J.D. Elder, J.A. Boedo, B. Bray, N.H. Brooks, M.E. Fenstermacher, M. Groth, R.C. Isler, L.L. Lao, S. Lisgo, G.D. Porter, D. Reiter, D.L. Rudakov, J.G. Watkins, W.P. West, and D.G. Whyte. Interpretive modeling of

simple-as-possible-plasma discharges on diii-d using the oedge code. *Journal of Nuclear Materials*, 313-316:883–887, March 2003.

[41] R. Neu, K. Asmussen, S. Deschka, A. Thoma, M. Bessenrodt-Weberpals, R. Dux, W. Engelhardt, J. C. Fuchs, J. Gaffert, C. García-Rosales, A. Herrmann, K. Krieger, F. Mast, J. Roth, V. Rohde, M. Weinlich, and U. Wenzel. The tungsten experiment in asdex upgrade. *Journal of Nuclear Materials*, 241-243:678–683, February 1997.

[42] K. Krieger, A. Geier, X. Gong, H. Maier, R. Neu, and V. Rohde. Erosion and migration of tungsten employed at the main chamber first wall of asdex upgrade. *Journal of Nuclear Materials*, 313-316:327–332, March 2003.

[43] M. Mayer, V. Rohde, J. Likonen, E. Vainonen-Ahlgren, K. Krieger, X. Gong, and J. Chen. Carbon erosion and deposition on the asdex upgrade divertor tiles. *Journal of Nuclear Materials*, 337-339:119–123, March 2005.

[44] R. Neu, Ch. Hopf, A. Kallenbach, T. Pütterich, R. Dux, H. Greuner, O. Gruber, A. Herrmann, K. Krieger, H. Maier, and V. Rohde. Operational conditions in a w-clad tokamak. *Journal of Nuclear Materials*, 367-370(Part 2):1497–1502, August 2007.

[45] J. Paméla, G.F. Matthews, V. Philipps, and R. Kamendje. An iter-like wall for jet. *Journal of Nuclear Materials*, 363-365:1–11, June 2007.

[46] G F Matthews, P Edwards, T Hirai, M Kear, A Lioure, P Lomas, A Loving, C Lungu, H Maier, P Mertens, D Neilson, R Neu, J Pamela, V Philipps, G Piazza, V Riccardo, M Rubel, C Ruset, E Villedieu, and M Way on behalf of the ITER-like Wall Project Team. Overview of the iter-like wall project. *Physica Scripta*, T128:137–143, 2007.

[47] J. P. Biersack and W. Eckstein. Sputtering studies with the monte carlo program trim.sp. *Applied Physics A: Materials Science & Processing*, 34(2):73–94, June 1984.

[48] W. Möller, W. Eckstein, and J. P. Biersack. Tridyn-binary collision simulation of atomic collisions and dynamic composition changes in solids. *Computer Physics Communications*, 51(3):355–368, November 1988.

[49] D. Naujoks and W. Eckstein. Sputtering of plasma facing material by simultaneous bombardment with carbon and deuterium ions. *Journal of Nuclear Materials*, 220-222:993–996, April 1995.

[50] R.P. Doerner. The implications of mixed-material plasma-facing surfaces in iter. *Journal of Nuclear Materials*, 363-365:32–40, June 2007.

[51] H. Maier, K. Krieger, M. Balden, Roth, and J. the ASDEX Upgrade-Team. Erosion and deposition in the asdex upgrade tungsten divertor experiment. *Journal of Nuclear Materials*, 266-269:1003–1008, March 1999.

[52] M Rubel, V Philipps, A Huber, and T Tanabe. Formation of carbon containing layers on tungsten test limiters. *Physica Scripta*, T81:61–63, 1999.

[53] D. Hildebrandt, P. Wienhold, and W. Schneider. Mixed-material coating formation on tungsten surfaces during plasma exposure in textor-94. *Journal of Nuclear Materials*, 290-293:89–93, March 2001.

[54] V. Philipps, A. Pospieszczyk, A. Huber, A. Kirschner, J. Rapp, B. Schweer, P. Wienhold, G. van Oost, G. Sergienko, T. Tanabe, K. Ohya, M. Wada, T. Ohgo, and M. Rubel. Experiments with tungsten limiters in textor-94. *Journal of Nuclear Materials*, 258-263(Part 1):858–864, October 1998.

[55] M Mayer, V Rohde, G Ramos, E Vainonen-Ahlgren, J Likonen, and J L Chen. Erosion of tungsten and carbon markers in the outer divertor of asdex-upgrade. *Physica Scripta*, T128:106–110, 2007.

[56] K Ohya, Y Nakayama, Y Hamada, T Tanabe, A Kirschner, V Philipps, and N Noda. Modeling of material mixing effects on plasma surface interactions in magnetic fusion devices. *Physica Scripta*, T111:138–144, 2004.

[57] K. Ohya, T. Tanabe, A. Kirschner, T. Hirai, V. Philipps, M. Wada, T. Ohgo, and N. Noda. Dynamic transition between erosion and deposition on a tungsten surface exposed to edge plasmas containing carbon impurities. *Journal of Nuclear Materials*, 337-339:882–886, March 2005.

[58] Y. Ueda, M. Fukumoto, A. Yamawaki, Y. Soga, Y. Ohtsuka, S. Brezinsek, T. Hirai, A. Kirschner, A. Kreter, A. Litnovsky, V. Philipps, A. Pospieszczyk, B. Schweer, G. Sergienko, T. Tanabe, K. Sugiyama, K. Ohya, and N. Ohno. Effects of tungsten surface conditions on carbon deposition. *Journal of Nuclear Materials*, 390-391:44–48, June 2009.

[59] M. Psoda, M. Rubel, G. Sergienko, P. Sundelin, and A. Pospieszczyk. Material mixing on plasma-facing components: Compound formation. *Journal of Nuclear Materials*, 386-388:740–743, April 2009.

[60] K. Schmid and J. Roth. Erosion of high-z metals with typical impurity ions. *Journal of Nuclear Materials*, 313-316:302–310, March 2003.

[61] W. Eckstein and J. Roth. Sputtering of tungsten by carbon. *Nuclear Instruments and Methods in Physics Research Section B: Beam Interactions with Materials and Atoms*, 53(3):279–284, March 1991.

[62] W. Eckstein, K. Krieger, and J. Roth. Erosion of w and deposition of c due to bombardment with d and ch3. *Journal of Nuclear Materials*, 258-263(Part 1):912–916, October 1998.

[63] W. Eckstein, V. I. Shulga, and J. Roth. Carbon implantation into tungsten at elevated temperatures. *Nuclear Instruments and Methods in Physics Research Section B: Beam Interactions with Materials and Atoms*, 153(1-4):415–421, June 1999.

[64] W. Eckstein. Dynamic behaviour of the systems be-c, be-w and c-w. *Journal of Nuclear Materials*, 281(2-3):195–202, October 2000.

[65] K. Krieger and J. Roth. Synergistic effects by simultaneous bombardment of tungsten with hydrogen and carbon. *Journal of Nuclear Materials*, 290-293:107–111, March 2001.

[66] K. Schmid, J. Roth, and W. Eckstein. Influence of diffusion on w sputtering by carbon. *Journal of Nuclear Materials*, 290-293:148–152, March 2001.

[67] Y. Ueda, M. Fukumoto, I. Sawamura, D. Sakizono, T. Shimada, and M. Nishikawa. Carbon impurity behavior on plasma facing surface of tungsten. *Fusion Engineering and Design*, 81(1-7):233–239, February 2006.

[68] I. Bizyukov and K. Krieger. Dual beam experiment for simultaneous irradiation of surfaces with ion species of gaseous and solid-state elements. *Review of Scientific Instruments*, 77(4):043501, 2006.

[69] Ivan Bizyukov, Karl Krieger, Nikolay Azarenkov, and Udo v. Toussaint. Relevance of surface roughness to tungsten sputtering and carbon implantation. *Journal of Applied Physics*, 100(11):113302, 2006.

[70] I. Bizyukov, K. Krieger, N. Azarenkov, Ch. Linsmeier, and S. Levchuk. Tungsten sputtering and accumulation of implanted carbon and deuterium by simultaneous bombardment with d and c ions. *Journal of Nuclear Materials*, 363-365:1184–1189, June 2007.

[71] Ivan Bizyukov, Andreas Mutzke, Ralf Schneider, Alexander M. Gigler, and Karl Krieger. Morphology and changes of elemental surface composition of tungsten bombarded with carbon ions. *Nuclear Instruments and Methods in Physics Research Section B: Beam Interactions with Materials and Atoms*, 266(9):1979–1986, May 2008.

[72] G. Federici, R. A. Anderl, P. Andrew, J. N. Brooks, R. A. Causey, J. P. Coad, D. Cowgill, R. P. Doerner, A. A. Haasz, G. Janeschitz, W. Jacob, G. R. Longhurst, R. Nygren, A. Peacock, M. A. Pick, V. Philipps, J. Roth, C. H. Skinner, and W. R. Wampler. In-vessel tritium retention and removal in iter. *Journal of Nuclear Materials*, 266-269:14–29, March 1999.

[73] Joachim Roth. Chemical erosion of carbon based materials in fusion devices. *Journal of Nuclear Materials*, 266-269:51–57, March 1999.

[74] Harold F. Winters and J. W. Coburn. Surface science aspects of etching reactions. *Surface Science Reports*, 14(4-6):162–269, 1992.

[75] J. Roth, J. Bohdansky, and K. L. Wilson. Erosion of carbon due to bombardment with energetic ions at temperatures up to 2000 k. *Journal of Nuclear Materials*, 111-112:775–780, 1982.

[76] J. Roth and W. Möller. Mechanism of enhanced sputtering of carbon at temperatures above 1200°c. *Nuclear Instruments and Methods in Physics Research Section B: Beam Interactions with Materials and Atoms*, 7-8(Part 2):788–792, March 1985.

[77] W. Eckstein. *Computer Simulation of Ion-Solid Interactions.* Springer-Verlag, 1991.

[78] Peter Sigmund. Theory of sputtering. i. sputtering yield of amorphous and polycrystalline targets. *Phys. Rev.*, 184(2):383–416, August 1969.

[79] R. Behrisch. *Sputtering by Particle Bombardment I.* Springer Verlag, Berlin, 1981.

[80] J. Bohdansky. A universal relation for the sputtering yield of monatomic solids at normal ion incidence. *Nuclear Instruments and Methods in Physics Research Section B: Beam Interactions with Materials and Atoms*, 2(1-3):587–591, March 1984.

[81] W. D. Wilson, L. G. Haggmark, and J. P. Biersack. Calculations of nuclear stopping, ranges, and straggling in the low-energy region. *Phys. Rev. B*, 15(5):2458–2468, March 1977.

[82] C. García-Rosales, W. Eckstein, and J. Roth. Revised formulae for sputtering data. *Journal of Nuclear Materials*, 218(1):8–17, January 1995.

[83] Y. Yamamura, Y. Itikawa, and N. Itoh. Technical report, IPPJ-AM-26, Nagoya (1983).

[84] J.P. Biersack and L. Haggmark. *Nuclear Instruments and Methods in Physics Research B*, 174:257, 1980.

[85] J. Lindhard and M. Scharff. Energy dissipation by ions in the kev region. *Phys. Rev.*, 124(1):128–130, October 1961.

[86] Ordean S. Oen and Mark T. Robinson. Computer studies of the reflection of light ions from solids. *Nuclear Instruments and Methods*, 132:647–653.

[87] E. Hechtl, J. Bohdansky, and J. Roth. The sputtering yield of typical impurity ions for different fusion reactor materials. *Journal of Nuclear Materials*, 103:333–337, 1981.

[88] H. Bergsåker, S. Nagata, and B. Emmoth. Carbon sputtering of a thin carbon film, a pure graphite sample and a part of an exposed limiter sample from jet. *Journal of Nuclear Materials*, 145-147:364–367, February 1987.

[89] J. Roth, J. Bohdansky, and W. Ottenberger. Unity yield conditions for sputtering of graphite by carbon ions. *Journal of Nuclear Materials*, 165(3):193–198, June 1989.

[90] W. Eckstein and J. P. Biersack. Self-sputtering and reflection. *Zeitschrift für Physik B Condensed Matter*, 63(1):109–120, March 1986.

[91] W. Möller. Pidat - a computer program for imlant diffusion and trapping. Technical report, IPP 9/44, 1983.

[92] A.I. Nakanechinikov, L.V. Pavlinov, and V.N. Bykov. *Fiz. Met. Metalloved*, 22:234, 1966.

[93] K. Schmid and J. Roth. Concentration dependent diffusion of carbon in tungsten. *Journal of Nuclear Materials*, 302(2-3):96–103, April 2002.

[94] Manuel A. Kanter. Diffusion of carbon atoms in natural graphite crystals. *Phys. Rev.*, 107(3):655–663, August 1957.

[95] I. Bizyukov, K. Krieger, N. Azarenkov, S. Levchuk, and Ch. Linsmeier. Formation of d inventories and structural modifications by deuterium bombardment of tungsten thin films. *Journal of Nuclear Materials*, 337-339:965–969, March 2005.

[96] H. Plank and W. Eckstein. Preferential sputtering of carbides under deuterium irradiation – a comparison between experiment and computer simulation. *Nuclear Instruments and Methods in Physics Research Section B: Beam Interactions with Materials and Atoms*, 124(1):23–30, April 1997.

[97] M. I. Guseva, A. L. Suvorov, S. N. Korshunov, and N. E. Lazarev. Sputtering of beryllium, tungsten, tungsten oxide and mixed w-c layers by deuterium ions in the near-threshold energy range. *Journal of Nuclear Materials*, 266-269:222–227, March 1999.

[98] J. Roth. *Sputtering by Particle Bombardment II.* Springer Verlag, Berlin, 1983.

[99] Wolfgang. O. Hofer and Joachim Roth, editors. *Physical processes of the interaction of fusion plasmas with solids.* Academic Press, 1996.

[100] A. A. Haasz and J. W. Davis. Hydrogen isotopic effects on the erosion of carbon. *Fusion Science and Technology*, 50:58, 2006.

[101] J. Biener, U. A. Schubert, A. Schenk, B. Winter, C. Lutterloh, and J. Kuppers. A surface reaction with atoms: Hydrogenation of sp- and sp2-hybridized carbon by thermal h(d) atoms. *The Journal of Chemical Physics*, 99(4):3125–3128, 1993.

[102] C. Lutterloh, A. Schenk, J. Biener, B. Winter, and J. Küppers. D(h) atom impact induced eley-rideal hydrogen abstraction reaction towards hd at fully hydrogenated c:h(d) film surfaces. *Surface Science*, 316(1-2):L1039–L1043, September 1994.

[103] A. Schenk, J. Biener, B. Winter, C. Lutterloh, U. A. Schubert, and J. Kuppers. Mechanism of chemical erosion of sputter-deposited c:h films. *Applied Physics Letters*, 61(20):2414–2416, 1992.

[104] A. Horn, A. Schenk, J. Biener, B. Winter, C. Lutterloh, M. Wittmann, and J. Küppers. H atom impact induced chemical erosion reaction at c:h film surfaces. *Chemical Physics Letters*, 231(2-3):193–198, December 1994.

[105] E. Vietzke, K. Flaskamp, V. Philipps, G. Esser, P. Wienhold, and J. Winter. Chemical erosion of amorphous hydrogenated carbon films by atomic and energetic hydrogen. *Journal of Nuclear Materials*, 145-147:443–447, February 1987.

[106] Jürgen Küppers. The hydrogen surface chemistry of carbon as a plasma facing material. *Surface Science Reports*, 22(7-8):249–321, 1995.

[107] J. Roth. *"Chemical Sputtering", in Sputtering by Particls Bombardment II.* Springer-Verlag, 1983.

[108] C. M. Braganza, S. K. Erents, and G. M. McCracken. Interactions of 5-30 kev deuterons with a carbon surface. *Journal of Nuclear Materials*, 75(2):220–225, August 1978.

[109] M. Balden and J. Roth. New weight-loss measurements of the chemical erosion yields of carbon materials under hydrogen ion bombardment. *Journal of Nuclear Materials*, 280(1):39–44, June 2000.

[110] J. Roth and C. Garcia-Rosales. Analytic description of the chemical erosion of graphite by hydrogen ions. *Nuclear Fusion*, 36(12):1647–59, 1996.

[111] J. Roth and J. Bohdansky. Mechanism of hydrocarbon formation upon interaction of energetic hydrogen ions with graphite. *Applied Physics Letters*, 51(13):964–966, 1987.

[112] E. Vietzke, K. Flaskamp, and V. Philipps. Differences in the ch3 and ch4 formation from graphite under bombardment with hydrogen ions and hydrogen atoms/argon ions. *Journal of Nuclear Materials*, 128-129:545–550, December 1984.

[113] B. V. Mech, A. A. Haasz, and J. W. Davis. Model for the chemical erosion of graphite due to low-energy h and d impact. *Journal of Applied Physics*, 84(3):1655–1669, 1998.

[114] B. V. Mech, A. A. Haasz, and J. W. Davis. Isotopic effects in hydrocarbon formation due to low-energy h+/d+ impact on graphite. *Journal of Nuclear Materials*, 255(2-3):153–164, June 1998.

[115] R. Schwörer, H. Plank, and J. Roth. Surface modifications and erosion yields of silicon and titanium doped graphites due to low energy d+ bombardment. *Journal of Nuclear Materials*, 230(3):208–213, June 1996.

[116] Allen Y. K. Chen, A. A. Haasz, and J. W. Davis. Comparison of the chemical erosion yields of doped graphites. *Journal of Nuclear Materials*, 227(1-2):66–75, December 1995.

[117] C. Hopf and W. Jacob. Bombardment of graphite with hydrogen isotopes: A model for the energy dependence of the chemical sputtering yield. *Journal of Nuclear Materials*, 342(1-3):141–147, June 2005.

[118] C. Hopf, A. von Keudell, and W. Jacob. Chemical sputtering of hydrocarbon films. *Journal of Applied Physics*, 94(4):2373–2380, 2003.

[119] C. Hopf, W. Jacob, and A. von Keudell. Ion-induced surface activation, chemical sputtering, and hydrogen release during plasma-assisted hydrocarbon film growth. *Journal of Applied Physics*, 97(9):094904, 2005.

[120] W Jacob, C Hopf, and M Schluter. Chemical sputtering of carbon materials due to combined bombardment by ions and atomic hydrogen. *Physica Scripta*, T124:32–36, 2006.

[121] E. Salonen, K. Nordlund, J. Keinonen, and C. H. Wu. Bond-breaking mechanism of sputtering. *Europhysics Letters*, 52(5):504–510, dec 2000.

[122] E. Salonen, K. Nordlund, J. Keinonen, and C. H. Wu. Swift chemical sputtering of amorphous hydrogenated carbon. *Phys. Rev. B*, 63(19):195415, Apr 2001.

[123] Ivan Bizyukov and Karl Krieger. Principal processes occurring at simultaneous bombardment of tungsten by carbon and deuterium ions. *Journal of Applied Physics*, 102(7):074923, 2007.

[124] T. Shimada, T. Funabiki, R. Kawakami, Y. Ueda, and M. Nishikawa. Carbon behavior on tungsten surface after carbon and hydrogen mixed beam irradiation. *Journal of Nuclear Materials*, 329-333(Part 1):747–751, August 2004.

[125] Retsuo Kawakami, Tomohisa Shimada, Yoshio Ueda, and Masahiro Nishikawa. Dynamic behavior of tungsten surfaces due to simultaneous impact of hydrogen and carbon ion beam. *Japanese Journal of Applied Physics*, 42(Part 1, No. 12):7529–7535, 2003.

[126] Wenmin Wang, V. Kh. Alimov, B. M. U. Scherzer, and J. Roth. Deuterium trapping in and release from tungsten carbide. *Journal of Nuclear Materials*, 241-243:1087–1092, February 1997.

[127] Masaki Taniguchi, Kazuyoshi Sato, Koichiro Ezato, Kenji Yokoyama, Masayuki Dairaku, and Masato Akiba. Sputtering of carbon-tungsten mixed materials by low energy deuterium. *Journal of Nuclear Materials*, 313-316:360–363, March 2003.

[128] V Kh Alimov. Deuterium retention in pure and mixed plasma facing materials. *Physica Scripta*, T108:46–56, 2004.

[129] C.H. Skinner, A. A. Haasz, V. Alimov, N. Bekris, R. Causey, R. Clark, J.P. Coad, J. W. Davis, R. Doerner, M. Mayer, A. Pisarev, J. Roth, and T. Tanabe. Recent advances on hydrogen retention in iter's plasma-facing materials: Beryllium, carbon, and tungsten. *Fusion Science and Technology*, 54:891–945, 2008.

[130] D. Hildebrandt, M. Akbi, B. Jüttner, and W. Schneider. Deuterium trapping in divertor tiles of asdex-upgrade. *Journal of Nuclear Materials*, 266-269:532–537, March 1999.

[131] Rion A Causey and Thomas J Venhaus. The use of tungsten in fusion reactors: a review of the hydrogen retention and migration properties. *Physica Scripta*, T94:9–15, 2001.

[132] A. A. Haasz and J. W. Davis. *Nuclear Fusion Research, Springer-Verlag Series in Chemical Physics*. Springer-Verlag, Heidelberg, Germany, 2005.

[133] V.Kh. Alimov and D.A. Komarov. Deuterium retention in carbon and tungsten-carbon mixed films deposited by magnetron sputtering in d2 atmosphere. *Journal of Nuclear Materials*, 313-316:599–603, March 2003.

[134] K. Sugiyama, K. Krieger, C.P. Lungu, and J. Roth. Hydrogen retention in iter relevant mixed material layers. *Journal of Nuclear Materials*, 390-391:659–662, June 2009.

[135] E. Igarashi, Y. Nishikawa, T. Nakahata, A. Yoshikawa, M. Oyaidzu, Y. Oya, and K. Okuno. Dependence of implantation temperature on chemical behavior of energetic deuterium implanted into tungsten carbide. *Journal of Nuclear Materials*, 363-365:910–914, June 2007.

[136] H. Kimura, Y. Nishikawa, T. Nakahata, M. Oyaidzu, Y. Oya, and K. Okuno. Chemical behavior of energetic deuterium implanted into tungsten carbide. *Fusion Engineering and Design*, 81(1-7):295–299, February 2006.

[137] T. Hino, F. Hirano, Y. Yamauchi, and Y. Hirohata. Hydrogen retention and erosion of carbon-tungsten mixed material. *Fusion Engineering and Design*, 49-50:213–216, November 2000.

[138] H. Yoshida, M. Taniguchi, K. Yokoyama, Y. Yamauchi, Y. Hirohata, M. Akiba, and T. Hino. Deuterium retention in carbon dust and carbon-tungsten mixed dust prepared by deuterium arc discharge. *Journal of Nuclear Materials*, 329-333(Part 1):790–794, August 2004.

[139] O.V Ogorodnikova, J Roth, and M Mayer. Deuterium retention in tungsten in dependence of the surface conditions. *Journal of Nuclear Materials*, 313-316:469–477, March 2003.

[140] M. Poon, J. W. Davis, and A. A. Haasz. Effect of carbon pre-implantation on deuterium retention in tungsten. *Journal of Nuclear Materials*, 283-287(Part 2):1062–1067, December 2000.

[141] Yasuhisa Oya, Yuji Inagaki, Sachiko Suzuki, Hirotada Ishikawa, Yohei Kikuchi, Akira Yoshikawa, Hirotomo Iwakiri, Naoko Ashikawa, Akio Sagara, Naoaki Yoshida, and Kenji Okuno. Behavior of hydrogen isotope retention in carbon implanted tungsten. *Journal of Nuclear Materials*, 390-391:622–625, June 2009.

[142] H. Atsumi and T. Tanabe. Hydrogen retention in high-z materials with various contents of carbon. *Journal of Nuclear Materials*, 258-263(Part 1):896–901, October 1998.

[143] R.A. Anderl, R.J. Pawelko, and S.T. Schuetz. Deuterium retention in w, w1 *Journal of Nuclear Materials*, 290-293:38–41, March 2001.

[144] T. Horikawa, B. Tsuchiya, and K. Morita. Retention and re-emission of deuterium implanted into tungsten monocarbide. *Journal of Nuclear Materials*, 258-263(Part 1):1087–1091, October 1998.

[145] V. Kh. Alimov and B. M. U. Scherzer. Deuterium retention and re-emission from tungsten materials. *Journal of Nuclear Materials*, 240(1):75–80, December 1996.

[146] R.A. Roy, R. Petkie, and A. Boulding. Properties and microstructure of tungsten films deposited by ion-assisted evaporation. *Journal of Materials Research*, 6:80–91, 1991.

[147] Y. G. Shen, Y. W. Mai, Q. C. Zhang, D. R. McKenzie, W. D. McFall, and W. E. McBride. Residual stress, microstructure, and structure of tungsten thin films deposited by magnetron sputtering. *Journal of Applied Physics*, 87(1):177–187, 2000.

[148] T. J. Vink, W. Walrave, J. L. C. Daams, A. G. Dirks, M. A. J. Somers, and K. J. A. van den Aker. Stress, strain, and microstructure in thin tungsten films deposited by dc magnetron sputtering. *Journal of Applied Physics*, 74(2):988–995, 1993.

[149] http://gwyddion.net. gwyddion.

[150] E. S. Gadelmawla, M. M. Koura, T. M. A. Maksoud, I. M. Elewa, and H. H. Soliman. Roughness parameters. *Journal of Materials Processing Technology*, 123(1):133–145, April 2002.

[151] F. Frost, D. Hirsch, and A. Schindler. Evaluation of afm tips using nanometer-sized structures induced by ion sputtering. *Applied Surface Science*, 179(1-4):8–12, July 2001.

[152] The international centre for diffraction data. icdd/jcpds database pdf-2,2000.

[153] M. Birkholz. *Thin Film Analysis by X-ray Scattering.* Wiley-VCH, Weinheim, 2006.

[154] R.A. Roy, R. Petkie, D.S. Yee, J. Karasinski, and A. Boulding. *Processing and Characterization of Materials Using Ion Beams.* Materials Research Society, 1989.

[155] O.V. Ogorodnikova, J. Roth, and M. Mayer. Pre-implantation and pre-annealing effects on deuterium retention in tungsten. *Journal of Nuclear Materials*, 373(1-3):254–258, February 2008.

[156] Wei-Kan Chu, James W. Mayer, and Marc-A. Nicolet. *Backscattering Spectrometry.* Academic Press, 1978.

[157] Joseph R. Tesmer and Michael Nastasi, editors. *Handbook of modern ion beam materials analysis.* Materials Research Society, 1995.

[158] Matej Mayer. Simnra user's guide. Technical report, IPP 9/113, 1997.

[159] S.Y. Tong, W.N. Lennard, P.F.A. Alkemade, and I.V. Mitchell. Absolute surface carbon coverage determination via the 12c(3he, p)14n reaction. *Nuclear Instruments and Methods in Physics Research Section B: Beam Interactions with Materials and Atoms*, 45(1-4):91–94, January 1990.

[160] J. L. Forand, C. Timmer, E. Wahlin, B. D. DePaola, G. H. Dunn, D. R. Swenson, and K. Rinn. A probe for real-time images of particle beams and their analyses in a merged-beams apparatus. *Review of Scientific Instruments*, 61(11):3372–3377, 1990.

[161] D. Naujoks and W. Eckstein. Non-linear erosion effects in plasma experiments. *Journal of Nuclear Materials*, 230(2):93–100, June 1996.

[162] David N. Ruzic. The effects of surface roughness characterized by fractal geometry on sputtering. *Nuclear Instruments and Methods in Physics Research Section B: Beam Interactions with Materials and Atoms*, 47(2):118–125, April 1990.

[163] M. Küstner, W. Eckstein, V. Dose, and J. Roth. The influence of surface roughness on the angular dependence of the sputter yield. *Nuclear Instruments and Methods in Physics Research Section B: Beam Interactions with Materials and Atoms*, 145(3):320–331, November 1998.

[164] Johan B. Malherbe. Bombardment-induced ripple topography on gaas and inp. *Nuclear Instruments and Methods in Physics Research Section B: Beam Interactions with Materials and Atoms*, 212:258–263, December 2003.

[165] Maxim A. Makeev and Albert-Laszlo Barabasi. Secondary ion yield changes on rippled interfaces. *Applied Physics Letters*, 72(8):906–908, 1998.

[166] K Reichelt. Nucleation and growth of thin films. *Vacuum*, 38(12):1083–1099, 1988.

[167] Y. Lifshitz, S. R. Kasi, J. W. Rabalais, and W. Eckstein. Subplantation model for film growth from hyperthermal species. *Phys. Rev. B*, 41(15):10468–10480, May 1990.

[168] B. Schrader. *Infrared and Raman Spectroscopy.* VCH, Weinheim, 1995.

[169] Hsiao chu Tsai and D. B. Bogy. Characterization of diamondlike carbon films and their application as overcoats on thin-film media for magnetic recording. *Journal of Vacuum Science & Technology A: Vacuum, Surfaces, and Films*, 5(6):3287–3312, 1987.

[170] R. Kalish. Ion beam modification of diamond. *Diamond and Related Materials*, 2(5-7):621–633, April 1993.

[171] Srinandan Kasi, Heon Kang, and J. Wayne Rabalais. Chemically bonded diamondlike carbon films from ion-beam deposition. *Phys. Rev. Lett.*, 59(1):75–78, Jul 1987.

[172] Retsuo Kawakami and Kaoru Ohya. Comparison between static and dynamic simulations of ion reflection and sputtering from layered materials. *Japanese Journal of Applied Physics*, 40(Part 1, No. 9A):5399–5406, 2001.

[173] W. Eckstein. Oscillations of sputtering yield. *Nuclear Instruments and Methods in Physics Research Section B: Beam Interactions with Materials and Atoms*, 171(4):435–442, December 2000.

[174] A. C. Ferrari and J. Robertson. Interpretation of raman spectra of disordered and amorphous carbon. *Phys. Rev. B*, 61(20):14095–14107, May 2000.

[175] T. Hirai, J. Compan, K. Niwase, and J. Linke. Laser raman microprobe analysis of graphite exposed to edge plasma in the textor tokamak. *Journal of Nuclear Materials*, 373(1-3):119–122, February 2008.

[176] V.Kh. Alimov, M. Mayer, and J. Roth. Differential cross-section of the d(3he, p)4he nuclear reaction and depth profiling of deuterium up to large depths. *Nuclear Instruments and Methods in Physics Research Section B: Beam Interactions with Materials and Atoms*, 234(3):169–175, June 2005.

[177] N. Yoshida, M. Yasukawa, and T. Muroga. Evolution of microstructure in nickel by low-energy deuterium ion irradiation. *Journal of Nuclear Materials*, 205:385–393, October 1993.

[178] G. Staudenmaier, J. Roth, R. Behrisch, J. Bohdansky, W. Eckstein, P. Staib, S. Matteson, and S.K. Erents. Trapping of deuterium implanted in carbon and silicon: A calibration for particle-energy measurements in the plasma boundary of tokamaks. *Journal of Nuclear Materials*, 84(1-2):149–156, October 1979.

[179] T Tanabe, N Bekris, P Coad, C.H Skinner, M Glugla, and N Miya. Tritium retention of plasma facing components in tokamaks. *Journal of Nuclear Materials*, 313-316:478–490, March 2003.

[180] S. Nagata and K. Takahiro. Deuterium retention in tungsten and molybdenum. *Journal of Nuclear Materials*, 283-287(Part 2):1038–1042, December 2000.

[181] A. A. Haasz and J. W. Davis. Deuterium retention in beryllium, molybdenum and tungsten at high fluences. *Journal of Nuclear Materials*, 241-243:1076–1081, February 1997.

[182] A.D. Quastel, J.W. Davis, A.A. Haasz, and R.G. Macaulay-Newcombe. Effect of post-d+-irradiation time delay and pre-tds heating on d retention in single crystal tungsten. *Journal of Nuclear Materials*, 359(1-2):8–16, December 2006.

[183] J. Luthin and Ch. Linsmeier. Carbon films and carbide formation on tungsten. *Surface Science*, 454-456:78–82, May 2000.

[184] J. Luthin. *Chemical interactions during the formation of carbon-based mixed materials.* PhD thesis, IPP-Report 9/129, 2001.

[185] Fan C. Sze, Leo Chousal, Russ P. Doerner, and Stan Luckhardt. Growth of redeposited carbon and its impact on isotope retention properties on tungsten in a high flux deuterium plasma. *Journal of Nuclear Materials*, 266-269:1212–1218, March 1999.

[186] M. Poon, A.A. Haasz, and J.W. Davis. Modelling deuterium release during thermal desorption of d+-irradiated tungsten. *Journal of Nuclear Materials*, 374(3):390–402, March 2008.

[187] I.A. Bizyukov, J.W. Davis, A.A. Haasz, and P. Brodersen. Cd4 production from mixed w-c-d surface during simultaneous irradiation of w with c+ and d+. *Journal of Nuclear Materials*, 390-391:925–928, June 2009.

[188] James F. Ziegler. Srim-2003. *Nuclear Instruments and Methods in Physics Research Section B: Beam Interactions with Materials and Atoms*, 219-220:1027–1036, June 2004.

[189] Donald Estep, editor. *Practical Analysis in One Variable.* Springer New York, 2002.

[190] K Ohya. Dynamic simulation of erosion and redeposition on plasma-facing materials. *Physica Scripta*, T124:70–75, 2006.

[191] A. Kirschner, V. Philipps, J. Winter, and U. Kogler. Simulation of the plasma-wall interaction in a tokamak with the monte carlo code ero-textor. *Nuclear Fusion*, 40(5):989–1001, 2000.

[192] V.A. Abramov, Yu.L. Igitkhanov, V.I. Pistunovich, and V.A. Pozharov. First wall and divertor plate sputtering in a tokamak reactor. *Journal of Nuclear Materials*, 162-164:462–466, April 1989.

[193] K. Schmid, K. Krieger, A. Kukushkin, and A. Loarte. Divimp modeling of tungsten impurity transport in iter. *Journal of Nuclear Materials*, 363-365:674–679, June 2007.

[194] Ch. Linsmeier, K. Ertl, J. Roth, A. Wiltner, K. Schmid, F. Kost, S.R. Bhattacharyya, M. Baldwin, and R.P. Doerner. Binary beryllium-tungsten mixed materials. *Journal of Nuclear Materials*, 363-365:1129–1137, June 2007.

[195] J P Coad, P L Andrew, and A T Peacock. Carbon deposition and hydrogen isotope retention in jet. *Physica Scripta*, T81:7–12, 1999.

[196] J.P. Coad, N. Bekris, J.D. Elder, S.K. Erents, D.E. Hole, K.D. Lawson, G.F. Matthews, R.-D. Penzhorn, and P.C. Stangeby. Erosion/deposition issues at jet. *Journal of Nuclear Materials*, 290-293:224–230, March 2001.

[197] D.G. Whyte, J.P. Coad, P. Franzen, and H. Maier. Similarities in divertor erosion/redeposition and deuterium retention patterns between the tokamaks asdex upgrade, diii-d and jet. *Nuclear Fusion*, 39(8):1025–1029, 1999.

[198] Y. Gotoh, J. Yagyu, K. Masaki, K. Kizu, A. Kaminaga, K. Kodama, T. Arai, T. Tanabe, and N. Miya. Analyses of erosion and re-deposition layers on graphite tiles used in the w-shaped divertor region of jt-60u. *Journal of Nuclear Materials*, 313-316:370–376, March 2003.

[199] K. Schmid. Beryllium flux distribution and layer deposition in the iter divertor. *Nuclear Fusion*, 48(10):105004 (10pp), 2008.

[200] K. Krieger, S. Brezinsek, S. Jachmich, S. Lisgo, M. Stamp, H.G. Esser, A. Kreter, S. Menmuir, Ph. Mertens, V. Philipps, P. Sundelin, and JET EFDA contributors. Be wall sources and migration in l-mode discharges after be evaporation in the jet tokamak. *Journal of Nuclear Materials*, 390-391:110–114, June 2009.

[201] K. Inai, K. Ohya, Y. Tomita, A. Kirschner, A. Litnovsky, and T. Tanabe. Simulation of redeposition of carbon/hydrocarbon on a material surface with castellated structures. *Journal of Nuclear Materials*, 390-391:119–122, June 2009.

Acknowledgments

First and foremost, I would like to thank **Prof. Dr.-Ing. Dr.-Eng. Harald Bolt** for providing me the opportunity to pursue my dissertation at IPP, and guiding me through the entire process. **Prof. Dr. E. Werner** for allowing me to pursue my doctorate degree at the Maschinenwesen department of TU München. A heart-felt thanks to **Dr. Karl Krieger** for his guidance and encouragement during the past three and a half years, and for his critical reading of the manuscript and relevant discussions. Thank you to **Dr. Joachim Roth** and **Dr. Karl Ertl** for their oversight and allowance in all purchases and conference related matters.

Special thanks to **Dr. Florian Kost**, and **Dr. Almut Wiltner** for the XPS measurements and analysis. **Dr. Monika Rinke** at IMF I des Forschungszentrums Karlsruhe for the Raman measurements. **Dr. Christoph Adelhelm** and **Martin Triendl** for help with AFM measurements. **Dr. Klaus Schmid** for help with the TRIDYN program and all relevant questions, and **Dr. Kazuyoshi Sugiyama** for his help with depth profile analysis and fruitful discussions. **Dr. Martin Balden** and **Stefan Lindig** for help with XRD and SEM measurements, and **Marcin Rasinski** for FIB measurements. **Freimut Koch** for his support in operating the magnetron sputter device, and **Thomas Dürbeck** for his aid in profilometry measurements.

I would also like to thank **Gabi Matern** for the polishing and preparation of my substrates, and a big thank you to **Herrn Peter Matern** for his numerous help and support in operating the Dual Beam Experiment. I am extremely grateful to my technicians, **Michael Fußeder** and **Joachim Dorner** for their operation of the tandem accelerator and patience during those late nights to finish my measurements.

Dr. Aurelia Herrman for all her help with German-language related issues and the boat rides, and **Frau Eggeling** and **Frau Mezger** for their support in all things bureaucratic related, that I must admit, I was always late for. Thank you to fellow PhD students, **Yury Gasparyan**, **Peter Worbs** and **Verena Paffenholz** for their friendship and help. Also, **Rainer Piechoczek** for being so optimistic all the time and **Christine Medina** for her support and numerous care packages.

Last but not least, I would like to thank Nozomi for keeping me sane, and of course my parents for their support and belief throughout my everlasting schooling process and my sisters for their incredible love and care. Without them nothing would have been possible.